

LA-4858-MS, Vol. I

AN INFORMAL REPORT

e. 1

# Central Station Power Generation by Laser-Driven Fusion



---

**For Reference**

**Not to be taken from this room**



**los alamos**  
**scientific laboratory**

of the University of California

LOS ALAMOS, NEW MEXICO 87544

↓      ↓

This report was prepared as an account of work sponsored by the United States Government. Neither the United States nor the United States Atomic Energy Commission, nor any of their employees, nor any of their contractors, subcontractors, or their employees, makes any warranty, express or implied, or assumes any legal liability or responsibility for the accuracy, completeness or usefulness of any information, apparatus, product or process disclosed, or represents that its use would not infringe privately owned rights.

In the interest of prompt distribution, this LAMS report was not edited by the Technical Information staff.

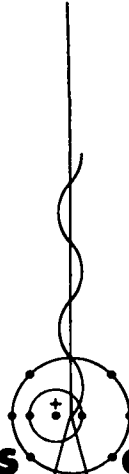
Printed in the United States of America. Available from  
National Technical Information Service  
U. S. Department of Commerce  
5285 Port Royal Road  
Springfield, Virginia 22151  
Price: Printed Copy \$3.00; Microfiche \$0.95

LA-4858-MS, Vol. I

An Informal Report

UC-20

ISSUED: February 1972



**Los Alamos**  
**scientific laboratory**  
of the University of California  
LOS ALAMOS, NEW MEXICO 87544

# Central Station Power Generation by Laser-Driven Fusion



Compiled by

**L. A. Booth**

## PREFACE

This report has been prepared for the Controlled Thermonuclear Research program of the U. S. Atomic Energy Commission, and presents the results of a study investigating an application of laser-driven fusion pulses for commercial power generation. The present discussion assesses the engineering feasibility of this application. The analyses are based on a specific design concept for utilizing the fusion energy and have been carried only to the point where semiquantitative conclusions may be made. The work, therefore, is at an interim stage and all findings are preliminary.

Certain aspects of the proposed techniques for generating the fusion energy remain classified. These matters are discussed in Volume II (LA-4859-MS, Classified, SRD).

This work has been conducted by the Advanced Concepts group of the Los Alamos Scientific Laboratory (LASL) Nuclear Propulsion Division. Staff members who contributed to this report were J. D. Balcomb, L. A. Booth, J. C. Hedstrom, D. B. Henderson, A. R. Larson, S. W. Moore, and C. W. Watson.

---



## NOMENCLATURE

A	Area	$m^2$
$A_f$	Cross-sectional flow area, Eq. (22)	$m^2$
$A_r$	Surface area, Eq. (25)	$m^2$
$C_p$	Heat capacity at constant pressure	J/kg K
$C_v$	Heat capacity at constant volume	J/kg K
D	Dimension, thickness	m
$D_t$	Film thickness, Eq. (24)	m
$D_w$	Wall thickness, Eq. (29)	m
E	Specific internal energy	J/kg
$E_s$	Source energy, Eqs. (3) and (14)	J/kg
$F_D$	Viscous drag force, Eq. (23)	$J/m^3$
g	Gravitational acceleration	$m/sec^2$
h	Gravitational head	m
$H_v$	Total heat content	J/kg
$\Delta H_v$	Heat of vaporization	J/kg
I	Internal energy	J
$k_t$	Thermal conductivity	W/m K
$r$	Tangential dimension, Eq. (21)	m
M	Mass	kg
$M_{vc}$	Mass vaporized, Eq. (16)	kg
$M_s$	Mass source, Eq. (11)	kg
$m$	Mass, Lagrangian coordinate system	kg
$\dot{m}$	Mass flow rate, Eq. (22)	kg/s
$\dot{M}$	Total mass flow	kg/s
P	Pressure	$N/m^2$
q	Volumetric heat generation rate	$J/m^3 \text{ s}$
Q	Viscous pressure, Eq. (B-1)	$N/m^2$
r	Radius, also Lagrangian coordinate	m
R	Gas constant	J/kg K
STP	Standard temperature and pressure	
t	Time	s
T	Temperature	K
U	Velocity	m/s
v	Specific volume	$M^3/kg$

V	Volume	$m^3$
x	Dimension, also Eulerian coordinate	m
Y	Young's modulus	$N/m^2$
$\beta_T$	Coefficient of thermal expansion	$K^{-1}$
$\beta_c$	Compressibility coefficient	$m^2/N$
$\gamma$	Ratio of specific heats ( $C_p/C_v$ )	-
$\lambda$	Average mean free path for thermal radiation	m
$\mu$	Viscosity	$N \cdot s/m^2$
$\mu$	Poisson's ratio, Eq. (20)	-
$\chi$	Void fraction	.
$\rho$	Density	$kg/m^3$
$\rho_T$	Combined liquid and gas density, Eq. (12)	$kg/m^3$
$\tau$	Time constant, Eq. (9)	s

l	Liquid
o	Initial condition
v	Vapor or gas
vp	Saturation condition

---

#### ABSTRACT

The feasibility of using laser-driven fusion pulses for the commercial generation of electric power was investigated. Results are presented in two volumes. Volume I (IA-4858-MS, Uncl.) discusses the general aspects of electric power plants based on laser-driven fusion energy sources, outlines the considerations that led to the wetted-wall concept on which the present study is based, presents detailed results of calculations that indicate the feasibility of the concept, discusses aspects of important areas that are not well defined, summarizes related needs for further study, and compares the concept with plants based on magnetically confined controlled thermonuclear reactions. Volume II (IA-4859-MS, Classified, SRD) outlines IASL's laser program, discusses the problems of achieving laser-driven fusion, considers subsequent neutronic interactions, and gives some economic implications.

---

CENTRAL STATION POWER GENERATION  
BY LASER-DRIVEN FUSION

- VOLUME I -

Compiled by L. A. Booth

I. INTRODUCTION

A. GENERAL

It is generally recognized within the scientific community that within the next few generations the world's fossil and rich-ore fissile fuel supplies will be depleted to the extent that their use for energy production will become economically unattractive. It is also recognized that the natural supply of the common thermonuclear materials, deuterium and lithium, is far greater than the estimated reserves of fossil and rich-ore fissile fuels. Therefore, an international cooperative program (Sherwood project) was initiated as early as 1955 to find a means of producing controlled thermonuclear energy.

The concepts generated in this international program are based on using magnetic forces to compress and heat the thermonuclear material to ignition conditions and to confine this material while it burns. However, in recent years, the development of laser technology has made compression, heating, and confinement by inertial forces an alternative theoretical possibility for practical utilization of thermonuclear energy. For purposes of this report, the conceptual devices based on these two means of producing thermonuclear energy will be termed:

- Magnetically Confined Thermonuclear Reactors (MCTR) and
- Inertially Confined Thermonuclear Reactors (ICTR).

This report describes a specific conceptual ICTR and attendant means of utilizing the thermonuclear energy for commercial electrical power

generation. The ICTR discussed in this report consists of concentric spherical vessels (shells) in which the thermonuclear energy is derived from a deuterium-tritium (D+T) burn within a "pellet", located at the center of the vessels and initiated by a laser pulse. The resulting  $\alpha$ -particle energy and a small fraction of the neutron energy are deposited within the pellet; this pellet energy is eventually transformed into sensible heat of lithium in a condenser outside the vessels. The remaining neutron energy is dissipated in a lithium blanket, located within the concentric shells, where the fuel ingredient, tritium, is also produced. The heat content of the blanket and of the condenser lithium is eventually transferred to a conventional thermodynamic plant where the thermal energy is converted to electrical energy in a steam Rankine cycle.

For this volume of the report, the following assumptions are made:

- The (D+T) energy released--17.6 MeV per (D+T) reaction--is 200 MJ once each second.
- Twenty-five percent--4.4 MeV per (D+T) reaction--of this energy is deposited within the pellet, and the remaining 75% is transported outside the pellet by neutrons.

The mechanisms for laser energy absorption and for (D+T) ignition and burning are tacitly ignored. A discussion of these matters is included in Volume II (IA.4859-MS) of this report.

## B. GENERAL ASPECTS OF ICTR PLANTS

For a (D+T)-burning plant, two essential requirements in an ICTR concept are similar to those in an MCTR: (1) the need to produce tritium artificially because natural supplies are insufficient to support a large-scale power-generation industry, and (2) the need to convert the 14-MeV neutron energy into usable form, because there is no known means of using the energy of 14-MeV neutrons directly except by transforming this energy into thermal energy of another substance.

Both needs are satisfied by providing a "blanket" of lithium which surrounds the source of (D+T) energy. Tritium is generated in a major fraction of reactions between neutrons and lithium; and lithium, being a light element, also converts neutron kinetic energy to thermal energy by means of elastic-scattering reactions. Furthermore, additional thermal energy is produced by neutrons absorbed in the lithium. It is essential that at least as much tritium be generated as is burned and lost, and that as much as possible of the neutron energy be converted into thermal energy.

Fortunately, tritium breeding ratios in a lithium blanket can be relatively high--in the range of 1.2 to 1.6--which would provide a large operating margin to an ICTR plant. However, because tritium losses will of necessity be small, the plant will operate normally at a breeding ratio only slightly greater than unity to prevent unnecessary buildup of tritium reserves, although the plant can operate temporarily with a high breeding ratio to build up a fuel inventory for a new plant.

Because the major fraction of the (D+T) energy will be converted in the blanket to thermal energy, the dominant method of converting thermal energy to electricity will probably be by means of a heat engine in a thermodynamic cycle. Such a cycle will be used merely because it offers the highest conversion efficiency in the temperature range in which normal engineering materials can operate. The possibilities of directly converting the remaining energy into electricity are discussed in Section III; however, the amount thus generated can be, at best, only a minor fraction of the total energy release.

A characterizing ICTR feature that is significantly different from any MCTR aspect is the fact that the energy pulses represent substantial amounts of explosive energy. As described in detail in Volume II, the minimum energy release, determined by both physical and economic considerations, is probably at least 200 MJ (equivalent to 95.6 lb of TNT), which clearly calls for a sturdy pressure vessel for containment. A major design problem in containing this blast energy is posed by the need for a low-pressure cavity in which the pellet can be initiated by a laser pulse without prohibitive laser-energy loss along its path, while, at the same time, maintaining a finite layer of blanket material that surrounds the pellet.

In one proposed concept<sup>(1)</sup> the cavity is defined by the vortex of a swirling liquid blanket; in another, suggested at IASL, the cavity is formed by the wake of a projectile and the pellet is initiated before the cavity collapses. In both concepts the liquid blanket is filled with gas bubbles, providing a compressible but dense medium to attenuate the blast shock arriving at the containing pressure-vessel wall.

Another method of defining the cavity region is to separate the cavity from the blanket by a solid wall. One significant advantage to the solid-wall concept (as opposed to concepts with no wall) is that the cavity region is well defined and thus amenable to analysis. Another advantage, which may be even more important, is the possibility of providing a passage by mechanical means for exhausting the hot gases in the cavity prior to the next shot. In the absence of a solid wall to define the cavity, much blanket lithium would be swept out of the vessel as these gases exhaust. The alternative approach, i.e., allowing these gases to condense in the blanket lithium, would take an excessively long time between shots.

In the solid-wall concept, the inner surface of the wall must be protected from the damaging effects of the blast to prevent vaporization of the wall material by thermal radiation and erosion by high-velocity material, both of which emanate from the fuel pellet. Liquid lithium is used to form a protective layer on the inner-cavity wall.

This concept, subsequently referred to as the wetted-wall concept, has been selected for analysis and will be discussed at length.

### C. CONSIDERATIONS LEADING TO THE WETTED-WALL CONCEPT

Three general features are essential to an ICER design: a cavity within which to detonate the pellet, a pressure vessel to contain the blast, and a thick blanket containing lithium to convert the fast-neutron energy into heat and into tritium fuel. However, within these constraints there remains a wide latitude within which to design the plant. For the present study a straightforward approach was identified and the development of a minimum of new technologies was assumed. This approach will not necessarily result in a highly efficient plant nor in one satisfying all needs. However, if laser-driven fusion becomes a reality in the near future, as is certainly possible, there will be a need for a realistic design to serve as a basis for early plants.

As mentioned earlier, the proposed concept uses a solid wall to separate the reaction cavity from the lithium blanket. The main design problems then become those of providing for the protection from the direct effects of the blast. This protection can be afforded by a thin layer of ablative material which, as it vaporizes, absorbs the energy of radiation and impact from the pellet. A layer of lithium, wetting the inside of the wall, should furnish this protection. If the wall is porous, the lithium layer can be restored after each pulse by a radial inflow of lithium from the blanket region. Thus the concept develops of a porous, wetted wall.

A second design problem concerns the containment of the blast energy. If the porous, wetted wall is thick enough to contain the blast, then internal heating will lead to excessive temperatures; also, the breeding ratio in the blanket will be reduced to an unacceptable level. Therefore, the wall must be thin. The momentum from the blast is transmitted through the relatively incompressible lithium behind the wall to a main pressure vessel, which is thick enough to contain the energy. This pressure vessel is placed inside the lithium blanket at a location where the breeding ratio is not significantly affected (see Appendix A).

This configuration of main vessel and wetted wall poses another design problem. The pressure waves reverberating between these two walls result in inward motion of the wetted wall. Because this wall is too thin to restrain the motion, another inner wall is needed between the pressure vessel and the wetted wall, with sufficient thickness to restrain the inward motion yet not thick enough to prohibitively reduce the breeding ratio.

The blast-containing design thus evolves into a system with at least three walls:

- An innermost porous wall, which is thin and allows the passage of lithium to form a protective coating on the inside surface.

- A main pressure-vessel wall, thick enough to restrain the internal pressures in the cavity and blanket, located deep enough into the blanket so that it does not seriously affect the breeding ratio.

- An inner structural wall, located between the former two walls, which is thick enough to restrain the inward motion and thin enough so that it still permits an adequate breeding ratio.

In the design of these walls, the strains and corresponding stresses must be limited to values which would not exceed the fatigue limits of the materials used. Therefore, careful design and analysis are necessary to minimize the motions of these walls.

A lithium flow path is chosen which introduces the return lithium (from the primary loop) at the surface of the porous wetted wall and forces it to flow radially outward through the blanket. Thus the wetted wall is exposed to the lowest temperature in the primary lithium loop. This temperature is chosen to be 400°C, which is well above the lithium melting point of 186°C, but is within the acceptable range for ferritic stainless steels. The use of stainless steel reduces the cost of the vessel. Maintaining the inner wall at the minimum loop temperature also reduces the mass transport of wall material by the flowing lithium to other parts of the loop and ensures that the lithium coating the inner surface is relatively cool, with a low vapor pressure; therefore, the lithium vapor density in the cavity prior to the blast is minimized. (The

vapor pressure of lithium at 400°C is  $\sim 10^{-4}$  Torr, which should be well below the cavity vacuum required for passage of the laser pulse.)

The temperature attained by the lithium flowing from the outer portion of the blanket to the heat exchanger is dependent upon the blanket thermal power and upon the lithium flow rate. For this temperature, a value of 750°C (1380°F) was arbitrarily chosen to be compatible with existing steam technology. A maximum temperature as high as 1000°C or higher could be easily postulated, as has been done for some MCTR plant studies, but this would introduce a host of presently unanswerable materials questions that can be bypassed by assuming only temperatures associated with existing steam technology.

Certain phenomena concerning the operation of the wetted-wall ICTR require analyses to determine the engineering feasibility of the concept. These are listed below:

1. Pellet interaction with the wetted-wall layer.
2. Equilibration conditions of the cavity gases after a pellet burn and exhaustion (blowdown) of these gases so that the initial conditions are restored before the next pellet is initiated.
3. Condensation of the exhaust gases and transformation of the cavity energy into heat content of the condenser lithium.
4. Formation of the protective layer on the inside surface of the wetted wall.
5. Tritium breeding and energy deposition within the blanket system.

6. Removal of the heat generated within the blanket.

7. Structural response of the restraining walls within the blanket.

8. Radiation damage to the solid materials within the system.

9. Induced activity in the materials within the system.

10. Removal of contaminants from the lithium.

11. Safety features of an ICTR.

12. Economics of an ICTR power plant.

Items 1 through 7 are considered crucial to the feasibility of the present concept. Although Items 8 through 12 need attention, there are uncertainties, due either to the lack of technology or to undefined design criteria, which hinder the determination of feasibility by "paper studies". Items 8 through 12 are therefore discussed in general terms only, in Section III.

Tritium breeding and energy deposition (Item 5) require analysis of nuclear processes. Because of the complexity and importance of the analysis, it is appropriate that the presentation be self-contained; therefore, the nuclear radiation-transport considerations are discussed separately in Appendix A.

The remaining items are grouped into those concerning the cavity (Items 1 through 4) and those concerning the blanket (Items 6 and 7). The analyses of these phenomena follow in Section II.

## II. ANALYSES OF WETTED-WALL CONCEPT

The analyses of the cavity and blanket phenomena presented in this section are based on current calculational methods and available data. During the few months available for this study, the analyses have been conducted only to the point where reasonable conclusions concerning the engineering feasibility of the wetted-wall concept may be made. In some instances an analysis has not been completed, and further work is called for. These cases are pointed out as they are subsequently discussed.

### A. GENERAL DESCRIPTION

#### 1. Introduction

A schematic of the wetted-wall ICTR is shown in Fig. 1. The pellet (containing D+T) is injected through a port, which penetrates the blanket, and is initiated at the center of the cavity by a laser pulse; the cavity is defined by the wetted wall located at a radius of 1.0 m from the center. The subsequent (D+T) burn releases 200 MJ of energy. Within fractions of a microsecond, 50 MJ is deposited within the pellet and 152.5 MJ is generated within the blanket lithium and structural materials.

#### 2. Cavity Phenomena

Within ~ 0.5 ms the pressure pulses generated by the interaction of the pellet with the lithium at the wetted wall have subsided. Within the next few milliseconds, the cavity conditions are equilibrated, ~ 1.6 kg of lithium are vaporized from the protective layer at the wall, and sonic flow conditions of the cavity gases are established at the outlet port.

The flow of hot gases through the cavity outlet port is expanded in a diffuser to supersonic conditions, and the gases are then condensed in a downstream length of duct where a finely atomized spray of liquid lithium is injected. (The spray of

atomized droplets is recirculated from the liquid pool at the bottom of the condenser.) Downstream of the condenser duct, the mixture of gas and liquid droplets, still at supersonic velocity, is decelerated by turbulent mixing created by a spray of large lithium droplets. (The coarse-droplet spray is provided from a side-stream of the 400°C return flow from the heat exchanger.) The kinetic energy of this mixture is finally absorbed by impacting with a pool of liquid lithium at the bottom of the condenser system.

After ~ 0.2 s, the pressure within the cavity decreases to less than atmospheric, and the blow-down continues during the remaining 0.8 s of the pulse cycle, reducing the cavity pressure to less than  $133 \text{ N/m}^2$  (1.0 mm Hg). The cycle is then repeated with the initiation of another pellet.

#### 3. Blanket Phenomena

The energy deposited within the blanket is removed by circulating the lithium through an external heat exchanger. Lithium, flowing at 400°C from the heat exchanger, is returned to a plenum between the 1.0-cm-thick wetted wall and the 5.0-cm-thick inner structural wall, which serves to restrain the movement of the inner blanket boundary caused by the pressure waves generated within the blanket and the cavity pressure. Located a few centimeters behind the wetted wall, the inner structural wall also serves as a flow baffle for distributing the radial outflow. The wetted wall moves along with the structural wall through hydrodynamic coupling and, if needed, through mechanical attachments.

The 10.0-cm-thick main pressure vessel shell, located 1.7 m from the center of the spheres, is the outer restraint for the ICTR. This shell is stressed by the shock loads from the pressure pulses generated within the cavity and within the blanket. The radial outflow of lithium collects in

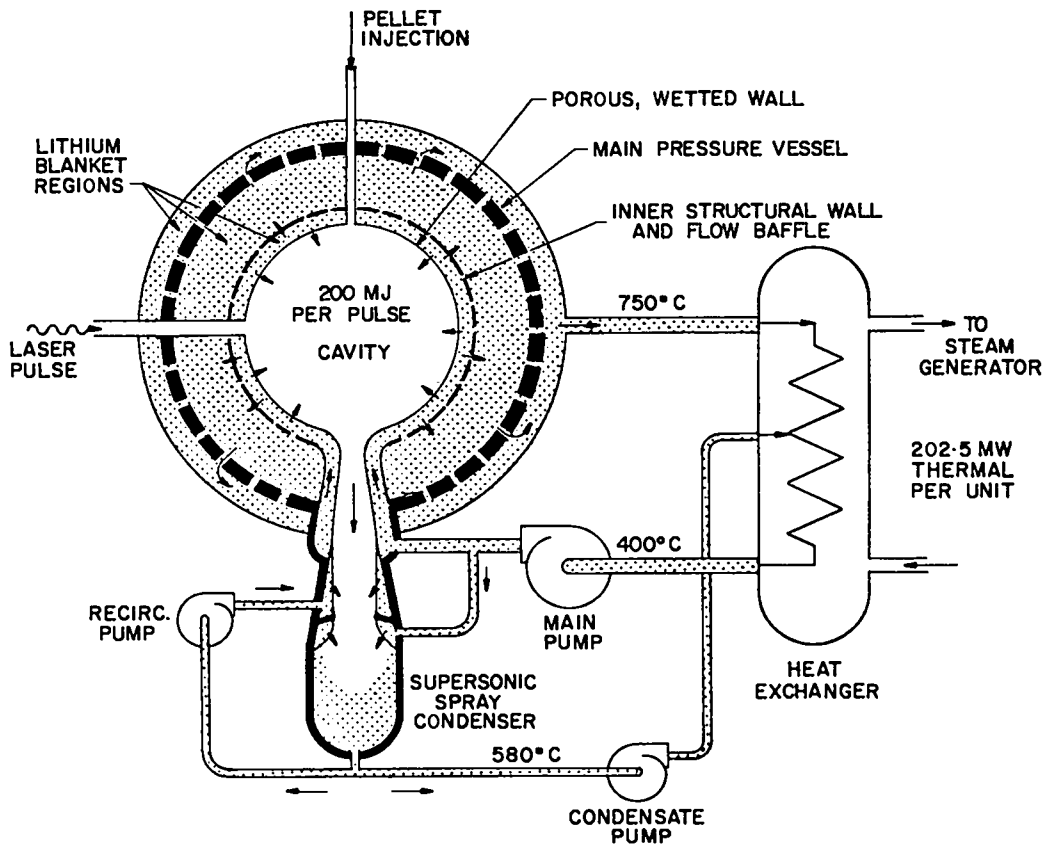


Fig. 1. Wetted-wall ICTR concept.

a plenum, defined by the outermost shell at 2.0 m from the center, and returns to the heat exchanger at 750°C.

Paths for pellet injection and for the laser pulse are provided by small ports penetrating the blanket. The diffuser for the expulsion of cavity gases provides the main structural support for the system of spherical shells.

#### 4. Thermodynamic Plant

The minimum power level is based on a thermal input of ~ 200 MW, from one ICTR. Higher power levels may be obtained by combining several ICTRs in a reactor system, thereby increasing both the versatility and the overall ratio of actual operating power to full design power. The nominal thermal power level for a conceptual plant was arbitrarily chosen to be ~ 2000 MW, requiring ten modular ICTRs.

The flow diagram of an ICTR plant module is presented in Fig. 2. The intermediate heat exchanger is placed between the tritium-containing lithium and the steam generator(s) to reduce the possibility of tritium leakage into the steam-plant components. The circulating fluid between the intermediate heat exchanger and the steam generator(s) will be determined by engineering design criteria.

The steam cycle for this power plant is based on a conventional double-steam-reheat design, sized for a thermal input of ~ 2000 MW.<sup>(2)</sup> A flow diagram of the cycle is shown in Fig. 3. The exit steam from the high-pressure and intermediate-high-pressure turbines is reheated prior to expanding through the succeeding turbine to increase the thermodynamic efficiency of the expansion. Mechanical-draft dry-cooling towers are used to reject waste heat, thus rejecting heat to the atmosphere rather than directly to natural water sources.

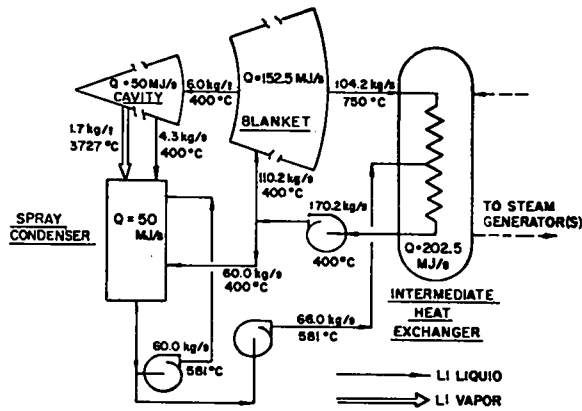


Fig. 2. ICTR plant flow diagram.

The performance characteristics of the conceptual power plant are:

Thermal power generated, MW	2025
Gross alternator output, MW	945
Steam-plant operating power, MW	48
Net steam-plant electrical output, MW	897
Net steam-plant efficiency, %	44.3
ICTR plant operating power, MW	72
Net station electrical send-out, MW	825
Net overall plant efficiency, %	40.7

The steam-plant operating power includes the requirements for boiler feed pumps, cooling-water pumps, cooling-tower draft fans, and other auxiliaries, and the ICTR plant operating power includes the requirements for lithium pumps, vacuum pumps, the laser, and other auxiliaries.

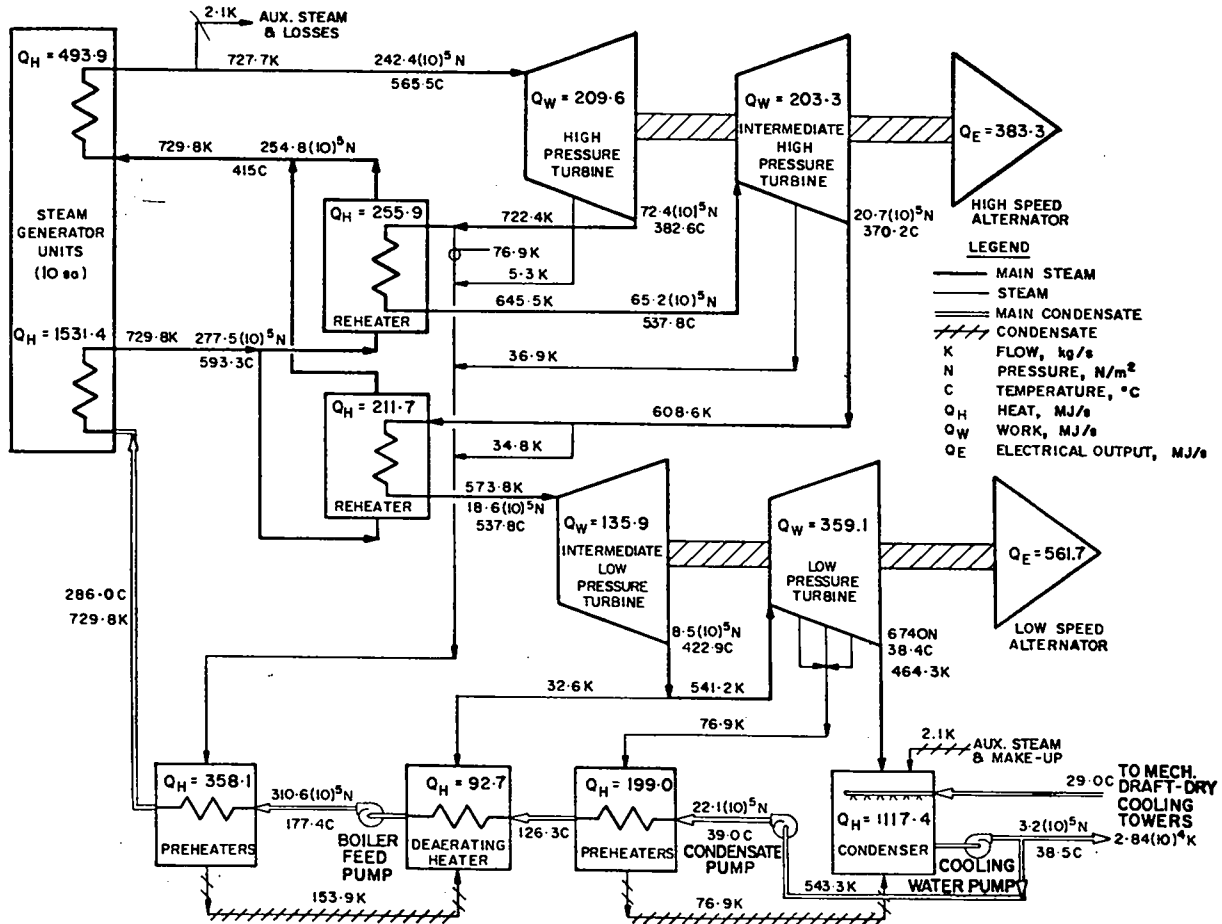


Fig. 3. Steam plant flow diagram.

## B. THE CAVITY

### 1. Introduction

Phenomena within the cavity that are crucial to the feasibility of the wetted-wall concept are:

- Pellet interaction with the wetted-wall layer -- The initial impulses transmitted into the blanket region are determined by the initial blow-off of the protective lithium layer on the wetted-wall surface by penetration of the initial thermal radiation from the pellet and subsequent radiation resulting from hydrodynamic interaction of the expanding pellet debris with this protective layer.

- Cavity equilibration and blowdown -- The quasi-equilibrium conditions (temperature, pressure, and density) of the cavity gases after the blowoff of the protective layer determine the size of the port through which these gases must exhaust, so that, within one second after the pulse, the density within the cavity is reduced to an acceptable value for the passage of the next laser pulse.

- Condensation of cavity exhaust gases -- The exhaust gases from the cavity must be cooled, condensed, and decelerated in the spray condenser in a manner that will maintain sonic flow through the exhaust port.

- Wetted-wall protective layer formation -- The protective layer of lithium must be formed on the inside surface of the wetted wall prior to the initiation of the next energy pulse.

These cavity phenomena are discussed individually in the following paragraphs.

### 2. Pellet Interaction with Wetted-Wall Layer

The analyses of the interaction phenomena are based on the solution of the gas-dynamic conservation equations of mass, momentum, and energy (coupled with energy transport by conduction and radiation diffusion) and on tabulated equation-of-state data. The conservation equations are formulated for one-dimensional spherical geometry in the Lagrangian space-coordinate system:

$$\text{Mass} \quad \frac{1}{\rho} = v = \frac{1}{3} \frac{\partial r^3}{\partial m}, \quad (1)$$

$$\text{Momentum} \quad \frac{\partial U}{\partial t} = - r^2 \frac{\partial}{\partial m} (P + Q), \quad (2)$$

$$\text{Energy} \quad \frac{\partial E}{\partial t} = - (P + Q) \frac{\partial v}{\partial t} + \frac{\partial E_s}{\partial t} + \frac{1}{\rho r^2} \left[ \lambda r^2 \frac{\partial}{\partial r} (\sigma T^4) + r^2 \frac{\partial}{\partial r} (k_t T) \right]. \quad (3)$$

These equations are integrated in space and time by a finite difference technique, as described in Appendix B, and the tabular equation-of-state data are discussed in Appendix C.

The calculation begins at 0.04  $\mu$ s after the (D+T) burn is initiated, with the pellet material containing 56.8 MJ. (For this initial calculation the amount of deposited energy was ~ 14% higher than the assumed 50 MJ.) The internal and kinetic energy distributions in the pellet material (and its geometry) are those from a pellet burn calculation described in Volume II. The lithium layer contains 1.18 kg, corresponding to a thickness of 0.196 mm, and the volume between the pellet material and the lithium layer is void. Throughout the calculation the outer boundary of the lithium (the wall boundary) is fixed at zero velocity, and hydrodynamic motion of the liquid phase is not permitted. The ablation is calculated as follows: energy is absorbed in the liquid-phase zones as internal energy until the temperature reaches ~ 6000 K (selected arbitrarily), then the material vaporizes at the saturation conditions (see Appendix C) and hydrodynamic motion of the zone begins.

The calculation has been carried out to 1000  $\mu$ s, at which time the cavity conditions are at quasi-equilibrium with the lithium boiloff rate being proportional to the cavity temperature and decreasing monotonically. The pressure profile transmitted to the wetted-wall boundary is shown in Fig. 4, and the integral of the lithium mass (vaporization rates) is presented in Fig. 5. The first pressure peak at 0.09  $\mu$ s is the result of lithium blowoff, caused by the radiation from the pellet penetrating into the lithium layer. During this initial period of radiation penetration (up to ~ 1.0  $\mu$ s), the average radiation flow is ~  $2 \times 10^5$  MW/m<sup>2</sup> and 54 g of lithium are vaporized.

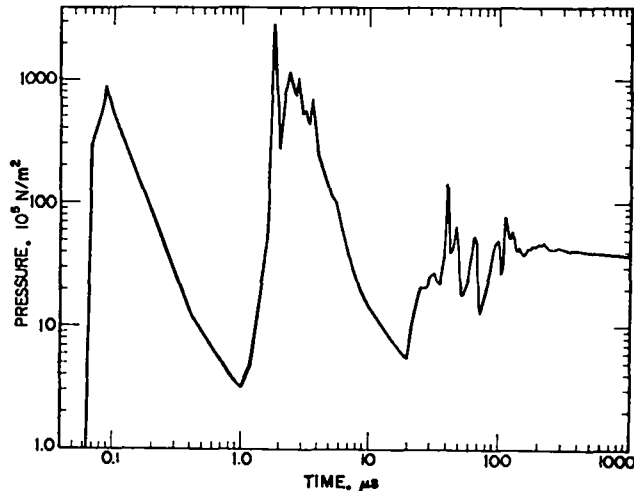


Fig. 4. Pressure transmitted to cavity boundary after pellet initiation.

At  $\sim 1.0 \mu\text{s}$  the pellet material collides with the lithium. During the subsequent period from 1.0 to  $\sim 400 \mu\text{s}$ , pressure pulses are generated at the boundary from additional lithium blowoff, caused by radiation as a result of hydrodynamic interaction of the pellet material with the lithium. The average energy flow into the lithium during this period is  $\sim 10^4 \text{ MW/m}^2$ , resulting in the vaporization of an additional 410 g of lithium.

### 3. Cavity Equilibration and Blowdown

For calculating the cavity conditions at a time later than that determined in the previous paragraph, a complete description of lithium state properties is necessary. The inclusion of this type of equation-of-state information in analytical methods for solving the hydrodynamics and heat-transport equations involves a complexity that is beyond the scope of this report. However, it will be shown that the exhaust-port size for cavity blowdown is relatively insensitive to the cavity conditions; therefore, the cavity conditions can be calculated by assuming extrapolated energy flow values from the results in Section II.B.2, above.

#### a. Cavity Equilibration

For a deposited energy of 50 MJ in a volume of  $4.189 \text{ m}^3$  (1.0 m radius), an "operating line" for the cavity conditions can be constructed on a pressure-temperature diagram. As derived in

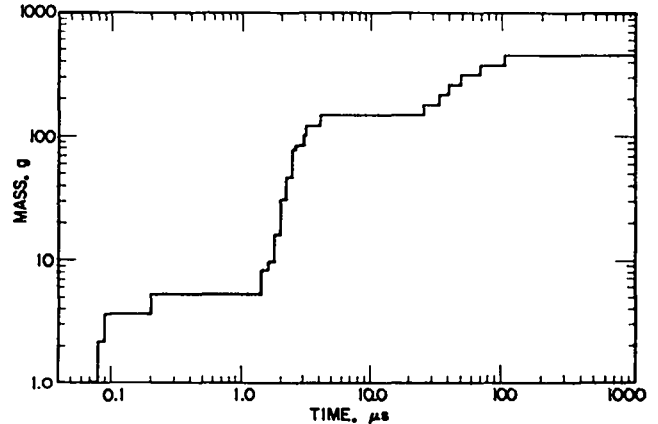


Fig. 5. Lithium mass vaporized (integral) from wetted wall during initial interaction with pellet.

Appendix C, the equation for this operating line is given by:

$$\frac{I}{V} = \frac{P_V}{T_V} \left[ \frac{H_V - E_0}{R} + \int_{T_V}^T \frac{dT}{\gamma - 1} \right] = 11.9 \frac{\text{MJ}}{\text{m}^3}. \quad (4)$$

By extrapolating the energy flow values from Section II.B.2, the temperature is less than 6000 K at 0.01 s; therefore, the operating line (Eq. 4) is plotted on the pressure-temperature diagram in Fig. 6 over the probable range of temperatures. (The development of the pressure-temperature diagram is also given in Appendix C.) As shown in Fig. 6, the insensitivity of the assumed cavity equilibration conditions is indicated by the relatively small pressure variation over the temperature range. This insensitivity will be further demonstrated later.

#### b. Cavity Blowdown

The pressure decay in the cavity can be calculated analytically by assuming an adiabatic expansion of the gas in the cavity through a choked nozzle. The equation for the cavity expansion is

$$V \frac{dp}{dt} = -\dot{M}, \quad (5)$$

and for sonic flow at the nozzle throat

$$\dot{M} = PA \sqrt{\frac{\gamma}{RT}} \left( \frac{2}{\gamma+1} \right)^{\frac{\gamma+1}{\gamma-1}} \quad (6)$$

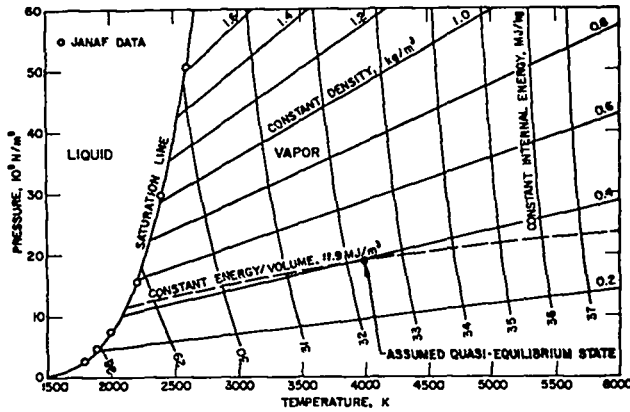


Fig. 6. Locus of quasi-equilibrium cavity conditions prior to exhaustion of cavity gases.

By applying the isentropic relations

$$\frac{P}{P_0} = \left(\frac{\rho}{\rho_0}\right)^\gamma \quad (7)$$

and

$$\frac{T}{T_0} = \left(\frac{\rho}{\rho_0}\right)^{\gamma-1}, \quad (8)$$

the analytic expression

$$\frac{\rho}{\rho_0} = \left(1 + \frac{\gamma-1}{2} \frac{t}{\tau}\right)^{-\frac{2}{\gamma-1}} \quad (9)$$

is obtained, where  $\tau$  is the time constant. The time constant is  $M_0/\dot{M}_0$ , where  $M_0$  is the initial mass in the cavity and  $\dot{M}_0$  is evaluated at the initial pressure and temperature.

By assuming that the pressure decays to  $133 \text{ N/m}^2$  (1 mm Hg) in 1.0 s,  $\tau$  and  $A$  can be calculated with Eqs. 6, 7, and 9. Results of such calculations over the probable cavity temperature range are shown in Table I. The insensitivity of the assumed cavity equilibration conditions is further indicated by the small variation in nozzle diameter over the temperature range. Therefore, the cavity equilibration temperature is arbitrarily assumed to be 4000 K; the corresponding pressure is  $18.9(10)^5 \text{ N/m}^2$  and the corresponding mass of vaporized lithium is 1.65 kg.

The resulting pressure, temperature, and density profiles for the adiabatic expansion at an initial temperature of 4000 K are shown in Fig. 7.

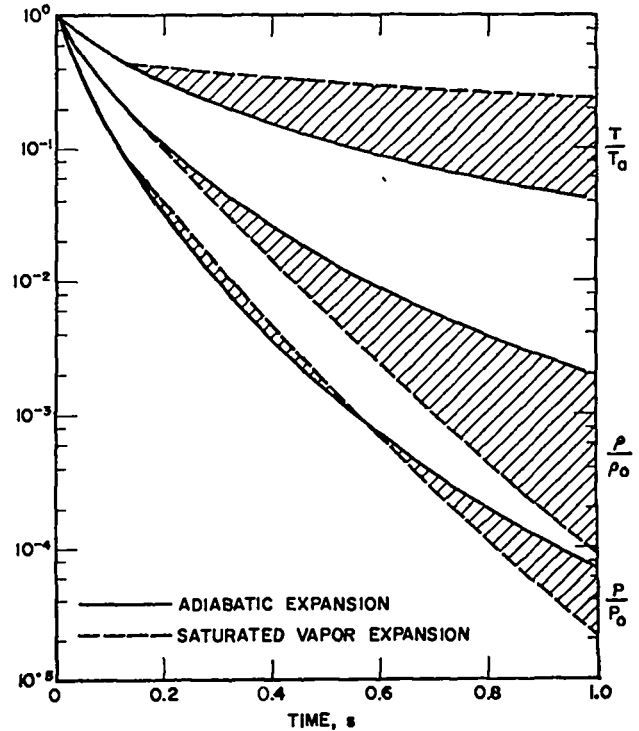


Fig. 7. Cavity conditions during blowdown;  $P_0 = 18.92 \times 10^5 \text{ N/m}^2$ ,  $T_0 = 4000 \text{ K}$ ,  $\gamma = 1.52$ , and nozzle diameter = 0.235 m.

These results assume that the lithium within the cavity expands as a perfect gas; but, if the pressure decreases below the saturation pressure at any point, condensation may occur and the subsequent expansion might not be adiabatic. If the expansion were to follow saturation conditions, it would begin at 0.13 s where the temperature is equal to the saturation temperature at the corresponding pressure, and subsequent profiles would follow the saturated vapor expansion curves shown in Fig. 7.

The different results for adiabatic and saturated expansion indicate that condensation would decrease the density during blowdown. However, experience at LASL with nozzle expansions of lithium indicate that a high degree of supersaturation results, and condensation does not occur.<sup>(3)</sup> Therefore, an assumption of adiabatic expansion may be more realistic and, for this analysis, is conservative because the densities within the cavity remain higher.

TABLE I

CAVITY CONDITIONS AND NOZZLE DIAMETER  
 FOR ENERGY = 50 MJ AND CAVITY VOLUME = 4.189 m<sup>3</sup>

Initial Temperature, K	Mass Vaporized, kg	Initial Pressure, 10 <sup>5</sup> N/m <sup>2</sup>	Nozzle Diameter, m
2500	1.838	13.14	0.259
3000	1.776	15.24	0.250
4000	1.654	18.92	0.235
5000	1.528	21.85	0.220
6000	1.385	23.77	0.203

#### 4. Condensation of Cavity Exhaust Gases

##### a. General

During cavity blowdown through the sonic nozzle, the downstream pressure to the "throat" must be low enough to maintain sonic flow at the throat, i.e., the cavity-to-throat pressure ratio must be maintained at the critical pressure ratio. This condition will be maintained if the downstream duct area is divergent, thus providing a supersonic nozzle or diffuser, and if the downstream pressure is sufficiently low. As the lithium vapor expands in the diffuser, the state conditions will eventually come to the point of condensation, even though highly supersaturated. The amount of supersaturation to be expected prior to condensation is unknown, but, as pointed out earlier, lithium condensation has not been achieved in supersonic-diffuser flow experiments. In any case, should condensation occur, a condensation shock will form in the diffuser at that point and the subsequent expansion will proceed at equilibrium saturation conditions.

The condensation can be predictable and controlled if liquid droplets are injected into the vapor stream, thus making the condensation process independent of the formation of liquid nuclei. If the droplets are small enough (< 10 μm), the liquid phase will act hydrodynamically as a gas. The large surface area-to-void volume ratio of the liquid-phase particles enhances very high energy transfer and mass-transfer rates between the two phases, so that these transfer phenomena occur essentially at equilibrium, i.e., are not time-dependent.

Therefore, under these conditions, the phenomenology of condenser processes is as follows: The superheated lithium vapor enters the condenser at supersonic velocity. Momentum is transferred between the two phases, so that their velocities very rapidly become equal. Because the liquid-phase mass is much larger than that of the gas phase and the gas-phase velocity is much larger than that of the liquid phase, the momentum balance requires a large void fraction (ratio of gas to total volume) to prevent choking the flow in the condenser. During the acceleration of the liquid phase, the liquid is heated and the gas is cooled because of the high energy transport rate. At first the gas pressures are higher than the corresponding vapor pressures, so that no vaporization occurs. When the gas pressure decreases to less than the corresponding vapor pressure, vaporization occurs until the volume becomes saturated. Passage of the gas phase then proceeds at the equilibrium saturation condition, with vaporization or condensation dependent upon the ratio of fluid pressure to vapor pressure; i.e., vaporization occurs at a ratio less than unity (< 1.0) and condensation occurs at a ratio greater than unity (> 1.0). At the condenser exit, the gas and liquid phases are at equilibrium saturation, moving at supersonic velocity, with most of the mass in the liquid phase. The exiting jet is decelerated through turbulent mixing with an injected lithium stream, and the kinetic energy of this mixture is then absorbed by impacting in a stagnant pool of lithium of greater depth (greater gravitational head) than the kinetic head of the mixture.

A conceptual illustration of the condenser system is shown in Fig. 8. The atomized spray is injected from a recirculating loop of the lithium pool and is independent of the main heat-removal loop of the condenser system. The return stream of the main heat-removal loop is injected downstream to the exiting jet to provide deceleration turbulence prior to impingement with the lithium pool.

Analysis of the time-dependent events within the condenser section is based on a solution of the one-dimensional differential equations for the conservation of mass, momentum, and energy, including change-of-state processes and mass and energy transfer between the two phases.

The hydrodynamic conservation equations in the Eulerian-space coordinate system, with corrections for area changes, are:

$$\frac{\text{Mass, gas phase}}{\lambda t} \frac{\partial \rho}{\partial t} = - \left[ U \frac{\partial \rho}{\partial x} + \rho \frac{\partial U}{\partial x} + \frac{\rho U}{\chi A} \frac{\partial (\chi A)}{\partial x} \right], \quad (10)$$

$$\frac{\text{Mass, liquid phase}}{\lambda t} \frac{\partial M_l}{\partial t} = - \left[ U \frac{\partial M_l}{\partial x} + M_l \frac{\partial U}{\partial x} + \frac{M_l U}{(1-\chi)A} \times \frac{\partial A(1-\chi)}{\partial x} + \frac{\partial M_s}{\partial t} \right], \quad (11)$$

$$\frac{\text{Momentum, combined phases}}{\lambda t} \frac{\partial U}{\partial t} = - \left[ U \frac{\partial U}{\partial x} + \frac{1}{\rho_T} \frac{\partial (P+Q)}{\partial x} \right], \quad (12)$$

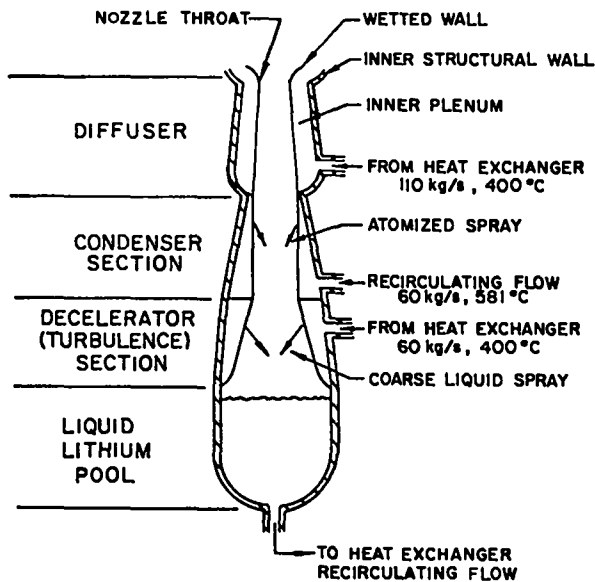


Fig. 8. Concept for supersonic spray condenser.

$$\frac{\text{Energy, gas phase}}{\lambda t} \frac{\partial E}{\partial t} = - \left[ U \frac{\partial E}{\partial x} + \frac{(P+Q)}{\rho} \frac{\partial U}{\partial x} \right], \quad \text{and} \quad (13)$$

$$\frac{\text{Energy, liquid phase}}{\lambda t} \frac{\partial E_l}{\partial t} = - U \frac{\partial E_l}{\partial x} + \frac{\partial E_s}{\partial t}, \quad (14)$$

where  $\rho_T$  is the combined gas and liquid-phase density (total mass per unit volume);  $U$  is either the gas or the liquid-phase velocity (which remain equal to one another from the equilibrium momentum exchange); the void fraction,  $\chi$ , is the ratio of gas volume to total volume; and  $\partial M_s/\partial t$  and  $\partial E_s/\partial t$  are the mass and energy source terms, respectively, for the injected liquid spray.

This system of equations is solved as an initial-value problem by a finite-difference technique; the equations are integrated in space for an incremental time cycle as described in Appendix B.

The mass and energy balances for the transport processes are: for energy transport prior to saturation,

$$M_l C_p \Delta T_l = M_v C_v \Delta T_v, \quad (15)$$

and for mass and energy transport after saturation,

$$M_l C_p \Delta T_l + M_{vc} \Delta H_v = M_v C_v \Delta T_v, \quad (16)$$

$$\Delta M_l = M_{vc}, \quad (17)$$

$$\rho_v = \rho + \frac{M_{vc}}{A \chi \Delta x} = \frac{P_{vp}}{RT_{vp}}, \quad (18)$$

$$\chi = 1 - \frac{M_l + M_{vc}}{\rho_l A \Delta x}, \quad (19)$$

where  $M_{vc}$  is the mass transported between phases,  $\Delta H_v$  is the latent heat of vaporization, the subscript  $l$  denotes liquid phase, the subscript  $v$  denotes gas phase, and the subscript  $vp$  denotes saturated conditions. In these latter five equations, if  $P = \rho RT > P_{vp}$ , condensation occurs and  $M_{vc}$  is negative; if  $P = \rho RT < P_{vp}$ , vaporization occurs and  $M_{vc}$  is positive. The equation-of-state for the gas phase is

$$P = (\gamma - 1) \rho E, \quad (20)$$

and follows the saturation line (see Appendix C) after saturation.

#### b. Cavity Blowdown Without Liquid Spray

The time required to achieve isentropic flow conditions has been determined by a calculation of the cavity blowdown with the above system of equations, without the liquid phase. The geometric mesh for the calculation included the cavity and the diffuser. The calculation was carried out to 0.1 s for initial conditions of  $18.9(10)^5 \text{ N/m}^2$  and 4000 K in the cavity, and of  $1.8 \text{ N/m}^2$  and 800 K in the nozzle. After  $\sim 1.0 \text{ ms}$ , a quasi-equilibrium is established and the flow process becomes essentially isentropic. A comparison of the cavity conditions as calculated by this time-dependent method and those calculated by the equilibrium method (adiabatic expansion in Section II.B.3) indicate slightly lower densities calculated by the time-dependent method. This is a reasonable result because the cavity conditions remain stagnant for the equilibrium calculation, whereas flow conditions within the cavity are calculated by the time-dependent calculation.

#### c. Cavity Blowdown with Liquid Spray

For a typical calculation, the initial conditions are  $18.9 \text{ N/m}^2$  and 4000 K within the cavity and "choked" flow within the converging section to the throat;  $1.8 \text{ N/m}^2$  and 800 K within the diffuser and condenser sections; and a steady state flow distribution of the liquid phase with a constant mass flow rate per unit area and the void fraction varying from 1.0 at the inlet to 0.75 at the exit of the condenser section. The geometry for this calculation consists of a diffuser length of 1.0 m with an outlet-to-inlet area ratio of 2.0, and a condenser length of 1.0 m with a constant area. The "Eulerian mesh" consists of 200 zones (1.0 cm each).

The time-dependent calculation includes the flow conditions within the diffuser and the condenser, and the cavity and throat conditions are calculated by the equilibrium method because of the rapid achievement of the isentropic conditions.

This typical calculation has been carried out to 0.02 s, at which time a quasi-equilibrium condition is established. The initial shock passes through the condenser in  $\sim 3.0 \text{ ms}$ , during which time the liquid phase is accelerated to  $\text{Mach} \approx 2$ .

At 0.02 s, the temperature and pressure profiles through the condenser are as shown in Figs. 9 and 10, respectively. At this time the following conditions exist through the duct. Within the first  $\sim 2.0 \text{ cm}$  the gas is cooled and the liquid is heated with no vaporization or condensation occurring; at  $\sim 2.0 \text{ cm}$  the liquid is heated to saturation and vaporization begins; at 8.0 cm condensation begins; and at 30.0 cm the gas phase is fully "quenched" to the liquid-spray temperature and pressure.

The kinetic head of the exiting jet from the condenser section is  $\sim 1.6 \times (10)^6 \text{ N/m}^2$  with a density of  $\sim 0.1 \text{ kg/m}^3$  and a velocity of  $\sim 4000 \text{ m/s}$ . This kinetic head is reduced to that equivalent to a gravity head of 1.0 m of lithium ( $\sim 4700 \text{ N/m}^2$ ) by turbulent mixing with an injected liquid spray to a density of  $8.5 \text{ kg/m}^3$  and a velocity of  $\sim 24 \text{ m/s}$ . A detailed analysis of this final mixing process is beyond the scope of this report.

#### 5. Wetted-Wall Protective Layer Formation

Protection from the initial high pellet-energy fluxes is afforded by the formation of a layer of liquid lithium on the inside surface of the wall prior to the initiation of the energy pulse. The minimum thickness of this layer is determined by that amount of lithium that could be vaporized by the deposited pellet energy (50 MJ); this amount of lithium is  $\sim 2.5 \text{ kg}$ , corresponding to a layer thickness of  $\sim 0.4 \text{ mm}$ . Results of calculations describing the interaction between the pellet and wetted-wall layer, presented in Section II.B.2, indicate that only  $\sim 0.5 \text{ kg}$  of lithium is vaporized during the interaction time of  $\sim 1.0 \text{ ms}$ . It is conservatively assumed that a minimum thickness of 1.0 mm is sufficient to protect the wall surface from exposure during the pulse cycle.

The layer is formed on the inside surface of the wetted wall by accumulation of the radial inflow of blanket lithium through the porous wall. It is assumed that the flow impedance within the wall can be tailored for any desired flow distribution. During the pulse cycle, this flow will cease until the cavity pressure decreases below the blanket pressure (assumed to be of the order of 1 atm). As shown in Fig. 7, the cavity pressure decreases to less than 1.0 atm at  $\sim 0.2 \text{ s}$  after

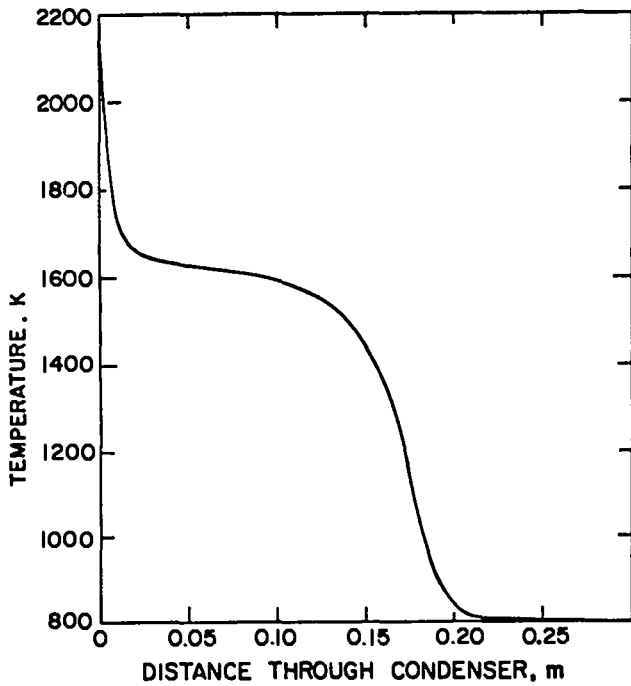


Fig. 9. Temperature distribution in spray condenser 0.02 s after pellet initiation.

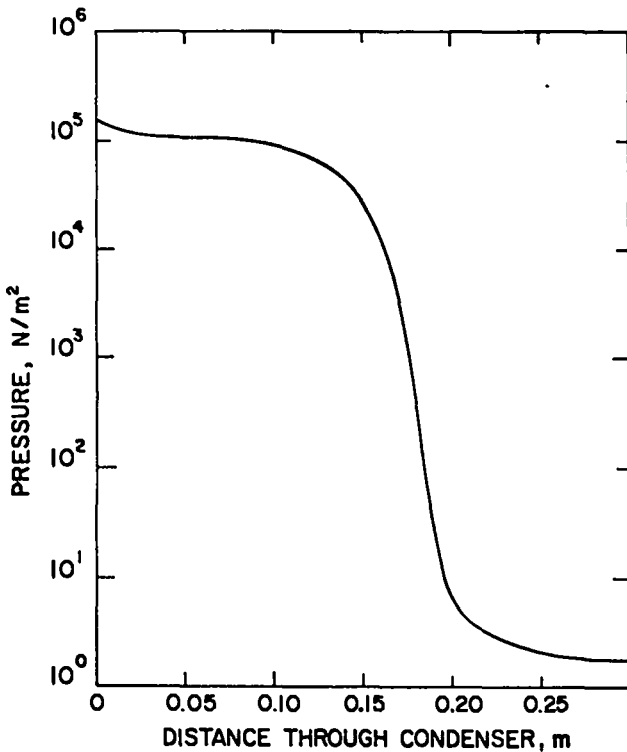


Fig. 10. Pressure distribution in spray condenser 0.02 s after pellet initiation.

pulse initiation; therefore, ~ 0.8 s is available for the formation of the layer.

During the collection and formation of the layer, the forces acting to alter its uniformity are gravity, surface tension, the fluid viscous force, and any imposed pressure gradients within the cavity or along the wall surface of the layer. The equation of motion, assuming constant density and unidirectional flow tangent to the inner spherical surface, is:

$$\frac{\partial p}{\partial l} + \rho U \frac{\partial U}{\partial l} - \rho g \frac{\partial h}{\partial l} + F_D = -\rho \frac{\partial U}{\partial t}, \quad (21)$$

where  $\partial l$  is the circumferential increment along the direction of flow and  $F_D$  is the viscous drag force. The surface-tension force does not appear in this relationship because this force is always normal to the tangent of the radius of curvature, i.e., in this case normal to the direction of flow; and, for this analysis, it is assumed that the surface-tension force is always counterbalanced by a force derived from the ability of the liquid to support tension through an internal stress mechanism.\* This assumption is valid where the radius of curvature is large (the order of centimeters) and negative, i.e., such that the surface-tension force is directed toward the center of the sphere. In the upper hemisphere, should the radius of curvature become positive and small, the surface may become unstable, and a droplet may form and fall from the surface.

Because of the ability of lithium to support tension, a static (velocity = zero everywhere) layer with a thickness of the order of millimeters could be formed if pressure gradients are established that equal the gravitational gradients. However, at the steady state flow condition, where the velocity distribution is fully developed, the layer thickness will be minimum. Although the steady-state condition will probably not be achieved during a pulse cycle, an analysis of this condition, which results in a minimum thickness of 1.0 mm, should ensure that a lithium layer of sufficient thickness is formed.

\* The ability of molten lithium to support tension has been observed in high-temperature heat-pipe research.<sup>(4)</sup>

For this analysis, the mass-continuity equation with constant fluid density is:

$$\rho \partial(UA_\ell) + \partial \dot{m} = 0, \quad (22)$$

where  $A_\ell$  is the cross-sectional area of the tangential flow and  $\dot{m}$  is the radial inflow through the porous wall. Assuming that the wall impedance to the radial inflow is such that the pressure gradients are zero, the equation of motion (Eq. 21) at steady state becomes

$$\rho U \frac{\partial U}{\partial \ell} - \rho g \frac{\partial h}{\partial \ell} + F_D = 0. \quad (23)$$

Because the layer thickness is small, the flow is laminar and the drag force may be expressed by the Hagen-Poiseuille relation,

$$32 \frac{\ell \mu U}{D_t^2},$$

where  $\ell$  is the circumferential distance along the flow path and  $D_t$  is the layer thickness. Equation 23 then becomes

$$U \partial U - g \partial h + \frac{32 \ell \mu U}{\rho D_t^2} = 0. \quad (24)$$

If the radial inflow is uniform, the source in Eq. 22 becomes

$$\partial \dot{m} = \frac{\dot{M} \partial A_r}{4 \pi r^2}, \quad (25)$$

where  $\dot{M}$  is the total radial inflow,  $r$  is the cavity radius, and  $\partial A_r$  is the incremental inside surface area of the wall. If  $\partial h$  and  $\partial A_\ell$  are expressed as functions of layer thickness, the three equations (Eqs. 22, 24, and 25) may be integrated simultaneously, giving the velocity and thickness distribution of the layer.

Results of this integration for radial inflow rates of 1.0, 2.0, 5.0, and 10.0 kg/s are presented in Fig. 11. These results indicate that a radial inflow of somewhat less than 5.0 kg/s will provide a minimum thickness of 1.0 mm. The greater thickness near the top of the upper hemisphere is undesirable because of the positive radius of curvature, but this may be alleviated by "tailoring" the wall impedance in this area to reduce the radial inflow of lithium. Because the velocities

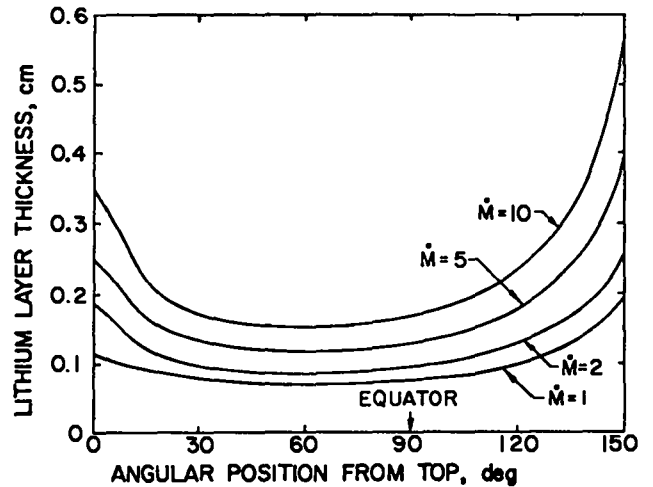


Fig. 11. Lithium layer thickness at steady-state flow conditions with uniform radial inflow through wetted wall.

are of the order of tenths of a meter per second, the steady-state condition will not be achieved; in any case, there will probably not be sufficient time for a droplet to form before the next pulse is initiated. The important point is that a sufficient amount of lithium be collected on the inside surface during the approximately 0.8 s of reduced pressure in the pulse cycle. Therefore, the crucial design parameter in the formation of the protective layer is the wall internal impedance to the radial inflow of lithium.

### C. THE BLANKET

#### 1. Introduction

The physical effects resulting from energy deposition, requiring specific analysis, are:

- Removal of Deposited Energy - Because the deposited energy in the liquid lithium is removed by circulating it through an external heat exchanger, the temperature distribution in the blanket is determined by the lithium flow rate and by the distribution of deposited energy. The deposited energy within solid walls is removed by conduction to the liquid as it flows in contact with wall surfaces.
- Structural Wall Response - The inner structural wall and the outer pressure-vessel wall will be stressed by the cyclic strains which result from pressure forces within the cavity and from forces

within the liquid-blanket regions. These stresses must not exceed the limitations of the material.

## 2. Removal of Deposited Energy

### a. General

For a temperature increase of 350 K in the blanket lithium, the flow rate is 104.2 kg/s, for a total energy of 152.4 MJ deposited once each second. This flow passes through the inner structural wall and the main-pressure-vessel wall during transit through the ICTR.

The analyses of the heat-transport processes within the liquid lithium and structural walls are based on solutions of the classical differential equation for heat conduction (diffusion), with a convection term added. For spherical symmetry, the one-dimensional equation with constant mass flow rate is

$$\rho C_p \frac{\partial T}{\partial t} = \frac{k_t}{r^2} \frac{\partial}{\partial r} \left( r^2 \frac{\partial T}{\partial r} \right) + q - \frac{\dot{M} C_p}{4\pi r^2} \frac{\partial T}{\partial r} \quad (26)$$

where the convection term is the last term of this equation.

### b. Temperature Distribution in Blanket

The volumetric heat-generation rates (q-term in Eq. 26) were calculated from the energy deposition values given in Table A-III, Appendix A. Using these heat-generation rates, the temperature distribution in the lithium between the inner structural wall and the main-pressure-vessel wall was calculated by a numerical solution of Eq. 26 for successive pulses until the steady state condition ( $\partial T/\partial t = 0$ ) was attained. These results, presented in Fig. 12, indicate that heat transport by conduction is negligible and that ~ 100 pulses are required to attain steady state.

The steady-state solution of Eq. 26, neglecting the conduction term, yields the distribution through the blanket region shown in Fig. 13. The possibility of mixing by natural convection currents could alter this distribution, probably increasing the temperatures within each liquid region to near the exit temperature of that region; but, because the radial outflow through the walls is uniform, this possibility would not alter the wall temperatures.

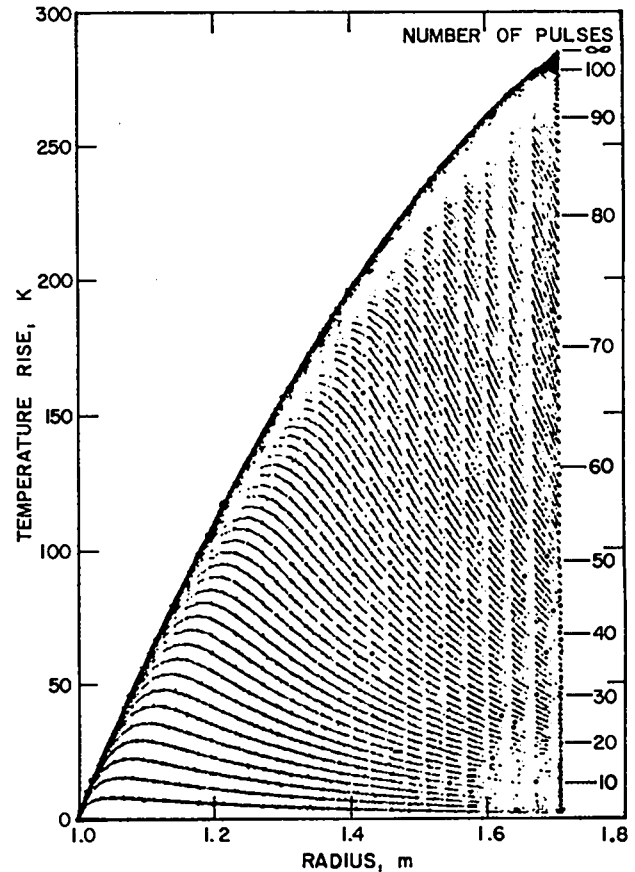


Fig. 12. Temperature distributions in blanket between structural walls for successive energy pulses

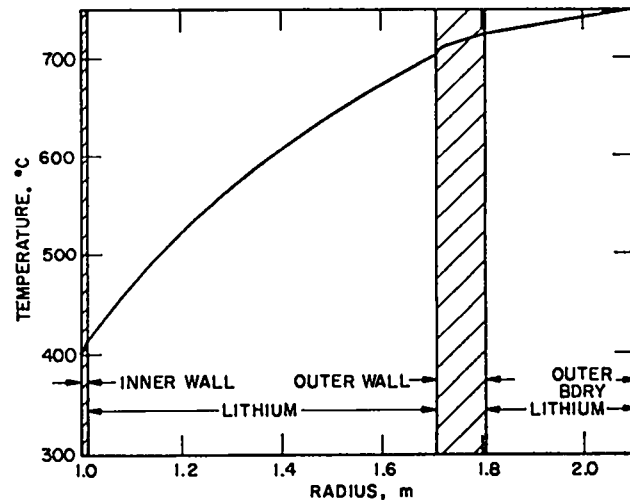


Fig. 13. Steady-state temperature distribution through lithium blanket system.

The "tailoring" of the wall impedances for uniform radial outflow obviates the need for internal structure within the lithium regions to maintain the radial outflow.

c. Heat Removal in Porous Wetted Wall

The resulting temperature distributions (by steady-state solutions of Eq. 26) through the wetted wall, with the inner and outer surfaces of the wall at constant temperature, are presented in Fig. 14 for lithium flow rates of 3 and 10 kg/s. Because of the low lithium flow rates (sufficient only to re-form the protective layer), the principal mechanism of heat removal from this wall is by radial conduction; this is indicated by the small difference between the temperature distributions at the two flow rates. Another calculation, with the inner-wall surface as an adiabatic boundary, resulted in a maximum temperature difference of 67 K. This means that the outer-wall surface must be cooled by the flowing lithium within the plenum between the wetted wall and the inner structural wall; otherwise, the wall material may overheat. The inside surface is cooled by vaporization of the protective lithium layer, but it may not be at the same temperature as the outside surface.

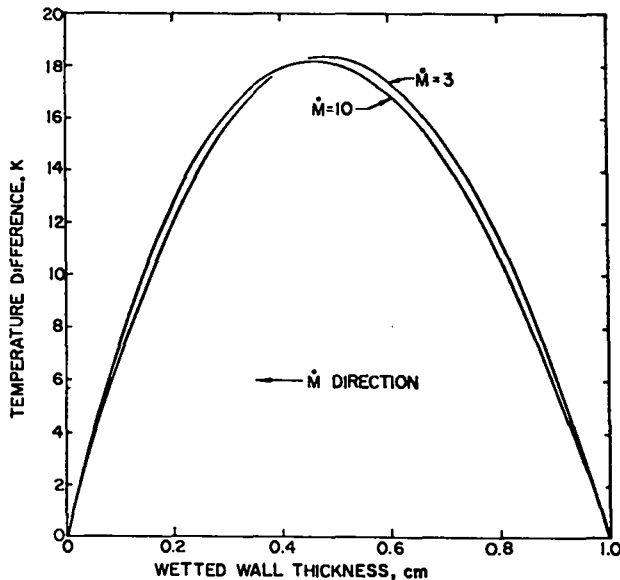


Fig. 14. Steady-state temperature distributions through wetted wall for radial inflow rates of 3 and 10 kg/s; inner and outer wall surfaces at constant temperature.

d. Heat Removal in the Structural Walls

The thicknesses of the inner and outer (main-pressure-vessel) structural walls, which are determined by the structural analyses in Section II.C.3, below, are too large for conduction of the deposited heat to the inner and outer wall surfaces. Therefore, this heat must be removed by the lithium that flows through the walls. If the passages for this lithium flow are arranged uniformly over the spherical surface, the dominant temperature gradients will be tangential, between the passages. A conventional design for such passages is a triangular array of holes, passing radially through the walls. Results from calculations of temperature gradients for various hole sizes and void fractions in triangular arrays are presented in Fig. 15. The calculation assumes no radial conduction and a constant temperature around the surface of the holes. The resulting temperature gradient is the difference between the temperature at the adiabatic center between the holes and that at the hole surface.

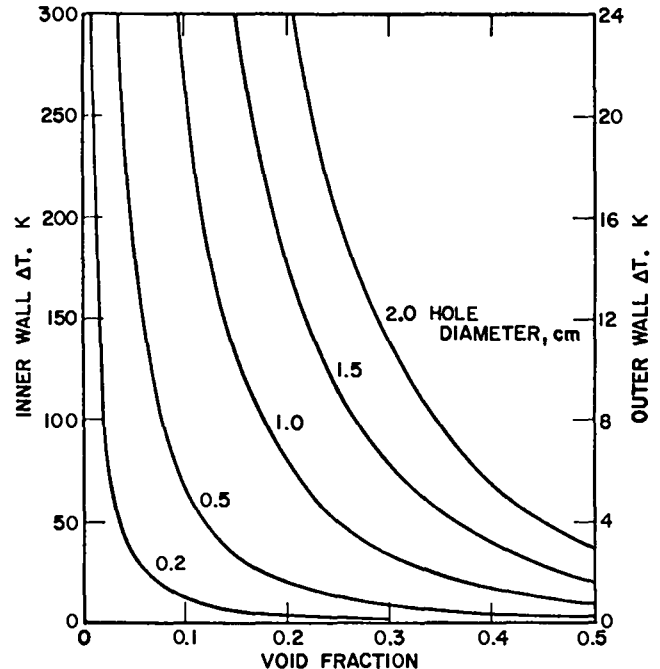


Fig. 15. Maximum steady-state temperature difference between coolant holes through structural walls; holes in triangular array.

The structural design criteria for these passages will be to limit the thermal stresses resulting from the temperature gradients and to limit the void fraction so that the wall strength is not impaired. As discussed in Section II.C.3, below, a temperature gradient of 50 K is easily accommodated. For the inner wall, a coolant-hole diameter of 0.25 cm and a void fraction of 0.05, corresponding to a spacing of 1.06 cm between centers, might fulfill these criteria. For the outer wall, a 0.9-cm-diam hole and a void fraction of 0.05 would give a 50-K gradient and a hole spacing of 3.8 cm.

#### e. Flow Impedance through Walls

Because the cooling of the inner and outer structural walls is by conduction to the lithium flowing through these walls, it is essential that this flow be uniformly distributed around the sphere. This can be accomplished by making the flow impedance such that the pressure losses through the wall are significantly higher than the total pressure changes within the lithium blanket regions. A reasonable assumption for this pressure loss is of the order of  $10^4$  N/m<sup>2</sup>, because the kinetic energy changes within these regions will necessarily be small. A means of supplying such a flow restriction could be the placement of orifices in the coolant holes through the wall. For the inner wall, an orifice with a diameter of ~ 0.08 cm in each coolant hole would provide a pressure loss of ~  $10^4$  N/m<sup>2</sup>. For the outer wall, an orifice diameter of ~ 0.22 cm would provide this impedance.

The flow impedance of the wetted wall is "tailored" to provide the desired protective-layer thickness on the inside surface. Although the flow distribution will be essentially uniform, this is not for the purpose of cooling the wall. The major difference between the flow impedance of this wall and that of the structural walls is that the friction pressure loss of the wetted wall must be higher by at least a factor of 10. The pressure in the plenum between the wetted wall and the inner structural wall will be of the order of  $10^5$  N/m<sup>2</sup> (1.0 atm), and the pressure in the cavity will be less than  $10^3$  N/m<sup>2</sup> during the last 0.5 s of the pulse cycle. Because this wall does not restrain any pressure forces, it is not subjected to significant stress loads although it must behave elastically due to the

hydrodynamic and probable mechanical coupling with the inner structural wall. Therefore, the wall may be porous, with an intricate internal structure to establish this high-impedance flow path. Possibilities for such structures are sintered metals or a wire-wound shell.

### 3. Structural-Wall Response

#### a. General

The pressure forces from the cavity tend to move the walls outward, but the pressure forces within the liquid (generated through the hydrodynamic coupling between the walls and the lithium expansion caused by neutron heating) and the wall-restraining forces cause a high-frequency oscillation (ringing) of both walls. This ringing is superimposed on the cyclic motion from the once-per-second energy pulse. Because the stresses are cyclic with a corresponding high-frequency ringing during each cycle, it is quite apparent that for any reasonable vessel lifetime the mode of failure will be that of fatigue.

#### b. Material Compatibility with Lithium

A conservative approach has been taken to investigate materials of high purity or known corrosion properties. Many alloys having higher strength and fatigue properties may find application; however, their corrosion properties would need further investigation.

Based on experimental data,<sup>(5)</sup> materials compatible with lithium in the temperature range of interest are the austenitic stainless steels, the refractory metals, iron-chromium alloys, and pure iron. Of these materials, the austenitic stainless steels are less expensive to fabricate; therefore, this material is preferable if grain-boundary attack does not alter the structural properties prohibitively.

Mass transfer of stainless steel in lithium appears to be a minor problem at 540°C, with only very minor grain-boundary attack, 0.0015 in. occurring in 3000 h of a dynamic test at one cycle per minute.<sup>(5)</sup> Based on these data, stainless steel should be acceptable for the inner wall at 400°C. However, a significant amount of grain-boundary attack and mass transfer would be expected for the

stainless-steel pressure-vessel wall at 700°C for extremely long operating times, and greater mass transfer than indicated by data for one-cycle-per-minute tests would be expected for the continuously operating system. The refractory metals pose a significantly smaller corrosion and mass-transfer problem; but, as will be discussed later, the decrease in strength of the stainless steel caused by corrosion is probably insignificant.

One of the major materials problems will remain that of maintaining adequate corrosion resistance in parent materials, welds, and brazes necessary for fabrication of the walls.

### c. Wall Strains

The analysis of wall strains is based on the boundary motion of the liquid, as determined from the solution of the hydrodynamic equations for conservation of mass, momentum, and energy. The equations are formulated for one-dimensional spherical geometry in the Lagrangian-space coordinate system. The equations for mass and momentum conservation are identical to Eqs. 1 and 2 of Section II.B.2, above. The conservation of energy equation is

$$\frac{\partial E}{\partial t} = - (P + Q) \frac{\partial v}{\partial t} . \quad (27)$$

The equation-of-state for liquid lithium, developed from definitions of the adiabatic compressibility factor and the volumetric coefficient of thermal expansion (see Appendix C) is

$$P = \frac{(\rho - \rho_0)}{\rho \beta_c} + \frac{\beta_T}{\beta_c} \frac{E}{C_p} , \quad (28)$$

where  $\rho_0$  is the reference density of 507 kg/m<sup>3</sup> at 473 K. Pressures in this equation are restricted to a minimum of 200 N/m<sup>2</sup> to simulate vaporization, which will precede any significant negative pressure (fluid tension).

The restraining force of the vessel walls is accounted for by the addition of a strain term to the momentum equation at the inner and outer boundaries of the problem. The momentum equation for the problem boundaries is

$$\frac{\partial U}{\partial t} = - r^2 \frac{\partial(P+Q)}{\partial \bar{m}} + \frac{2Y D_w}{(1-\mu)} \frac{\partial r}{\partial \bar{m}} . \quad (29)$$

These equations are integrated explicitly in space and time by a finite-difference technique, as described in Appendix B.

For the calculation, the configuration is a hollow sphere, divided into 150 zones of equal thickness, with a 1.0-m inner radius and a 1.7-m outer radius. The initial conditions are determined as follows. The density distribution is found (by using Eq. 28) from the temperature distribution in Fig. 13 at a constant pressure of 10<sup>5</sup> N/m<sup>2</sup>; with this density distribution the pressure distribution, shown in Fig. 16, is determined (again from Eq. 28) by adding the energy distribution (shown in Fig. 17 and calculated from the energy deposition in Table A-III, Appendix A) to the original steady-state energy distribution.

Throughout the calculation, a pressure profile, shown in Fig 18 and derived from Fig. 4, was imposed as the inner-wall boundary condition.

The results from a typical calculation are shown in Figs. 19, 20, and 21. The wall parameters for this calculation are:  $\rho = 8000 \text{ kg/m}^3$ ,  $Y = 2 \times 10^{11} \text{ N/m}^2$ , inner-wall  $D_w = 0.01 \text{ m}$ , outer-wall  $D_w = 0.10 \text{ m}$ . The pressures in Fig. 20(a) and (b) are the pressures in the lithium zones adjacent to the walls. The outer wall initially moves outward due to the sudden lithium expansion caused by the neutron-energy deposition. The inner wall also initially moves outward, due to the impulse from the cavity pressure buildup. During these initial wall movements, the internal pressure wave from the neutron deposition moves outward at the speed of sound. At 0.18 ms (the time for sound to travel a distance of 0.7 m) the pressure wave reflects off the outer wall and returns to the inner wall at 0.36 ms. The motion of the inner wall is momentarily reversed, then continues outward due to the cavity pressure force as this first internal pressure wave dissipates. At 0.6 ms the inner-wall motion is reversed and is accelerated inward by the inner-wall restraining force coupled with the force exerted by the pressure wave that has been building up immediately behind the wall. At this time the outer wall motion also is reversed by its restraining force. The pressure wave, which originated at the inner wall, arrives at the outer wall at 0.78 ms; as the wave reflects, its intensity is amplified by

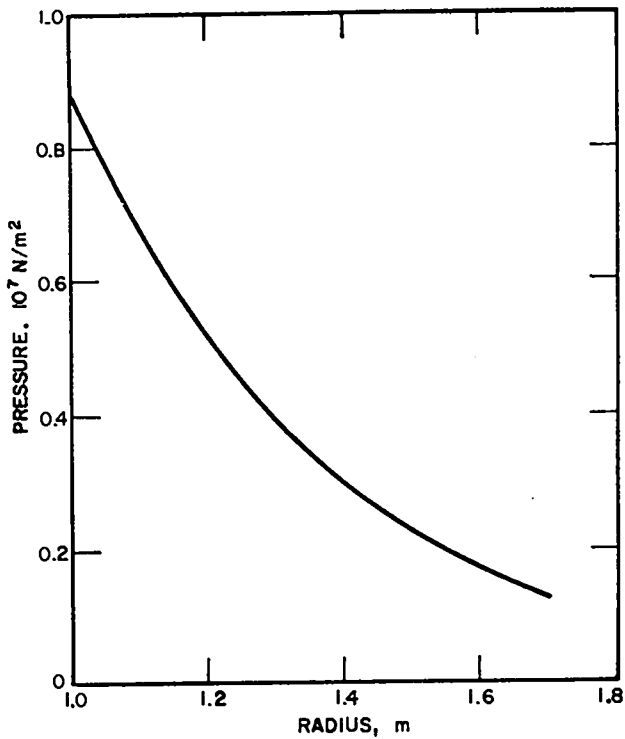


Fig. 16. Initial pressure distribution in blanket lithium resulting from neutron-energy deposition.

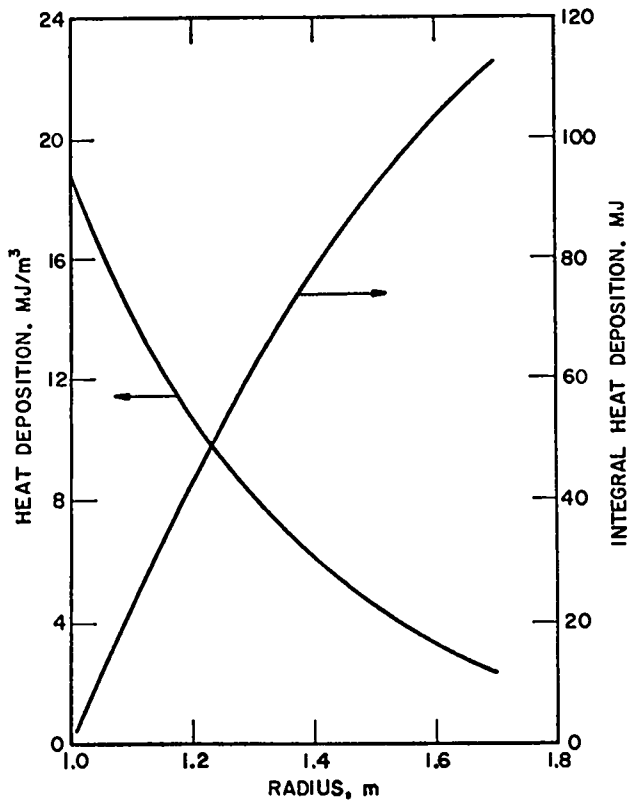


Fig. 17. Heat deposition in blanket lithium - used in wall strain analysis.

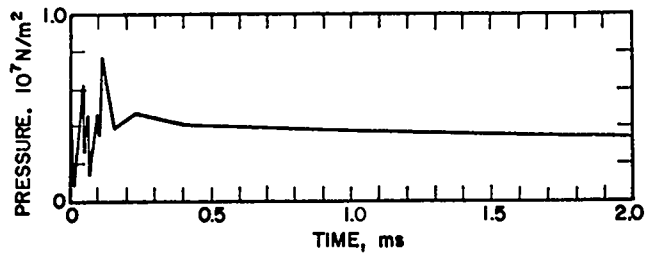


Fig. 18. Cavity pressure profile transmitted to inner wall, derived from Fig. 4.

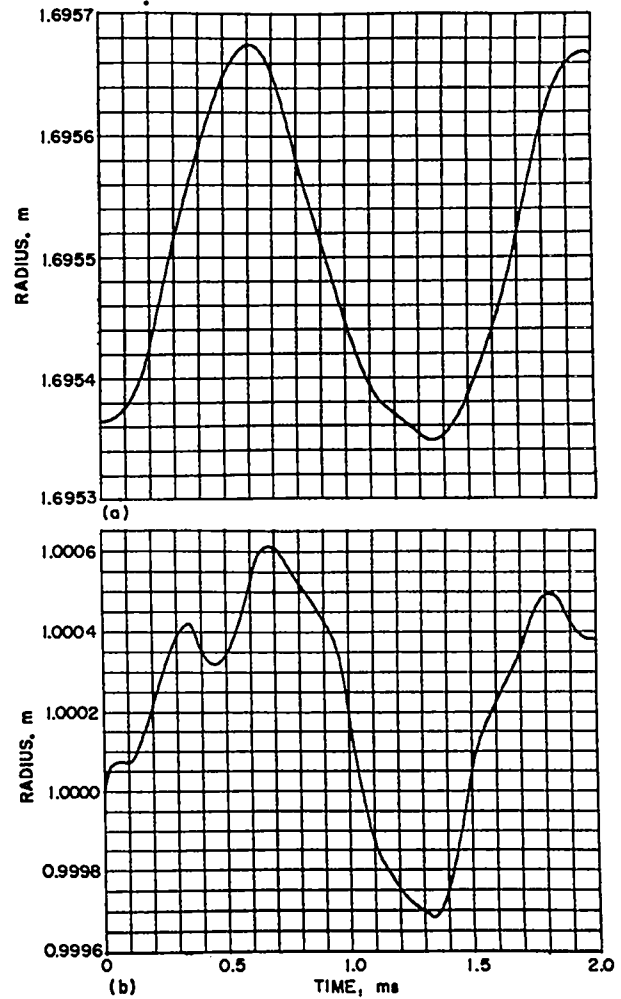


Fig. 19. Displacement of structural walls during initial period of oscillation; (a) outer wall, (b) inner wall.

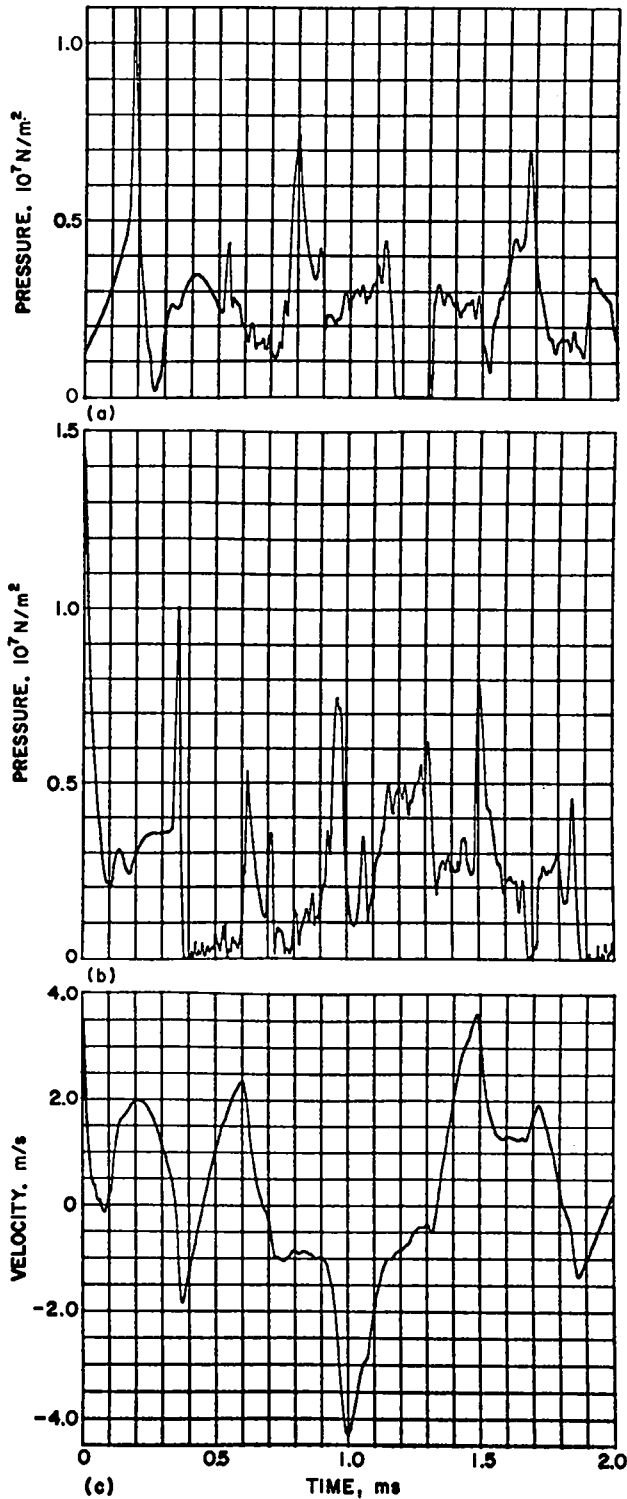


Fig. 20. Pressure in lithium zones adjacent to: (a) outer wall, (b) inner wall, (c) velocity of inner wall, during initial period of oscillation.

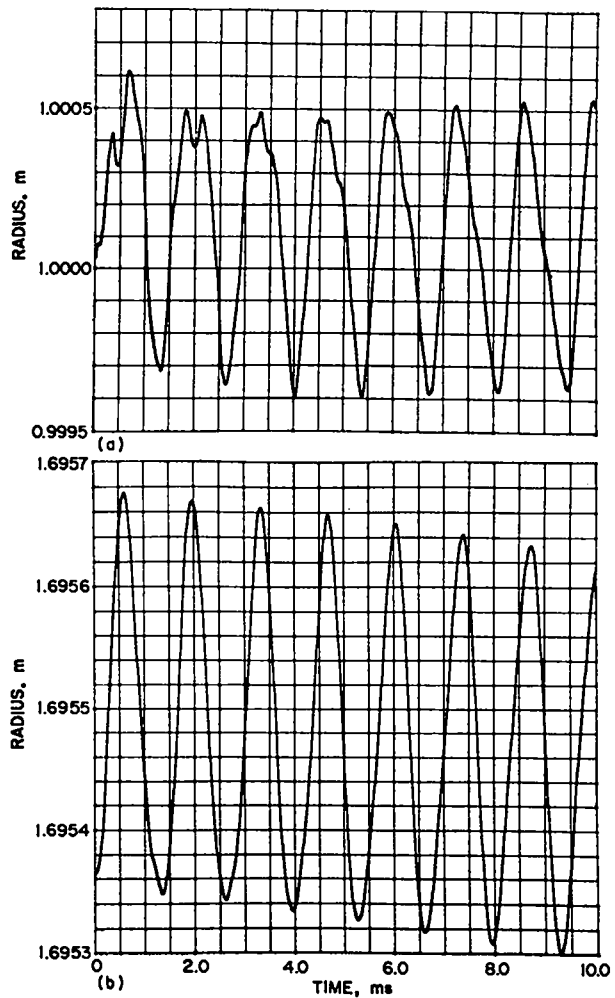


Fig. 21. Displacement of structural walls indicating oscillatory motion; (a) inner wall, (b) outer wall.

the inward motion of the outer wall. When this wave returns to the inner wall, at 0.96 ms, the wall is driven into compression and is accelerated further inward until the restraining force and the cavity pressure force again reverse the motion, accelerating the wall outward at 1.35 ms. At 1.8 ms the events, which began at 0.6 ms, are repeated, and the system continues to oscillate, driven by the natural frequency of the outer wall. This is shown by the results of a calculation to 10 ms, plotted in Fig. 21. No damping mechanism that could reduce the above motions has been provided for either wall. Damping will exist but will not significantly affect the first few cycles.

Maximum strains that result from varying the inner-wall thickness, the modulus of elasticity, and the density are shown in Fig. 22. In all cases the maximum strain occurred with the wall in tension, frequently on the second cycle. With stiffer walls (higher modulus of elasticity) the strain is less but the stress is increased. A discussion of these results will follow in the subsequent section. Density changes of the inner wall have little effect on the resulting strain.

The thickness of the outer wall was also varied to determine the effect on wall strains. These results, shown in Fig. 23, indicate that for thicker outer walls the strain is reduced in the inner wall, as well as in the outer wall.

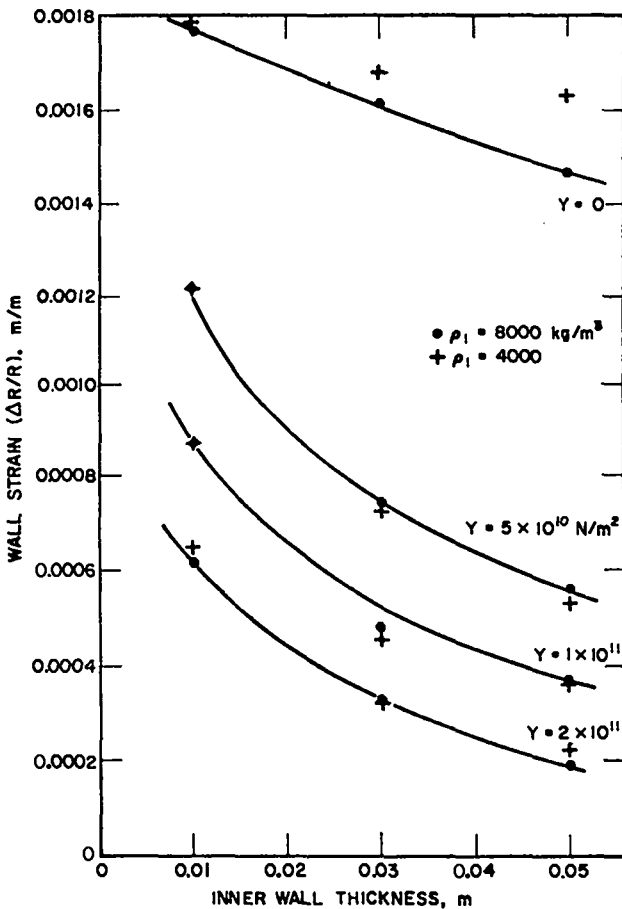


Fig. 22. Maximum strain of inner wall as a function of inner-wall thickness for various material properties (density and modulus of elasticity); outer wall parameters:  $Y = 2 \times 10^{11} \text{ N/m}^2$ ,  $\rho = 8000 \text{ kg/m}^3$ ,  $Y = 2 \times 10^{11} \text{ N/m}^2$ ; inner wall thickness = 0.01 m.

#### d. Structural Analysis

As mentioned previously, the failure mode is fatigue. To obtain a conservative comparison between imposed and allowable fatigue stresses, allowable fatigue properties obtained from the literature<sup>(6,7,8,9)</sup> were based on either  $10^7$  or  $10^8$  cycles, whichever was longest. Although  $10^7$  or  $10^8$  cycles are equivalent, respectively, to only ~100 or 1000 days of operation at one cycle per second, an extremely minor decrease in allowable fatigue properties would be expected for exposures beyond the  $10^7$  to  $10^8$  cycles. Other than the normal cyclic fatigue damage, allowable material fatigue properties will be degraded by corrosion or mass transfer and possibly by irradiation damage. The structural properties of concern are then fatigue strength and Young's modulus of elasticity. For comparison of stainless steel with prospective refractory metals, a fatigue analysis was conducted which included Ti-55, Ti-70, Zr-1.5Sn, and Nb(0.001%  $O_2$ ) as well as 300-series stainless steel. The fatigue strength and Young's modulus of these materials are shown in Figs. 24 and 25, respectively.

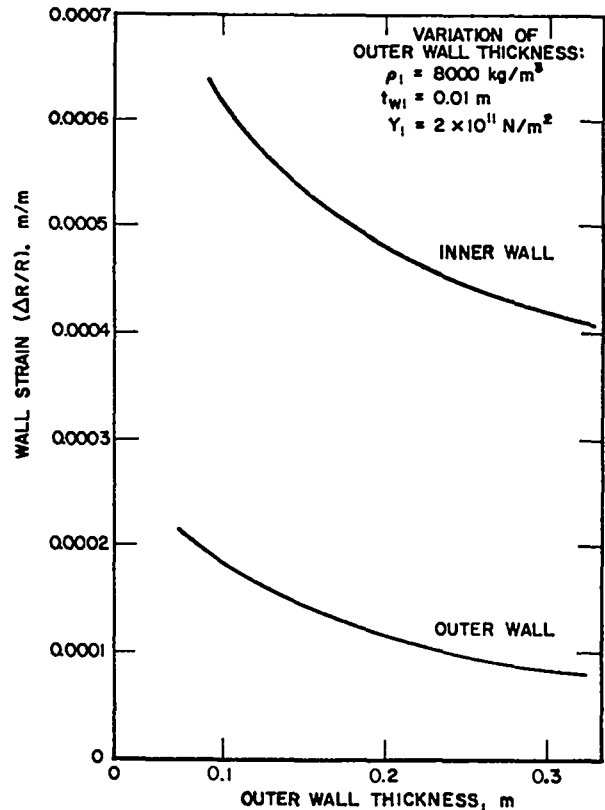


Fig. 23. Maximum wall strains as a function of outer wall thickness.

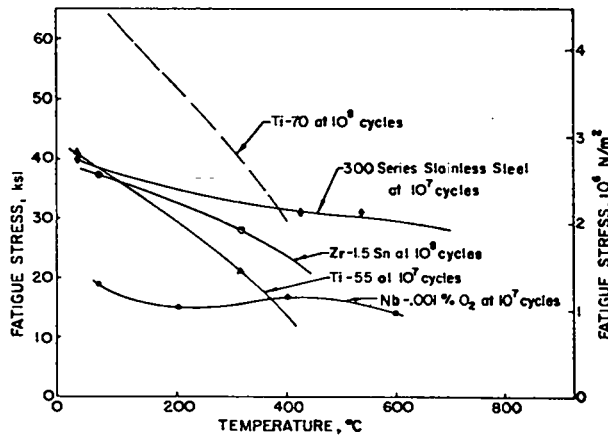


Fig. 24. Allowable fatigue-stress limits for prospective wall structural materials.

As can be seen in Fig. 22 the inner wall is subjected to a radial deflection affected primarily by the modulus and thickness of the material. Imposed stresses, plotted in Fig. 26, are calculated from these radial deflections for stainless steel, niobium, zirconium, and titanium, based on the modulus values in Fig. 25 and on a stress-concentration factor of 2.2, based on the void fraction of 0.05. The imposed stress curves have taken into account the variations in Young's modulus, Poisson's ratio, hole-stress concentrations, and the effects of ligament efficiencies of the triangular hole pattern on these properties. Allowable properties are based on published tensile-fatigue data<sup>(6,7,8,9)</sup> at  $10^7$  or  $10^8$  cycles (Fig. 24) and, for a conservative estimate, have been corrected for biaxial effects using Gough's approximation.

As can be seen from Fig. 26, the shell thicknesses required are 0.072 m for niobium, 0.043 m for stainless steel, and 0.024 m for zirconium. Two grades of commercially-pure titanium, Ti-55 and Ti-70, are also plotted. If the corrosion properties of Ti-70, with its higher concentration of  $O_2$  and Fe were adequate to permit its use, the allowable thickness could be reduced from 0.046 m for Ti-55 to 0.014 m for Ti-70. A similar comparison could be made for niobium, where the thickness could also be reduced significantly if a higher  $O_2$  content could be tolerated.

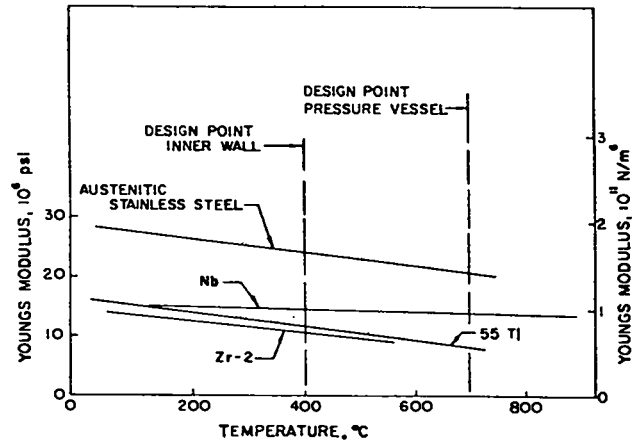


Fig. 25. Modulus of elasticity of prospective wall structural materials.

Any imposed thermal stress will reduce the allowable fatigue stress. As shown in Fig. 27 for a limiting gradient of  $\sim 50$  K, the imposed thermal stress results in only a minor reduction in allowable fatigue properties. Obviously, for a final design, more margin in the form of increased thickness will be required than indicated by the predicted failure points shown in Fig. 26.

The imposed alternating stresses in a niobium or stainless-steel outer wall, shown in Fig. 28, have been calculated from the deflection characteristics in Fig. 23. The allowable stresses are based on the same type analysis as for the inner wall. Imposed stresses for titanium and zirconium, which have relatively low tensile and alternating-stress properties at  $700^\circ\text{C}$ , are not shown. To illustrate the effect of Young's modulus on this imposed stress, moduli of  $Y = 1 \times 10^{11} \text{ N/m}^2$  for stainless steel and of  $Y = 2 \times 10^{11}$  for niobium have been plotted.

The wall deflection of the outer vessel is very small compared with that of the inner vessel. For a 10-cm-thick vessel, stainless steel has a large margin in fatigue strength. Although the corrosion and mass-transfer resistances are better for niobium, additional corrosion allowance is probably not necessary for a stainless-steel pressure vessel, which would be an extremely thick structure. The thermal stress resulting from a 50-K temperature gradient will present no problem.

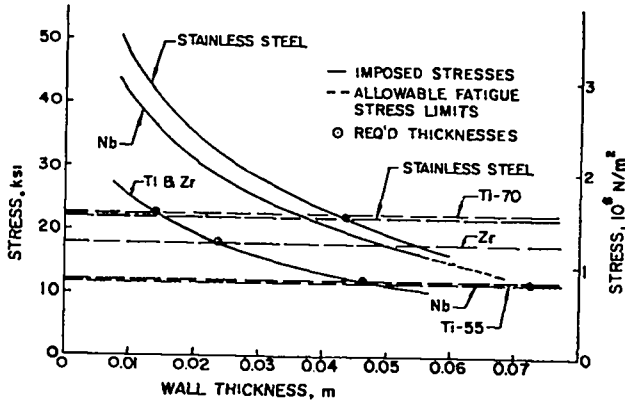


Fig. 26. Imposed stresses in inner wall as a function of thickness for prospective wall materials, based on strains from Fig. 22.

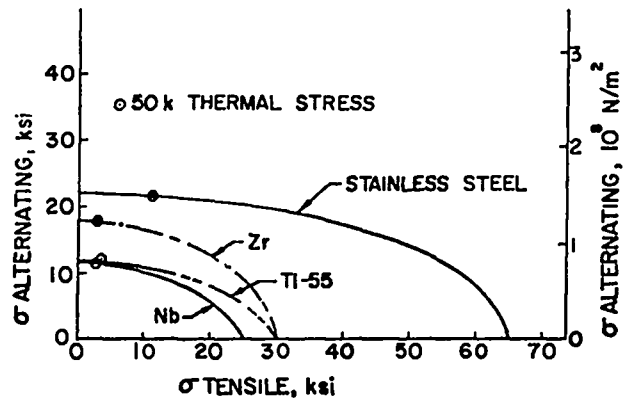


Fig. 27. Reduction in allowable fatigue stresses by imposed stress.

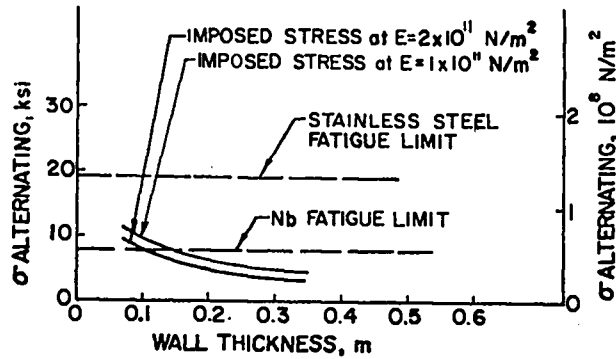


Fig. 28. Imposed stresses in outer wall as a function of thickness for stainless steel and niobium, based on strains from Fig. 23.

### III. AREAS OF UNCERTAINTY

#### A. RADIATION DAMAGE

Neutron damage to the inner walls of the confining vessel could limit the design power level and, more importantly, require replacement of the inner walls during the lifetime of the power plant. Thus neutron damage becomes an important factor affecting both the feasibility and economics of the plant. This damage to an ICTR inner wall is similar to that to the reaction cavity wall of a MCTR, which must endure comparable fluxes of neutrons with similar energy spectra. Moreover, most magnetic systems, which do not have the protective lithium coating of ICTRs on the inner wall, must also endure significant fluxes of charged particles and low-energy photon radiation.

Unfortunately, neutron radiation damage cannot be predicted accurately because the expected fluences are beyond present experience. The average flux of neutrons at the wetted wall is  $\sim 2 \times 10^{15}$  neutrons/s  $\text{cm}^2$  with an energy spectrum as shown in Fig. 29. Fast-fission reactors produce neutron fluxes of comparable magnitude, but only at lower energies ( $< 2.5$  MeV). However, because many important neutron reactions have energy thresholds exceeding 2.5 MeV, extrapolation of data from such fission reactors is inadequate. Cockcroft-Walton accelerators produce the appropriate neutron spectra, but only at fluxes lower by a factor of  $\sim 10^3$ ; therefore experiments equivalent to ten or twenty years of fusion-reactor operation would be clearly impractical. Underground explosions of thermonuclear weapons could provide appropriate fluxes and spectra, but only in short, single pulses, with the result that the total fluence would not be adequate, amounting to only a few minutes of reactor operation. Various experiments are under way to model some aspects of the radiation-damage problem to be encountered in fusion reactors, but all are deficient in either fluence or spectrum. New experiments with appropriate fluxes and energies are proposed,<sup>(10)</sup> but none are under way.

There are two major categories of neutron damage: (1) atomic displacements, i.e., Frenkel-pair production, and (2) nuclear transmutations. The production rates of Frenkel pairs and transmutation products can be estimated: the transmutation production from standard cross-sections;<sup>(11)</sup> and Frenkel-pair production from the elastic and inelastic differential scattering cross-section (coupled with a slowing-down model of the primary, knock-on, displaced atoms,<sup>(12)</sup> as given by Kinchin and Pease<sup>(13)</sup>). As an example, estimated displacement and transmutation production rates for niobium, the common inner-wall material for MCTRs, are shown in Table II. These results were calculated by using the above-cited cross-section data

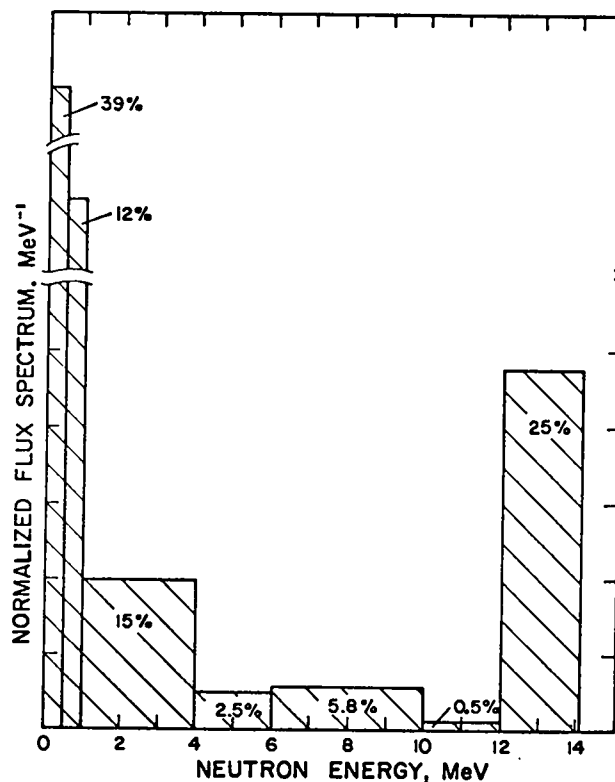


Fig. 29. Neutron spectrum at the ICTR inner wall.

and the spectrum in Fig. 29. The amount of material swelling can also be computed, as done by Martin.<sup>(12)</sup> Unfortunately, the effect of these transmutation and Frenkel-pair production rates or of the swelling on the important structural properties (ductility, yield strength, fatigue strength, and creep rate) cannot be calculated.

TABLE II

DAMAGE REACTION RATES FOR A NIOBIUM INNER WALL

Product	Reactions	Production Rate, %/Year
Frenkel pairs	see text	11.7
Hydrogen	(n,p)	0.037
Helium	(n, $\alpha$ )+(n,n' $\alpha$ )	0.021
Zirconium	(n,2n)+(n,p),(n, $\alpha$ )	0.76
Yttrium	(n,n' $\alpha$ )	0.017

For the stainless-steel inner walls of the suggested ICTR, the theoretical approach outlined above is more difficult than for niobium because of the many constituents in stainless steel, the great number of isotopes for each constituent, the large cross sections for some reactions at thermal energies, and the necessity of including non-linear effects due to isotopic "burn-in" and "burn-out". Because of these difficulties, the calculations of, e.g., helium production, do not agree well with data from fast reactors.<sup>(14)</sup> More importantly, large amounts of data concerning the effects of fast fission fluxes on the structural properties of stainless steel are available,<sup>(14)</sup> but these data do not agree with calculations and must be correlated empirically. In view of the apparent complexity of these damage processes it is difficult to see how such empirical correlations can be extrapolated for a radiation spectrum such as that shown in Fig. 29.

In summary, the neutron-damage effects expected in the ICTR are similar to those to be expected for MCTRs because the fluxes and spectra are similar. For the ICTR the lithium wetting the wall protects the wall from high-velocity particles and low-energy photons, which in magnetic systems interact with the cavity wall. On the other hand, cyclic loading, which occurs in the ICTR walls, does not occur in most magnetic systems. It should be pointed out, however, that radiation damage coupled with cyclic loading may not be necessarily detrimental to the

fatigue strength. It has been suggested that cyclic loading could promote recombination of the Frenkel pairs,<sup>(15)</sup> thus reducing the damage caused by atomic displacement. Because of the general similarity of the present ICTR with other fusion concepts, the results from present radiation-damage research being conducted for the latter should also be applicable to the ICTR.

B. INDUCED ACTIVITY AND AFTERHEAT

Several investigators<sup>(16,17)</sup> have commented upon the smaller levels of radioactivity to be expected in a fusion power plant, compared to the gross fission-product activity in an analogous fission plant. Of perhaps greater significance, from the standpoint of potential inadvertent releases to the plant environs, is the fact that the radioactive products of a fusion plant will generally exist in a more tractable physical form than in a fission reactor, i.e., as induced activity in the structural components of the fusion reactor, rather than as fission products. (A singular exception is the tritium activity in a fusion reactor; however, studies<sup>(17)</sup> indicate that the implied tritium handling problems will not negate the overall relative advantage of a fusion plant.)

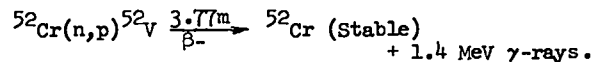
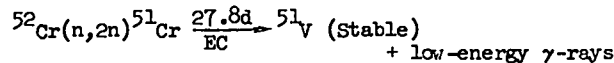
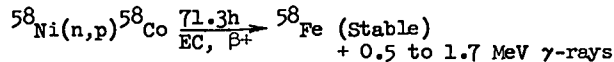
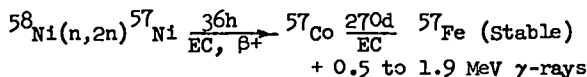
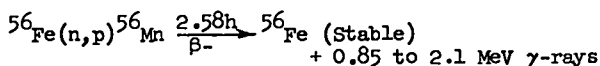
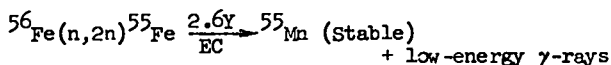
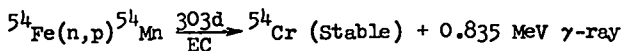
Induced activity and attendant afterheat in fusion-reactor structures will, however, be important factors in the engineering design and in the operation and maintenance of such a plant. Afterheat levels will imply substantial component-cooling requirements for long periods of time after shutdown; and many orders-of-magnitude of ( $\gamma$ -ray) shielding will be needed to allow even limited personnel access to the vicinity of the fusion reactor structural components. This latter point is particularly important if maintenance (or replacement) of structural vessels is required.

Although the absence of fission products is a paramount advantage, the relatively large induced activity in fusion-reactor structures, compared to that in fission reactors, is basic, and derives from two fundamental characteristics of the fusion reactor. First, fusion reactions are neutron-rich; the ratio of excess neutrons produced per megawatt in a (D+T) reactor, to excess neutrons produced per megawatt in a fission reactor is in the range of

~ 2 to 3. More importantly, most fission neutrons do not leave the core, whereas most fusion neutrons will reach at least the inner wall; thus, the effective neutron flux ratios (fusion-to-fission) for structural vessels are typically more like 20 to 80. Secondly, neutrons impinging upon fusion-reactor (blanket) materials will be very fast; perhaps 20 to 40% of these neutrons will have energies of 6 to 14 MeV, as shown in Fig. 29. At these neutron energies a preponderance of particle reactions, e.g., (n,2n), (n,p), can be expected in structural materials, and such reactions generally lead to radioactive daughter products, many of which have long half-lives.

In the present study, the afterheat and the dose-rate levels after shutdown were not estimated accurately. Such estimates have been made by others for typical MCTR systems, (18,19) and the ICTR under discussion should not be very different in these respects. (The main difference is that the present ICTR pressure-vessel material is stainless steel, instead of a refractory metal.) Differences would be expected in magnitudes, but not in the qualitative implications of the results.

Some rough order-of-magnitude values will be estimated to illustrate the activity levels to be expected. Consider a 5-cm-thick inner wall in an ~ 200 MWt ICTR (Fig. 1). The flux of high-energy neutrons (~ 6 to 14 MeV) at this wall will be ~  $7 \times 10^{14}$  neutrons/s cm<sup>2</sup> (plus lower-energy fluxes of ~ 2 to 3 times this magnitude). Using calculated ICTR fluxes, rough estimated reaction cross sections, (11) and appropriate decay data, (20) the possible neutron-induced activities in iron, nickel, and chromium were scanned. The results indicate that the following reactions are of principal importance (for operating times greater than a few months):



Estimated activities (in curies) for these reaction products in the inner wall are shown in Table III, for a shutdown time (t) = 0.

TABLE III

APPROXIMATE RADIOACTIVITY AT SHUTDOWN FOR INNER WALL OF 200-MWt ICTR

Species	Half-Life	Radioactivity After Various Operating Times, 10 <sup>7</sup> Ci				
		30d	180d	1 yr	5 yr	∞
<sup>54</sup> Mn	303d	0.14	0.70	1.2	2.0	2.1
<sup>55</sup> Fe	2.6y	0.49	2.8	5.3	16.6	22.5
<sup>56</sup> Mn	2.58h	10.0	10.0	10.4	10.4	10.4
<sup>57</sup> Co	270d	0.09	0.44	0.73	1.2	1.2
<sup>58</sup> Co	71.3d	0.01	3.1	3.7	3.8	3.8
<sup>51</sup> Cr	27.8d	2.0	3.7	3.7	3.7	3.7
<sup>52</sup> V	3.77m	1.5	1.5	1.5	1.5	1.5
Total		14.2	22.2	26.5	39.2	45.2

For an operating time of one year, one month after shutdown the total activity is ~  $1.1 \times 10^8$  Ci, produced primarily by <sup>55</sup>Fe, <sup>58</sup>Co, and <sup>51</sup>Cr. For long times after shutdown (t > several months), the activity is primarily from <sup>55</sup>Fe, with a half-life of 2.6 years (five years after shutdown, the <sup>55</sup>Fe activity is still ~  $1.4 \times 10^7$  Ci).

The activities in Table III imply rather high and long-lasting afterheat levels and biological dose rates. Table IV shows estimates for these two quantities as functions of time after shutdown. Although these estimates are uncertain to, perhaps, an order of magnitude, they are indicative of the levels to be expected. Clearly, heavy biological shielding would be required for the removal or maintenance of such a component.

TABLE IV  
 APPROXIMATE AFTERHEAT AND DOSE RATE FROM INNER WALL  
 OF A 200-Mwt ICTR  
 (Operating Time, 1 yr)

Nuclear Species	Time After Shutdown							
	0		30 d		1 yr		5 yr	
	After-Heat <sup>a</sup>	Dose Rate <sup>b</sup>	After-Heat	Dose Rate	After-Heat	Dose Rate	After-Heat	Dose Rate
<sup>54</sup> Mn	0.10	0.92	0.09	0.86	0.04	0.40	0	0.014
<sup>55</sup> Fe	0.07	0	0.07	0	0.05	0	0.02	0
<sup>56</sup> Mn	2.28	14.0	0	0	0	0	0	0
<sup>57</sup> Co	0.04	0	0.04	0	0.02	0	0	0
<sup>58</sup> Co	0.50	2.83	0.37	2.11	0.01	0.08	0	0
<sup>51</sup> Cr	0.16	0	0.08	0	0	0	0	0
<sup>52</sup> V	0.36	1.93	0	0	0	0	0	0
Totals	3.5	19.7	0.65	3.0	0.12	0.48	0.02	0.014

<sup>a</sup>Megawatts.

<sup>b</sup>Units of 10<sup>6</sup> rem/h at distance of 1 m.

#### C. REMOVAL OF CONTAMINANTS FROM LITHIUM

Contaminants that must be removed from the ICTR lithium systems may be divided into two groups --noncondensables and condensables. The noncondensables are helium--a (D+T) reaction byproduct (also formed in the lithium); unburned deuterium and tritium from the pellet; and tritium formed from neutron reactions in lithium. The condensables are pellet materials, other than unburned fuel and (D+T)-reaction products, and lithium tritide, which is formed as tritium is produced by neutron reactions.

Another contaminant, not created by nuclear reaction, that must be removed, is oxygen. As in most alkali-metal systems, the oxygen content must be maintained at a very low level. Methods of oxygen removal are discussed elsewhere, (21,22) and are beyond the scope of this report.

Of these contaminants, tritium and lithium tritide formed in the blanket are the only ones that appear to pose a removal problem. The condensable pellet materials will solidify and can be collected in the lithium pool of the spray condenser, where they can be removed by filtration. Helium will collect as a gas and can be removed from the spray condenser through a vacuum pumping system (a vacuum system will probably be needed

anyway to maintain the necessary low condenser pressure). Unburned fuel and lithium compounds in the cavity can probably be confined to the condenser system. Excess deuterium and tritium gases can be pumped out by the vacuum system; and lithium compounds can be crystallized in a cold trap operating at slightly above the lithium melting point, e.g., at 200°C, and located in a side-stream from the atomized-spray recirculation loop of the condenser system.

There are two reasons for maintaining a low tritium inventory in the blanket system: (1) minimization of the radiological hazard from tritium (due to normal leakage or accidental release) and (2) prevention of lithium tritide crystallization in the cool portions of the system, e.g., in the cold end of the intermediate heat exchanger. A removal problem arises because lithium tritide remains in solution with metallic lithium at a concentration which is a function of temperature. This concentration varies from ~ 1 mole % at 1000°C to 0.01-to-0.4 mole % at 200°C. (23) (The wide range of uncertainty at 200°C is due to uncertainties in extrapolating data from 400°C.) If the 750°C stream entering the heat exchanger has an equilibrium LiT concentration, solid LiT will be crystallized and deposited in the heat exchanger as the stream is cooled during transit. Therefore, if LiT

crystallization in the heat exchanger is to be prevented,\* the LiT concentration in the inlet stream (750°C for the present ICTR) must be reduced to, or below, the equilibrium LiT concentration of the outlet stream (400°C for the present ICTR).

A method for tritium removal at high temperature, which would be applicable for the present concept, has been studied and proposed for other fusion power plants.<sup>(24)</sup> This method takes advantage of the high permeability of some metals (notably niobium-1% zirconium) to hydrogen diffusion.<sup>(25)</sup> In this approach the tritium concentration, and thereby the LiT concentration, in the high-temperature lithium stream would be reduced by diverting a side-stream to a system containing thin "windows" of a metal through which the tritium will readily diffuse.

However, the tendency of hydrogen (or tritium) to readily diffuse through metals poses a problem in the present concept--that of tritium leakage through the outer containment wall because permissible tritium leakage rates to the atmosphere are very low (see Section II.D). Based on the permeability of hydrogen through stainless steel<sup>(25)</sup> (which is  $\sim 10^{-2}$  times that through niobium), the tritium diffusion through the 2.5-cm-thick outer wall will be excessive, posing a radiobiological hazard as well as inflicting an economic penalty. This leakage therefore must be reduced. One possibility consists in cladding the outer vessel wall with a material, e.g., tungsten, that has a low permeability for tritium diffusion. Another possibility would be to enclose the entire ICTR in another vessel, maintained at a low temperature, and then to evacuate the volume between this vessel and the outer wall. If the latter scheme is used, the reduction of tritium concentration in the blanket could be enhanced by placing niobium "windows" in the outer wall of the ICTR as shown in Fig. 1.

The removal of LiT in a side-stream cold trap of the condenser recirculation loop will probably be sufficient to maintain the LiT concentration in the

\*Actually, crystallization in the heat exchanger may be only a minor problem if one is willing to accept the economic penalty of using an extra heat exchanger--designed to transfer the full heating load--so that one heat exchanger may be taken "off line" for "regeneration" by heating it to vaporize or dissolve the crystallized LiT.

400°C return stream below the equilibrium solubility concentration. If this is not sufficient, another side-stream cold trap, located in the main 400°C return stream, may be necessary.

In summary, the following considerations will be applicable for the design of a contaminant removal system for the present ICTR concept:

- Condensable materials from the pellet, and LiT formed in the cavity, can be removed by filtration in a side-stream cold trap, operating at  $\sim 200^\circ\text{C}$ , of the condenser recirculation loop.

- Noncondensable materials (helium and unburned fuel) in the cavity can be removed through a vacuum pumping system.

- Tritium leakage through the outer wall at 750°C will probably be excessive. This leakage must be prevented or some means of collecting the leakage must be provided.

- The steady-state LiT concentration within the blanket system should be kept as low as possible--preferably at less than the equilibrium solubility concentration at the lowest system temperature (400°C). Either of two removal methods can probably effect this low LiT concentration--tritium diffusion through a metal (e.g., niobium) membrane at high temperature, and LiT crystallization and removal by filtration at low temperature.

Currently, data are needed to predict these phenomena accurately. These data include equilibrium solubility constants of LiT in lithium, equilibrium dissociation constants for  $2 \text{ LiT} \rightleftharpoons 2 \text{ Li} + \text{T}_2$ , and permeation constants of tritium in various metals. Because appropriate tritium data are unavailable, preliminary design studies<sup>(24,26)</sup> have been based primarily on the extrapolation of LiH and hydrogen data. Although the extrapolations are based on known physical principles, the possible errors are currently too large to undertake detailed design of processing equipment.

#### D. SAFETY FEATURES OF AN ICTR PLANT

In discussing the safety of fusion-powered plants, we are especially concerned with "nuclear safety"--most importantly, with the protection of the public from radiation hazards.

The hazards of handling molten lithium are discussed elsewhere<sup>(21,22)</sup> and are beyond the scope of this report.

As in a fission-powered plant, there are nuclear reactions within the fusion-powered plant; therefore, radiological hazards are attendant. Beyond this fact it is difficult (and often futile) to draw analogies between fission and fusion hazards. As pointed out in Section III.B, claims have been made that fusion plants will be "orders-of-magnitude" safer than fission plants, based on the comparison of fission-product activity to the estimated activity of tritium and of the activated structures in a fusion plant. This comparison is not very useful simply because levels of activities per se are essentially meaningless in terms of radiobiological hazards. The fact remains that the operation of fission plants has been proven safe through many years of technological development and operating experience, whereas the real hazards of a fusion plant can only be a matter of speculation.

However, an important basic difference exists between the fission and fusion processes--in a fission-power reactor an undesirable power excursion is, in principle, possible because excess reactivity is necessary for continued operation; in a fusion-power reactor a power excursion is impossible. Even in this context, however, one must be careful in making comparisons. Although a power excursion is possible in a fission-power reactor, it cannot credibly lead to an explosive energy release because of the way in which these reactors are designed--they simply shut themselves down before such a disaster can occur. Still, in a fusion reactor, whether it is an ICTR or a MCTR, the rate of energy release is proportional only to the amount of fuel confined within the (D+T)-burning region, and both the amount of fuel and the burning-region conditions must be optimal for the process to occur at all. Deviations from the optima, e.g., increases in the amount of fuel or in the energy in the confinement system, will result in decreasing power production.

There will be two known radiological hazards which may present particular problems in a (D+T) "breeder" plant, i.e., the accumulation of tritium and the activation of reactor structures. Tritium is a radiobiological hazard only if ingested (tri-

tium emits only a low-energy beta particle), and therefore poses no hazard if contained within a leak-tight envelope. The problem, however, is in adequately containing gaseous tritium, as discussed in the previous section. In particular, tritium leakage from the primary lithium blanket system must be sufficiently low so that tritium concentrations within and outside the plant area are less than prescribed limits (the allowable tritium concentration at a boundary to the public<sup>(27)</sup> is  $2 \times 10^{-7}$   $\mu\text{Ci}/\text{cm}^3$  or  $2 \times 10^{-17}$   $\text{g}/\text{cm}^3$ ). For example, in an operating plant with this boundary at a radius of 100 m the allowable tritium leakage rate from the plant is of the order of  $10^{-9}$  to  $10^{-10}$   $\text{cm}^3$  (STP)/s if the transport of tritium to this boundary from the plant is by diffusion through air. This low allowable leakage rate imposes an extremely stringent requirement for tritium containment, especially when considering the propensity of tritium to diffuse through metals.

One requirement that will probably be imposed on fusion plants is protection against accidental tritium release from a breach in a pressurized tritium containment system. This is analogous to the required protection in lieu of the classical Maximum Credible Accident (MCA) in the regulatory criteria for fission plants. This MCA has been traditionally assumed not to be obviated by any assurances of structural integrity of the primary containment system, and the imposition of protection against this event will probably be carried over into regulations for the design of fusion plants. This probably means that a secondary containment system will be required to completely enclose any pressurized system containing lithium (bearing tritium) or gaseous tritium.

The other known radiological hazard--that of activated structural materials--will be an operational problem, not a radiation-protection problem. Radiation protection from these activated materials is tractable because they are solid and immobile, and the radiation can be attenuated by simply shielding the activated material. However, the very high biological dose rates from these structures, as indicated in Section III.B, preclude the access of personnel for contact maintenance or replacement of the blanket structure within any reasonable length of time after shutdown.

## E. ECONOMICS

The current competitive criterion for commercial electrical power generation is the total production cost, usually broken down into operating cost and capital cost. The major portion of the operating cost for conventional power plants is the fuel cost, and this is expected to be the case for the ICTR concept. (A discussion of ICTR fuel cost is included in Volume II of this report.) It is assumed that the ICTR fuel cost will be equivalent to the estimated fraction of total production cost (~ 30%) of fast-breeder power-plant concepts. Thus, it is assumed that the capital cost will be ~ 70% of the total production cost for the ICTR.

Because engineering design criteria for the ICTR concept have not been established, it is impossible to estimate detailed capital costs. However, certain portions of the plant and associated costs will be essentially identical to those in advanced nuclear fission-plant concepts, e.g., the HTR (High-Temperature Gas-Cooled Reactor) and the fast breeder reactor. Included in these costs are the direct and indirect construction and depreciable capital costs of the structures and improvements, the steam-plant equipment, and the electrical-plant equipment. For advanced fission-powered concepts, such costs are ~ 60% of the total capital costs, including the secondary containment structure for the reactor system.<sup>(28)</sup> The remaining 40% include the reactor plant equipment and the nuclear-engineering costs. For the (conceptual) MCTR plants, these costs are not well known. (The promoters of the MCTR concepts have the same problem as the advocates of the ICTR concept: detailed cost estimating is impossible unless the plant has been engineered.) In general, however, among the crude estimates that have been made, the reactor plant equipment and nuclear engineering costs for MCTR concepts are slightly higher than those for the HTR and breeder plants.

In comparing fusion-plant reactor equipment and nuclear engineering costs to those of advanced fission-powered plants, the following qualitative statements can be made.

- The mechanical design of fusion reactors is basically simpler than that of fission systems.

Therefore the cost of the fusion reactor and its internal components should be less than that of the fission reactor.

- Nuclear safety systems to prevent supercritical accidents and engineering safeguards to ensure primary containment of fission products are a significant fraction of the cost of fission reactors. Supercriticality simply is not a consideration in fusion reactors. Further, although containment of tritium is a major concern in a fusion reactor, such containment should not be as expensive as the safeguards for containment of much more hazardous fission products.

- The cost of lithium-processing facilities for contamination cleanup in fusion plants is likely to be comparable to that of the sodium-processing facilities in sodium-cooled breeder plants. Possibly, the cost of the tritium removal system in a fusion plant will raise the total chemical-plant cost above that for a sodium-cooled breeder plant. However, it is not likely that this higher chemical-processing cost will offset the cost gains from the first two cost advantages.

In comparing ICTR and MCTR reactor-equipment costs, the major difference is in the equipment for plasma containment, i.e., laser equipment for the ICTR and magnet equipment for the MCTR. If a cost comparison is based on power requirements, the laser equipment will be significantly less expensive than the magnet equipment.

Although a detailed cost estimate of an ICTR can not be made, a significant portion of the total production cost (~ 40%) should be the same as current capital costs of advanced fission electrical-generating plants. Qualitative evaluation of the remaining 60% of the production cost indicates that the ICTR could be economically competitive with other advanced concepts for electrical power generation.

## F. OTHER MEANS OF ENERGY CONVERSION

### 1. General Considerations

Throughout the technological development of the power-conversion industry, which has been based on the heat-engine cycle, a major goal has been to decrease the fuel cost by increasing the efficiency

of converting thermal energy to electrical energy. Thermodynamically, the conversion efficiency is directly affected by the maximum temperature in the process, i.e., the higher the temperature, the higher the conversion efficiency. Heretofore, this maximum temperature has been limited because of physical and chemical properties of the materials (usually for containment) in contact with the thermodynamic "working fluid".

In addition to decreasing fuel cost, there has been an impetus in the past few years to decrease the amount of heat rejected by increasing the conversion efficiency. With the advent of large power plants (1000 MWe or larger) rejecting their waste-heat to natural water sources, the problem arises of altering the ecology of these sources by increasing the water temperature (thermal pollution). The amount of waste heat can be significantly decreased by increasing the conversion efficiency: because the waste heat is proportional to  $1/\eta_0 - 1$ , where  $\eta_0$  is efficiency, an increase in efficiency from 40 to 48% (a factor of 1.2) results in a decrease in the amount of waste heat by a factor of 1.38. However, increases in conversion efficiency entail higher capital cost, as is discussed later; and, in response to public pressure, power-plant designers have discovered that the production cost of existing plants modified at increased cost to reject heat to the atmosphere (even at the expense of decreased conversion efficiency) is less than the cost for a new plant designed for higher conversion efficiency using more expensive materials. Fraas<sup>(29)</sup> has suggested that waste-heat from fusion power plants could be used for building heating and air-conditioning because such plants could be located within urban complexes, thus eliminating the thermal-pollution problem.

The limitation on maximum temperature due to material properties has applied not only to heat-engine cycles but also to various direct-conversion schemes that are based on energy extraction directly from charged particles (e.g., ions). Because ionization of most materials is negligible below  $\sim 2000^\circ\text{C}$  and the maximum working temperature for containing materials that are economically attractive is below  $\sim 1000^\circ\text{C}$ , none of these direct-conversion schemes have been seriously considered as a basis for the electrical-power industry.

Proponents of fusion power have claimed that the prospect of fusion reactors operating at extremely high reaction temperatures (in the keV range) and, particularly, MCFR systems where the hot plasma does not come in contact with containing materials, promises high conversion efficiency by means of direct conversion. Unfortunately, fusion-reactor designs, either ICFR or MCFR, are based on the (D+T) reaction, where the major fraction (0.75 to 0.8) of the total energy must be converted to thermal energy in a liquid lithium blanket to produce tritium. Here, again, the maximum lithium temperature is limited to  $\sim 1000^\circ\text{C}$  by the physical and chemical properties of the materials containing the lithium. Therefore, this major fraction (0.75 to 0.8) of the (D+T) energy can only be converted to electricity by means of a more conventional thermodynamic cycle with a heat engine, leaving only the minor fraction (0.2 to 0.25) for direct conversion. Two questions then remain: "How high a conversion ratio is practical with a heat-engine cycle?" and "Is it practical to consider direct conversion of 20 to 25% of the total energy?"

## 2. Heat-Engine Cycles

The maximum steam temperature in modern steam plants is  $\sim 600^\circ\text{C}$ , resulting in conversion efficiencies of 40 to 45%. Gas turbines, used in combined-cycle power plants and for power peaking in large steam plants, are operating with combustion gases at temperatures of  $\sim 800^\circ\text{C}$  and power levels of 50 to 100 MWe; the resulting conversion efficiency is  $\sim 12\%$  higher than that of plants operating only on a steam cycle. Gas turbines are being developed in Europe to operate in closed-Brayton-cycle plants, with helium at maximum temperatures of  $\sim 1000^\circ\text{C}$ , and at power levels up to 500 MWe; the conversion efficiencies of these plants would be greater than 50%.<sup>(30)</sup> Fraas has proposed a combined potassium vapor-steam cycle for fusion power plants.<sup>(17)</sup> The potassium turbine would operate at  $\sim 1000^\circ\text{C}$ , and the conversion efficiencies would be greater than 50%.

There is little doubt that heat engines can be developed to operate at higher temperatures than in modern steam plants, i.e., up to  $1000^\circ\text{C}$  with overall efficiencies approaching 60%. Unfortunately, the materials that must be used in these machines and for associated components (e.g., piping, heat

exchangers) are very expensive, so that the capital cost of such a power system would be simply too high to compete economically, even though the plants would operate at higher efficiencies.

To emphasize this point, consider the following example of a basic economic principle.<sup>(31)</sup> If a proposed plant can operate at an efficiency  $X\%$  higher than that of an existing plant and for a capital cost increase of  $Y\%$  and if the operating costs are the same for both plants, these plants will be competitive (total production costs are equal) when  $Y = X(P)/C$ , where  $C$  is the capital cost and  $P$  is the total production cost (capital cost plus operating cost). If the ratio of capital cost to total production cost remains the same as that for advanced nuclear-powered plants (see preceding section), then the percentage increase in capital cost for a proposed plant to compete with an existing plant is  $Y = X/0.7$ . Therefore, if the proposed plant operates at  $60\%$  efficiency, the increase in capital cost of this plant is limited to  $48\%$  of that of an existing plant operating at  $45\%$  efficiency. Because the cost of currently available raw materials that would permit such a high conversion efficiency is up to ten times that of materials in existing plants, it is questionable whether the capital cost of the highly efficient plant would be economically competitive with that of the existing plant.

### 3. Direct-Conversion Possibilities

Two direct-conversion possibilities exist for a plant based on the present ICER concept: (1) the generation of a counter electromotive force in a magnet system that provides a magnetic field in the cavity by extracting energy from the expanding (ionized) pellet material as it works against the magnetic field; and (2) the exhaustion of the cavity gases (after quasi-equilibration) through a magneto-hydrodynamic (MHD) duct. Here, again, the use of any

direct-conversion method will be based on the economic principle described above. However, because only  $25\%$  of the total energy is available for conversion, a major fraction of this energy must be converted at high efficiency to offset the added expense of magnet systems, energy storage systems, power-conditioning equipment, and associated cooling equipment.

Even if in the first method it were possible to convert a major fraction of the cavity energy at high efficiency, the cost due to the increased complexity of magnetizing the blanket would probably price such a system out of competition with a heat-engine-only conversion system. For example, the conversion efficiency of a fusion plant based on the ICER concept would increase from  $40$  to  $43.75\%$  if  $50\%$  of the energy in the cavity were directly converted at an efficiency of  $90\%$ . Then, to be competitive with steam-plant conversion of the cavity energy, the increase in capital cost of adding the direct-conversion system must be only  $13.4\%$  or less, which would probably be economically unfeasible.

In the second method, the fraction of the cavity energy that can be extracted is very low-- the enthalpy change from  $4000$  to  $2000$  K is only  $20\%$  of the total heat content. Even if the conversion efficiency were  $100\%$ , the increase in capital cost due to adding the MHD system would have to be  $10.7\%$  or less to be competitive with converting all the energy in a steam plant.

In conclusion it may be stated that the cost of magnet systems and associated equipment for direct conversion of  $25\%$  of the total energy would probably be too high to compete economically with heat-engine conversion cycles.

#### IV. CONCLUSIONS

##### A. THE WETTED-WALL ICTR

###### 1. Introduction

The analyses of cavity and blanket phenomena described in Section II do not indicate any unsolvable engineering problems in developing a wetted-wall ICTR. The most significant unknown (see Section III) is the effect of radiation damage on the lifetime of the inner walls. However, it must be remembered that laser-driven fusion is not yet a reality nor even an eventual certainty. Therefore it seems unwise to undertake a large-scale engineering effort to establish a reference reactor design that is based on assumptions about currently unknown phenomena. On the other hand, it is also unwise to ignore recognizable engineering problems in a potentially attractive concept. Such problems can be effectively studied, both analytically and experimentally. Efforts on certain of these problems are under way, but other work needs to be started.

Problems of integrating ICTR systems in a plant and recommendations for extension of other study areas mentioned in this report are discussed in the following paragraphs.

###### 2. Plant Systems Integration

As mentioned in Section III.E, certain portions of an ICTR power plant will be similar to those of current electrical generating plants. These portions, which can be engineered with current technology, are the electrical switchyard, the steam-turbine plant, and the intermediate cooling system. The electrical switchyard includes power-conditioning equipment from the main alternator busses to the high-voltage transmission lines; the steam-turbine plant includes the equipment described in Fig. 3; and the intermediate cooling system includes the piping, pumps, and auxiliaries for circulating the intermediate coolant between the steam generators (Fig. 3) and the intermediate heat exchanger (Fig. 2).

Other portions, which cannot be engineered because of lack of technology, are the ICTR, the chemical processing systems, and the laser and pellet-injection systems. Major engineering problems in the ICTR and in the tritium-processing system have been discussed earlier.

ICTR engineering problems are centered on the survival of the inner wall separating the cavity from the blanket. The largest and most important uncertainty is the effect of radiation damage on wall lifetime--neither erosion from the blast nor fatigue failure from the cyclic strains per se seem to limit the lifetime. If the wall lifetime is only a few years or less, a major problem arises in designing for replacement. If replacement in situ is infeasible, the entire assembly of shells may have to be discarded and replaced. Either method of replacement may impose a major cost penalty.

Another feature that must be provided is shutdown cooling of the afterheat generated in the wall structure. Because the afterheat level is relatively high and the isotopes have half-lives of the order of years, the structure will have to be cooled indefinitely.

The chemical processing systems must remove condensable pellet materials, LiT formed by tritium generated from neutron reactions in lithium, as well as oxygen and other noncondensables (helium and unburned fuel) that accumulate in the lithium systems. The tritium concentration, whether in the form of LiT or gaseous tritium, must be minimized to reduce the radiobiological hazard in case of tritium leakage.

Details of laser engineering problems are discussed in Volume II. Integration problems for the laser system are centered on transporting and focusing the beam (with the aid of mirrors, lenses, etc.) from its source to the point at which it impinges on the pellet.

The design of the pellet-injection system will be a difficult timing, trajectory, and mechanical-engineering problem. The pellet-injection system must be integrated with the laser system so that the laser beam and the pellet arrive simultaneously at the center of the cavity. The geometric tolerances of the focused spot are likely to be small, and the pellet may have to be oriented exactly as desired.

### 3. Extension of Present Work

Most of the analyses presented in Section II should be continued and expanded.

- Because of time (and cost) limitations, the ablation of lithium from the wall (pellet wetted-wall interaction) was calculated by using a very approximate equation-of-state; more sophisticated calculational methods are available. Also, the quasi-equilibration conditions in the cavity were assumed and should be determined more accurately by extending the ablation calculations.

- The calculation for blowdown of the cavity gases through the condenser should be extended. Deceleration of the supersonic liquid-vapor spray at the condenser exit was not calculated; a calculational model could be developed.

- Wall stresses were estimated from the movement of liquid boundaries based on hydrodynamic calculations; a calculational model should be developed to include a more accurate determination of restraining forces.

In addition, experimental studies, some of which are already under way in the Sherwood controlled-fusion program or in other programs, should be conducted in the following areas.

- Properties of Lithium - Thermodynamic and transport (particularly opacity) property data are needed in the temperature range of 0.2 to 20 eV.

- Radiation Damage - The effects of neutrons, with appropriate fluences and spectra, on the structural properties (yield strength, ductility, fatigue strength, and creep rate) of prospective materials must be known.

- Neutron Data - Neutron reaction and  $\gamma$ -ray production data are needed for lithium and pertinent structural materials especially at neutron energies  $> \sim 5$  MeV.

- Corrosion and Mass Transport - Compatibility studies should be extended to measure mass transport, intergranular attack, etc., of structural materials by lithium in dynamic systems at appropriate temperatures.

- Tritium Removal - Solubility constants for LiT and tritium in lithium and permeation constants for tritium through various metals are needed. Chemical-engineering laboratory and pilot-plant scale studies of tritium recovery methods should be initiated.

- System Studies - These studies include experimental evaluation (engineering similitude) of lithium layer formation on the wetted wall, and condensation of superheated lithium vapor in a supersonic spray duct.

The activities outlined above can be conducted simultaneously with efforts to attain successful laser-driven fusion. Most of the experimental work is also applicable to magnetically confined concepts.

When (and if) laser-driven fusion becomes a reality, a program to develop a demonstration ICTR should be initiated. This program would include, as a major goal, a full-scale test of a laser-initiated pellet in a cavity surrounded by a vessel containing lithium.

## B. COMPARISON OF ICTR WITH MCTRS

### 1. Introduction

A comparison between the present laser-driven fusion concept and some familiar magnetic plasma-confinement concepts reveals interesting similarities and differences. Most similarities stem from the common fuel (D+T); whereas most of the contrasts are due to the difference in proposed confinement method, either magnetic or inertial. While the elucidation of these contrasts is informative, some caution is in order. As previously mentioned, no fusion concept is yet a working reality; therefore, it is inappropriate (and harmful to the overall development of controlled fusion) to treat these comparisons as advantages or disadvantages as if there was a choice between one concept or another.

Because these concepts burn (D+T) they must utilize the energy of neutrons generated by the

fusion process--75 to 80% of the total (D+T) energy-- which escape the reaction volume, and they must breed tritium from these neutrons to replace the consumed fuel. These facts require a breeding blanket, largely composed of lithium, that surrounds the reaction volume. In addition to removing the heat generated by dissipation of the neutron energy, the lithium must be processed to remove the tritium. In the wetted-wall concept, the lithium will be comparatively easy to flow for heat transfer and tritium removal because there is no magnetic field in the blanket. This will eliminate any need for gas cooling or for small insulated tubing, as sometimes discussed in magnetic fusion systems.

## 2. Inner Wall

Because the energy output is proportional to the neutron output, structural materials of fusion systems will be damaged by the neutron flux. In the present concept of an ICTR the cavity may be sized to control the damage, as is discussed later. The only damaging particles that will penetrate to the wetted wall will be neutrons; the wall surface is protected from erosion by low-energy photon radiation and by impact of high-velocity particles. The wetted wall need not have particular electrical properties and the cavity does not have to be highly evacuated, with the result that the cavity volume does not have to be defined by a sealed vessel. Thus, for the present concept, greater latitude is allowed in the choice of both wall material and method of fabrication. However, because the wetted wall sustains significant strain under each cycle, its material will have to have a fatigue strength not required in most, but not all, magnetic fusion concepts.

## 3. Confinement System

For magnetically confined concepts, the plasma pressure will be specified by attainable magnetic pressures and by the yield strength of materials. The plasma density is then specified by the minimum ignition temperature ( $\sim 5$  keV) and by the requirement of useful return on invested energy ( $n\tau$ ). Together, these parameters imply a minimum plasma scale length, thereby inferring a corresponding reactor size. In the case of the ICTR, the dimensions of the confining vessel remain free parameters,

independent of confinement and ignition problems; therefore, the dimensions may be chosen to suit radiation-damage levels or other criteria.

Another feature of magnetic confinement is the requirement for large amounts of stored energy in the magnet system:  $4 \times 10^{10}$  J for a Tokamak reactor magnet<sup>(32)</sup> or  $5 \times 10^9$  J for a theta-pinch reactor.<sup>(33)</sup> A corresponding feature in the present system might be power supply to the laser, but this supply will be much lower and the power source can be located away from the reactor vessel. Thus, the possibility of a stored-energy accident involving the reactor does not exist for an ICTR. A further consequence of separating the power source from the reactor will be the relatively easier protection from neutrons leaking through the lithium blanket.

## 4. Power Level

System studies of MCFRs generally dictate that units should be large, resulting in plants generating 2000 to 5000 MWe, to be economically feasible. Upon failure of such units, large transients would be introduced into power networks, making load adjustment difficult, perhaps requiring large energy storage systems. Failure of the cooling system for superconducting magnets would be very serious, not only because of a potential energy storage accident, but also because of the long time (60 days for a Tokamak reactor<sup>(32)</sup>) required to cool the superconducting magnet down prior to its operation.

In contrast, ICFRs need not be large--the present design assumes a thermal-energy output of 200 MW. They could be either scaled up to larger sizes or could be clustered, and probably would be served by a single laser system. Individual units could be shut down or restarted without special difficulty, and the pulse rates could be changed as needed to supply a varying load. This flexibility also has an important bearing on the radiation-damage problem: individual units could be shut down for replacement of parts without completely interrupting power generation.

## 5. Ecological Effects

Discussion of the ecological impact of fusion reactors has centered upon the relatively waste-free fuel cycle (compared to fission reactors), on

the possible hazards involved, and on the possibility of burning wastes (particularly the long-lived fission products  $^{85}\text{Kr}$ ,  $^{90}\text{Sr}$ , and  $^{137}\text{Cs}$ ). Most of the general discussion of fusion also applies to the ICTR system. The fuel cycle is the same, resulting in the same waste products; and the breeding is the same, presenting the same hazard of accidental tritium release. With regard to burning wastes, the possibility of burning fission products or other wastes is much greater in the ICTR because, unlike magnetic systems, no ultrahigh vacuum is required.

### C. COMPARISON OF WORLD ENERGY RESOURCES

Up to the present, economics has been the sole consideration in determining fuel usage and methods of energy conversion, i.e., the quest for ever-decreasing electrical power production cost overrode all other considerations. However, during the past few years, the public has become aware of a host of socioecological problems, some the result of advancing technology, but most the result of the ever-expanding population; these problems will no doubt affect any future fuel usage and energy conversion considerations, but economics will probably remain the most important factor.

The known and (estimated) undiscovered reserves of the world's supply of fossil, fissile, and fusion fuels, as of 1968<sup>(34)</sup> are shown in Table V. In many treatises on the effects of an expanding population it is reasoned that the world's population will reach an asymptotic value of  $\sim 10^{10}$  within the next 100 years. If the U.S. per-capita energy consumption rate of 1970 is applied to this asymptotic total population, the world's total energy-consumption rate will be 2.8 Q per annum<sup>(35)</sup> ( $Q = 10^{18}$  Btu =  $1.06 \times 10^{21}$  J). At this consumption rate the supplies in Table V, would last for the durations shown in Table VI.

These results clearly indicate the relative shortage of fossil and rich-ore fissile fuels. In the past decade, the shortage in fossil fuels has been reflected in a changeover to power plants burning fissile fuels in areas where fossil-fuel costs are high. This change has not occurred because nuclear power, per se, is preferable, but simply because this form of energy production has become economically competitive. However, fissile

TABLE V  
WORLD ENERGY RESOURCES

Energy Source	Energy Available, $Q^a$	
	Known	Undiscovered (Estimated)
<u>Fossil</u>		
Coal	19	270
Oil and natural gas	5.1	90
<u>Fissile</u>		
Burners (1.5% eff)		
Rich ore (< 20¢/kg)	7.5	20
Low-grade ore (> 20¢/kg)	2.8(10) <sup>4</sup>	8(10) <sup>4</sup>
Breeder (60% eff)		
Rich ore (< 20¢/kg)	300	950
Low-grade ore (> 20¢/kg)	9.5(10) <sup>5</sup>	3(10) <sup>6</sup>
<u>Fusion (50% eff)</u>		
Deuterium	4(10) <sup>9</sup>	4(10) <sup>9</sup>
Lithium	3(10) <sup>6</sup>	3(10) <sup>6</sup>

<sup>a</sup> $Q = 10^{18}$  Btu =  $1.06 \times 10^{21}$  J

TABLE VI  
WORLD ENERGY RESERVES

Energy Source	Years at 2.8 Q per Annum <sup>a</sup>	
	Known	Possible
<u>Fossil</u>		
Coal	6.8	96
Oil and natural gas	1.8	32
Total	8.6	128
<u>Fissile</u>		
Rich-ore burners	2.7	7.1
Low-grade ore burners	1.0(10) <sup>4</sup>	3(10) <sup>4</sup>
Rich-ore breeders	107	340
Low-grade ore breeders	3.4(10) <sup>5</sup>	(10) <sup>6</sup>
Total rich ore	110	347
Total low-grade ore	3.5(10) <sup>5</sup>	(10) <sup>6</sup>
<u>Fusion</u>		
Deuterium	(10) <sup>9</sup>	(10) <sup>9</sup>
Lithium	(10) <sup>6</sup>	(10) <sup>6</sup>

<sup>a</sup> $Q = 10^{18}$  Btu =  $1.06 \times 10^{21}$  J

fuel costs will increase as the rich-ore reserves are depleted; and, unless new mining and ore-processing techniques are developed, fissile-fuel-burning plants will become economically unattractive and other forms of energy will be sought. At present, it is established national policy that the fast-breeder reactor (in which low-grade fissile fuel,  $^{238}\text{U}$ , is converted to fissionable  $^{239}\text{Pu}$  while producing power) will replace the fissile-fuel-burning plants as rich-ore deposits are depleted. Although the supply of low-grade ore is vast, there remains the question whether a fast-breeder-based power industry is desirable or even feasible.<sup>(36)</sup> The problem of large-scale fission-product waste disposal, alone, could make a fission-power economy very expensive.

If our fuel sources are in fact restricted as indicated in Table V, nuclear power (either fission or fusion) must be used for the world's future needs. Electric-power generation by controlled fusion processes is, of course, not a certainty; but from the foregoing discussions there is little doubt that, if made to work, fusion power could have vast economic, technical, and socioecological advantages over fast-fission breeders.

In conclusion, it should be evident that the quest for a workable fusion power system is more than the satisfaction of a scientific curiosity; it may be essential to the future well-being of mankind.

## APPENDIX A

### SOME NEUTRONICS FEATURES OF AN ICTR

by C. W. Watson

#### 1. Introduction

Nuclear radiation-transport considerations will be of central concern in the design and operation of any controlled thermonuclear reactor (CTR) for electrical power generation. Generally, these considerations fall into one or more of five areas (listed below in order of decreasing importance in determining the engineering feasibility of a CTR design):

- Energy-deposition rates and spatial distributions in the reactor complex.
- Tritium production rate.
- Radiation-damage effects.
- Tritium processing and handling (safety).
- Safety and reliability problems arising from the buildup of induced activities and associated afterheat in the plant components.

The first two categories, in particular, are of fundamental importance in the initial conceptual design of any CTR.

For the present study of inertially-confined thermonuclear reactors (ICTRs), neutron and  $\gamma$ -ray transport calculations were required to define specific reactor systems and to provide numerical results for concomitant design studies. The first two categories--energy deposition and tritium production--are treated in this Appendix.

#### 2. Basic ICTR Configuration

A rather specific overall concept has dominated the ICTR studies to date. The basic configuration consists of an evacuated spherical cavity in which (D+T)-burning pellets are exploded. This cavity is surrounded by a thin ablative layer of liquid lithium on the inner surface of a metallic inner wall (which surrounds the central vacuum and maintains

the cavity), followed by a liquid-lithium blanket. The blanket functions as a tritium-breeding region, as a (D+T) neutron-energy absorber, and as the heat-transfer medium for removing the deposited energy. This lithium blanket and the pellet blast energy are contained by an outer, relatively thick, metallic pressure vessel. Both the inner and the outer metallic walls are cooled by the lithium as necessary. A schematic representation of the system is shown in Fig. A.1.

In a more realistic design a small blowdown nozzle (half-angle,  $\sim 6^\circ$ ) would be added, as shown, for removing cavity debris after each shot. The nozzle would occupy only  $\sim 1\%$  of the total blanket volume, and would decrease the tritium production and energy deposition in the blanket by no more than a few percent. Consequently, the nozzle was not included in the neutronics studies.

#### 3. Pellet Source

Nuclear characteristics of the pellets are discussed in Vol. II of this report. Each (D+T) reaction is assumed to produce 3.52 MeV of  $\alpha$ -particle energy, deposited locally in the pellet, and one 14.1-MeV neutron. This neutron produces secondary  $\gamma$ -rays and also deposits some of its energy directly in the pellet. Leakage from the pellet consists of a high-intensity 14.1-MeV neutron component, a lower-energy (degraded) neutron component, and secondary  $\gamma$ -rays. Because the pellets are small, self-absorption in the pellets is also relatively small (but not negligible); for convenience, the blanket heating calculations assumed the pellet to be a massless, isotropic-point monoenergetic (14.1 MeV) neutron source, emitting 8 MeV of neutrons per (D+T) reaction, accompanied by  $\gamma$  MeV of secondary  $\gamma$ -rays. The source intensities,  $\theta$  and  $\gamma$ , were inferred from appropriate pellet neutronics studies.

#### 4. Tritium Production

In the ICTR concept there is no magnetic field penetrating the blanket region, in contrast to a magnetically-confined system (MCTR), giving a fundamental breeding advantage to the ICTR. The absence of magnetic fields means that the blanket lithium can be efficiently pumped out of the blanket directly to external heat exchangers, obviating the need for special heat-transfer structures (and media) within the blanket; any such structure would normally reduce the tritium-producing potential in the blanket.

Another tritium-breeding advantage is inherent in the concept of Fig. A.1. The principal mechanism by which blanket structures reduce the tritium production is through degradation of the fast-neutron spectrum via inelastic-scattering reactions, particularly in the inner portion of the blanket; this reduces the vital  ${}^7\text{Li}(n, n'\alpha)\text{T}$  reaction rate. This degradation would be relatively small in the geometry of Fig. A.1 because most of the structural material is located in the pressure vessel away from the inner part of the lithium blanket.

Because adequate tritium breeding in an ICTR would probably be relatively easy to accomplish and because there are no compelling reasons for keeping the blanket thickness small (in contrast to the MCTR, where thinner blankets mean smaller magnets), it seems reasonable to assume that no tritium-enhancing or blanket-thickness-reducing additives would be required in the ICTR. (Note also that good neutron-removal properties for shielding are not necessary

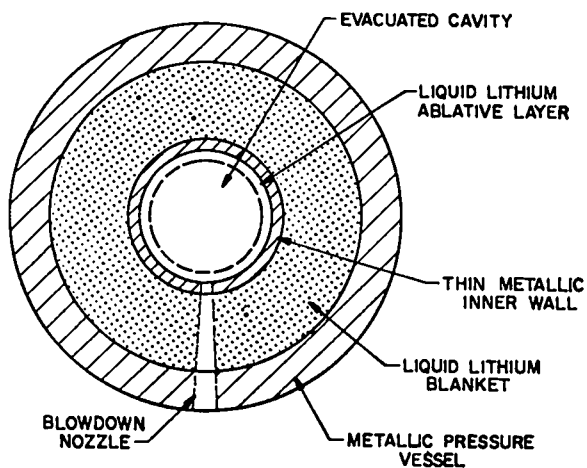


Fig. A.1. ICTR schematic.

in the ICTR blanket.) Thus, for the present work, a blanket of molten natural lithium was assumed, with no internal structure. Adequate internal support could be provided by the blowdown nozzle mentioned earlier.

Tritium production calculations were performed with the MCH Monte Carlo code, which is similar to the MCN code<sup>(37)</sup>, but includes tallies of tritium-producing reactions for lithium. Both  ${}^6\text{Li}(n, \alpha)\text{T}$  (or  $T_6$ ) and  ${}^7\text{Li}(n, n'\alpha)\text{T}$  (or  $T_7$ ) reactions are tallied per source neutron. Total tritium production is  $T = T_6 + T_7$ .

The basic calculational model is shown in Fig. A.2. Here, an outer wall is included for two reasons: (1) a plenum is required to collect lithium flow from the inner blanket, and (2) the location of the main pressure vessel, determined primarily by hydrodynamic response considerations, may not be compatible with the overall lithium thickness needed to remove most of the available neutron energy.

Tritium production studies were made by varying the dimensions and the materials in this basic configuration. Running time for each of these problems, for relative errors of  $< 5\%$ , was  $\sim 5$  min on the CDC-7600 computer.

Figure A.3 shows tritium production vs position of a 2.54-cm-thick iron main pressure vessel in a 100-cm-thick lithium blanket (total thickness of lithium). These calculations were made for an ICTR having a fusion pellet at the center of a cavity of 100-cm radius, with a 0.5-cm-thick niobium

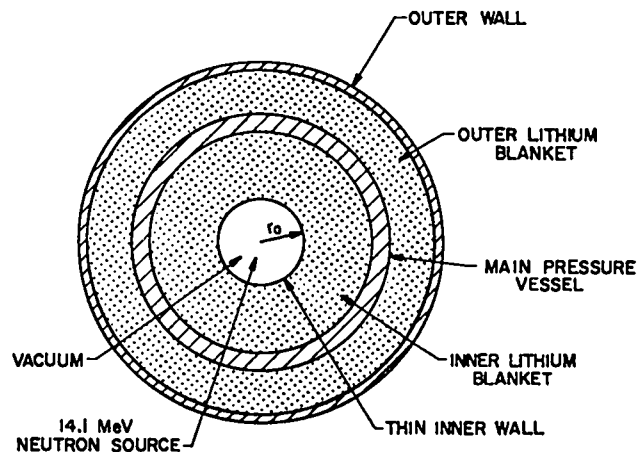


Fig. A.2. Basic ICTR configuration.

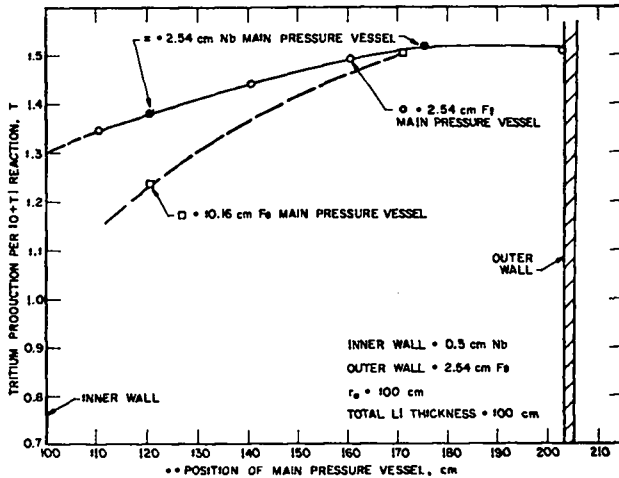


Fig. A.3. Tritium production ( $T$ ) per  $(D+T)$  reaction for configuration of Fig. A.2.

inner wall and a 2.54-cm-thick iron outer wall. Two calculations for a 2.54-cm-thick niobium main pressure vessel are also plotted; these results are almost identical to those for the iron vessel. Finally, two points are shown for a 10.16-cm-thick iron main pressure vessel.

Note that the effect of the main pressure vessel upon tritium production is small if the vessel is located at  $\sim 70$  cm or more into the lithium. Also, the reduction from the maximum value ( $T \approx 1.51$ ) produced by locating a 10.16-cm-thick vessel at 20 cm into the lithium is very nearly twice that produced by a 2.54-cm-thick vessel at that location, i.e., the tritium production is reduced approximately inversely as the square root of the vessel thickness.

This variation is consistent with a calculated breeding-ratio reduction produced by adding a relatively thick ( $\sim 5$  cm) inner structural wall for restraint of inward motion of the inner wall (see Section II.C.3 of main body of report). A calculation using the configuration of Fig. A.2 with a 5.08-cm-thick iron inner wall indicated that  $T \approx 1.23$ , which is not a prohibitive reduction in the breeding ratio.

Additional tritium estimates for a more specific ICTR design will be presented later.

## 5. Heating Estimates for a 200-MWt ICTR

Hydrodynamic calculations indicate that a 10-cm-thick main pressure vessel at 70 cm into the lithium blanket of Fig. A.3 ( $r = 170$  cm) would be adequate to contain a pellet explosion with a (total) energy release of  $\sim 200$  MJ. From these results, combined with cavity blow-off calculations, blanket heat-transfer calculations based upon initial heating estimates, and tritium production estimates, preliminary geometry specifications were defined for a 200-MWt ICTR (one 200-MJ pellet per second). The resulting configuration is that of Fig. A.2, with detailed (one-dimensional, spherical) specifications as given in Table A-I. Total lithium in this system is  $1.47 \times 10^4$  kg.

Neutron heating estimates were based upon Monte Carlo calculations, using codes that were modifications of the LASL point-cross-section general-geometry Monte Carlo neutron code, MCN.<sup>(37)</sup> In these codes, several optional tallies of value to energy deposition estimates were incorporated.

- $\phi_{ij}$  = neutron flux in energy interval  $\Delta E_j$  at surface  $i$ ,
- $J_{ij}$  = neutron currents (+ and -) in energy group  $\Delta E_j$  across surface  $i$ ,
- $\Delta E_{el}$  = energy deposited in each spatial cell of the problem via neutron elastic-scattering events,
- $\Delta E_{n,1}$  = neutron energy lost in each cell via  $(n, n'\gamma)$  events in lithium,
- $\Delta E_{non}$  = neutron energy lost in each cell via other nonelastic scattering events,
- $\Delta E_{n, xn}$  = energy lost by neutrons in each spatial cell of the problem via  $(n, 2n)$ ,  $(n, 3n)$ , etc. events,
- $C$  = number of neutrons captured in each spatial cell of the problem.

Total computer running time per problem was  $\sim 20$  min (CDC-7600) for relative errors of 1 to 5%. Two problems were run, one with lithium coolant in the stainless steel (SS) and one without lithium, to separate the heating for the two materials. A tritium production calculation with the MCH code was also run for this geometry; results are shown in Table A-II.

TABLE A-I

CALCULATIONAL MODEL FOR A SPHERICAL 200-MWt ICTR

(One Pellet per Second)

<u>Cell No.</u>	<u>Outer Radius, (r), cm</u>	<u>Material</u>	<u>Density, gm/cm<sup>3</sup></u>	<u>Description</u>
1	98.9	Li	0.0018	Cavity
2	99.0	Li	0.495	Ablative Li on inner wall
3	100.0	Stainless Steel + Li	SS=4.72 Li=0.197	Inner wall, with void fraction = 40%
4	103.25	Li	0.492	1st blanket
5	106.49	Li	0.490	1st blanket
6	110.20	Li	0.488	1st blanket
7	113.91	Li	0.486	1st blanket
8	118.08	Li	0.484	1st blanket
9	123.19	Li	0.482	1st blanket
10	129.22	Li	0.480	1st blanket
11	137.10	Li	0.478	1st blanket
12	147.76	Li	0.476	1st blanket
13	158.43	Li	0.474	1st blanket
14	169.55	Li	0.473	1st blanket
15	172.88	Stainless Steel + Li	SS=7.07 Li=0.047	Pressure vessel, with void fraction = 10%
16	176.21	"	"	"
17	179.55	"	"	"
18	189.55	Li	0.472	2nd blanket
19	199.55	Li	0.472	2nd blanket
20	209.55	Li	0.472	2nd blanket
21	212.09	SS	7.86	Outer shell

TABLE A-II

RESULTS OF MONTE CARLO CALCULATIONS FOR CONFIGURATION OF TABLE A-I  
PER 14.1-MeV SOURCE NEUTRON

Cell	$\Delta E_{el}$ MeV/Neutron	$\Delta E_{n,l}$ MeV/Neutron	$\Delta E_{non}$ MeV/Neutron	$\Delta E_{n,xn}$ MeV/Neutron	Captures/ Neutron	$T_6$	$T_7$
1	0.0020	0.0059	0.0514	0.0111	0.0011	0.0008	0.0049
2	0.0089	0.0023	0.0151	0.0037	0.0008	0.0010	0.0010
3 (Li)	0.0336	0.0081	0.0490	~ 0	0.0041	0.0036	0.0064
3 (SS)	0.0127	--	0.8128	0.2494	0.0098	0	0
4	0.2551	0.0728	0.4846	0.0752	0.0306	0.0276	0.0488
5	0.2460	0.0690	0.4518	0.0697	0.0317	0.0315	0.0516
6	0.2736	0.0761	0.4996	0.0736	0.0365	0.0366	0.0625
7	0.2610	0.0670	0.4610	0.0630	0.0369	0.0348	0.0510
8	0.2752	0.0767	0.4742	0.0662	0.0433	0.0422	0.0553
9	0.3235	0.0860	0.5219	0.0729	0.0540	0.0546	0.0623
10	0.3372	0.0916	0.5301	0.0703	0.0643	0.0625	0.0647
11	0.3881	0.1025	0.5947	0.0700	0.0848	0.0836	0.0738
12	0.4361	0.1157	0.6108	0.0615	0.1190	0.1162	0.0721
13	0.3432	0.0852	0.4549	0.0453	0.1232	0.1211	0.0573
14	0.2869	0.0676	0.3428	0.0327	0.1371	0.1370	0.0468
15 (Li)	0.0059	0.0025	~ 0	~ 0	0.0042	0.0048	0.0010
15 (SS)	0.0245	--	0.5287	0.0745	0.0125	0	0
16 (Li)	0.0037	0.0011	~ 0	~ 0	0.0034	0.0040	0.0004
16 (SS)	0.0184	--	0.3239	0.0392	0.0094	0	0
17 (Li)	0.0024	0.0005	~ 0	~ 0	0.0024	0.0028	0.0001
17 (SS)	0.0130	--	0.1957	0.0202	0.0064	0	0
18	0.0610	0.0127	0.0423	0.0054	0.0512	0.0499	0.0067
19	0.0434	0.0093	0.0378	0.0042	0.0415	0.0417	0.0054
20	0.0307	0.0057	0.0243	0.0023	0.0363	0.0344	0.0031
21	0.0024	--	0.0378	0.0035	0.0015	0	0
Total (Li)	3.618	0.958	5.646	0.727	0.9064	0.891	0.675
Total (SS)	0.071	0	1.899	0.387	0.0396	0	0
Total (Li+SS)	3.689	0.958	7.545	1.114	0.9460	0.891	0.675

With the exception of  $\Delta E_{e1}$ , the terms in Table A-II do not give energy deposition directly; nor do they, because of the implied secondary  $\gamma$ -ray production, generally give the spatial distributions. The variety and complexity of reactions that 14-MeV neutrons undergo in most materials, especially in lithium, make a complete analysis of the blanket energy deposition very difficult, even in principle. In practice, the lack of requisite detail in available physics data makes such an analysis impossible.

It becomes necessary to assess the relative rates of the various reactions and to direct attention only to those that are of primary importance. Such assessments were made for the ICTR, using Monte Carlo tabulated flux spectra. Results for lithium are shown as a function of distance into the blanket in Addendum 1 to this Appendix. Based upon these results, the energy deposited was estimated by assuming the following:

1. All lithium captures are  ${}^6\text{Li}(n,\alpha)\text{T}$  events which deposit  $\sim 4.79$  MeV locally per capture.
2. Energy deposition via SS captures is negligibly small. Thus, all of  $\Delta E_{n,xn}$  for SS is a direct energy loss (no nuclear recoil energy deposited).
3. All of  $\Delta E_{\text{non}}$  for SS reappears as inelastic  $\gamma$ -rays.
4. All of  $\Delta E_{\text{non}}$  for lithium is from  ${}^7\text{Li}(n,n'\alpha)\text{T}$  events.

For  ${}^7\text{Li}(n,n'\alpha)\text{T}$ , we assume 2.47 MeV lost per event, i.e., 2.47 MeV is lost per unit  $\text{T}_7$  production. The remainder of  $\Delta E_{\text{non}}$  is deposited locally as recoil energy of the helium and tritium produced. The following questions remain:

1. How much of  $\Delta E_{n,1}$  for lithium reappears as inelastic  $\gamma$ -rays and what are their energies?
2. What fraction of  $\Delta E_{n,xn}$  for lithium is deposited locally as recoil energy of the lithium nuclei?

Detailed estimates were made for Item 2, using MCN cross-sections,  $(n,xn)$  neutron production spectra, and calculated fluxes, plus equations for recoil energy from Ref. 38. (Isotropic center-of-mass neutron emission was assumed.) The results gave

$\sim 22\%$  of  $\Delta E_{n,xn}$  deposited, with a maximum variation over the blanket of  $\sim 2\%$ . (A constant 22% was assumed.)

Item 1 poses a more basic, and more important problem. It is basic, because the data required to unequivocally assign lithium inelastic-scattering  $\gamma$ -ray spectra (and, thus, the  $\gamma$ -ray production fractions) are apparently not available; it is important, because heating in internal structures, especially structures such as the inner wall, can be predominantly from the lithium inelastic-scattering  $\gamma$ 's. Estimates of these heating rates are sensitive to the lithium inelastic- $\gamma$  spectrum assumed; in general, a softer lithium  $\gamma$ -ray spectrum will imply a higher inner-wall heating rate.

Addendum 2 to this Appendix discusses the approach which was used for lithium inelastic  $\gamma$ 's in the present case, based upon inelastic-scattering  $\gamma$ -ray spectra from Ref. 38. Although still uncertain, this approach was used because it constitutes an example of a spectral model that includes both the dominant scattering from low-lying levels (0.478 MeV in  ${}^7\text{Li}$  and 3.56 MeV in  ${}^6\text{Li}$ ) as well as an evaporation component for very-high-energy neutrons (14 MeV). The development in Addendum 2 uses, in effect, only the  $\gamma$ -spectra from Ref. 38; the overall inelastic-scattering energy balance is based upon the Monte Carlo-calculated energy changes. It is important to note, however, that there is an inconsistency in this approach. The MCN code assumes  $(n,n'\gamma)$  scattering only from the low-lying levels of lithium; thus, the resultant total Monte Carlo lithium inelastic- $\gamma$  energy is lower than that implied by the assumed spectra from Ref. 38.

Using results from Addendum 2 and from Table A-II,  $\gamma$ -source intensities and spectra were inferred for the cells of Table A-I. Gamma-ray transport calculations were then performed to estimate secondary  $\gamma$ -heating rates throughout the system.

These results were normalized to a given pellet output on the basis of the following assumptions:

$\alpha$ -particle deposition in the pellet	3.52 MeV
Nuclear energy absorbed in the pellet	0.89 MeV
Neutron leakage from the pellet	12.2 MeV
$\gamma$ -ray leakage from the pellet	<u>0.9 MeV</u>
Total energy per (D+T) reaction in the pellet.	17.51 MeV

Final neutron heating-rate estimates were made by multiplying the point-source values by  $(12.2/14.1) = 0.865$ . Tritium production rates were similarly estimated. These results are given in Table A-III and Fig. A.4. The total energy available in the system is  $13.43 + 3.52 + 0.89 = 17.84$  MeV per (D+T) reaction.

Note that an error is implicit in this normalization. It assumes that 0.865 neutrons per (D+T) reaction leave the pellet, with each neutron having an energy of 14.1 MeV. This is probably adequate for estimating direct neutron-energy deposition rates, but may not be adequate for  ${}^6\text{Li}(n,\alpha)\text{T}$  estimates. If low-energy neutrons escape from the pellet after having deposited some of their energy in the pellet, a correction might be required. For example, if an additional  $(1.0 \cdot 0.865) = 0.135$  neutrons per (D+T) are assumed to be of this type, then a potential (maximum) increase in T of 0.135, and an increase in blanket energy deposition of  $(0.135)(4.79) = 0.65$  MeV are possible per (D+T) reaction. These effects (< 10% increase, in T, < 4% increase in available energy) can be properly estimated only with coupled pellet-blanket calculations, which here are not justified.

An overall energy balance, based upon the stated normalization assumption and the Monte Carlo calculations, can be estimated as follows:

<u>Energy Produced/(D+T) Reaction:</u>	<u>Energy, MeV</u>
(D+T) reaction	17.62
${}^6\text{Li}(n,\alpha)\text{T}$ reactions = $(0.771)(4.79)$	<u>3.69</u>
Total	21.31

<u>Energy Loss/(D+T) Reaction:</u>	
Binding-energy loss in ${}^7\text{Li}(n,n'\alpha)\text{T}$ reactions = $(0.584)(2.47)$	1.44
Binding-energy loss in (n,xn) reactions	0.49
Loss in capture reactions, e.g., (n,p), (n,D)	0.55
$\gamma$ -ray leakage from the blanket	0.48
Neutron leakage from the blanket	0.12
Assumed pellet losses	0.11
Miscellaneous other losses	0.28
Energy deposited	<u>17.84</u>
Total	21.31

<u>Energy Deposited/(D+T) Reaction:</u>	<u>Energy, MeV</u>
Pellet	4.41
Cavity total (minus the pellet)	0.072
Inner wall	0.470
Inner lithium blanket	11.045
Main pressure vessel	0.951
Outer lithium blanket	0.772
Outer wall	<u>0.116</u>
Total	17.84

Although there are uncertainties in these estimates, they can hardly total more than ~ 1 MeV/(D+T) and they are probably smaller. Thus an upper limit of perhaps 18.5 MeV/(D+T) or, at most, 19 MeV/(D+T) is implied. The "correct" value for the ICTR system of Table A-I probably is 17.8 MeV ( $+0.7$   $-0.3$  MeV)/(D+T) reaction.

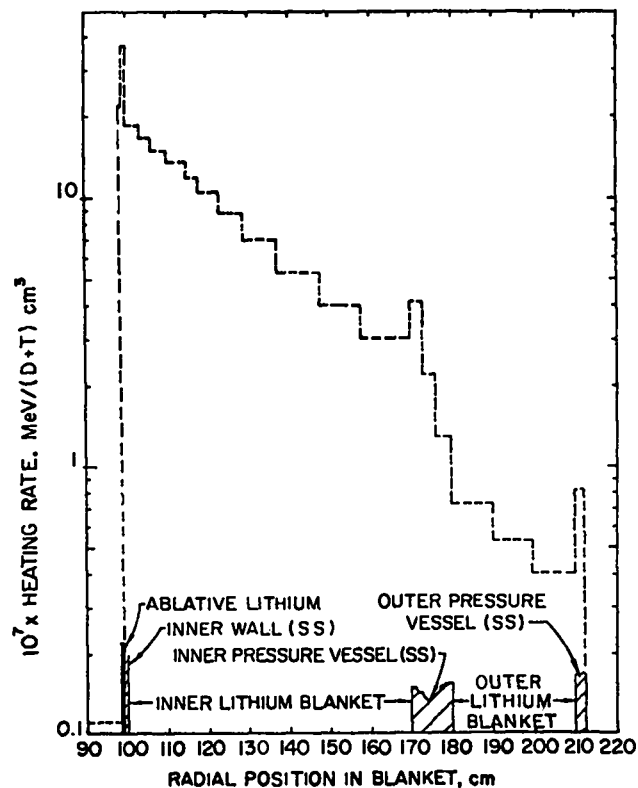


Fig. A-4. Blanket heating-rate distribution for configuration of Table A-III.

TABLE A-III

ESTIMATED ENERGY DEPOSITION AND TRITIUM PRODUCTION IN THE 200-MWt ICTR  
CONFIGURATION OF TABLE A-I

Cell	MeV/(D+T)			Tritium Production/(D+T)		
	Neutrons	Pellet $\gamma$ -rays	Total	$T_6$	$T_7$	T
1	0.045	0	0.045	0.0007	0.0042	0.0049
2	0.024	0.003	0.027	0.0009	0.0009	0.0018
3	0.270	0.200	0.470	0.0031	0.0055	0.0086
4	0.737	0.055	0.792	0.0239	0.0422	0.0661
5	0.694	0.050	0.744	0.0273	0.0446	0.0719
6	0.762	0.053	0.815	0.0317	0.0541	0.0858
7	0.738	0.048	0.786	0.0301	0.0441	0.0742
8	0.787	0.049	0.836	0.0365	0.0478	0.0843
9	0.911	0.054	0.965	0.0472	0.0539	0.1001
10	1.010	0.055	1.065	0.0541	0.0560	0.1101
11	1.170	0.060	1.230	0.0723	0.0639	0.1362
12	1.380	0.064	1.444	0.1005	0.0624	0.1629
13	1.196	0.050	1.246	0.1048	0.0496	0.1544
14	1.082	0.040	1.122	0.1185	0.0405	0.1590
15	0.431	0.069	0.500	0.0042	0.0009	0.0051
16	0.249	0.031	0.280	0.0035	0.0003	0.0038
17	0.158	0.013	0.171	0.0024	0.0001	0.0025
18	0.307	0.003	0.310	0.0432	0.0058	0.0490
19	0.249	0.001	0.250	0.0361	0.0047	0.0408
20	0.211	0.001	0.212	0.0298	0.0027	0.0325
21	0.115	0.001	0.116	0	0	0
Total	12.53	0.90	13.43	0.771	0.584	1.355

RELATIVE IMPORTANCE OF VARIOUS  
LITHIUM REACTIONS IN AN ICTR

14-MeV NEUTRON NONELASTIC REACTIONS  
IN NATURAL LITHIUM

Relative importances for the various neutron reactions in a lithium ICTR blanket can be evaluated by examining the flux-weighted microscopic cross sections for these reactions as a function of position in the blanket. The importance from the standpoint of energy deposition in the blanket and, secondarily, the importance with respect to tritium production in the blanket are of interest.

Lithium nonelastic reactions that must be considered, along with appropriate Q-values, are listed in Table A-IV. Point cross sections for these reactions were taken directly from the MCN Monte Carlo library and used to estimate rough group-averaged cross-sections in the energy groups,  $\Delta E_j$ , for which Monte Carlo fluxes were calculated. These cross sections were then used to estimate the percent of all nonelastic reactions in natural lithium for each reaction, as shown in Table A-V.

Tables A-IV and A-V indicate that, with an error of less than 5%, we can ignore energy deposition from all reactions except  ${}^6\text{Li}(n,\alpha)\text{T}$ , and  $\gamma$ -rays from  ${}^7\text{Li}(n,n'\gamma){}^7\text{Li}$  and  ${}^7\text{Li}(n,n'\alpha)\text{T}$  reactions. (This latter reaction probably produces no  $\gamma$ 's). Net energy losses to binding energy in  ${}^7\text{Li}(n,n'\alpha)\text{T}$  and in  $(n,xn)$  reactions should also be considered.

Reaction	Q-Values, MeV
${}^6\text{Li}(n,n'\gamma){}^6\text{Li}$	--
${}^6\text{Li}(n,n'\alpha)\text{D}$	-1.47
${}^6\text{Li}(n,2n\alpha)\text{p}$	-3.70
${}^6\text{Li}(n,\gamma){}^7\text{Li}$	+7.25
${}^6\text{Li}(n,\text{p}){}^6\text{He}$ ( ${}^6\text{He} \rightarrow {}^6\text{Li}$ )	-2.73 +0.815
${}^6\text{Li}(n,\alpha)\text{T}$	+4.79
${}^7\text{Li}(n,n'\gamma){}^7\text{Li}$	--
${}^7\text{Li}(n,2n){}^6\text{Li}$	-7.25
${}^7\text{Li}(n,n'\alpha)\text{T}$	-2.47
${}^7\text{Li}(n,2n\alpha)\text{D}$	-8.72
${}^7\text{Li}(n,\gamma){}^8\text{Li}$ ( ${}^8\text{Li} \rightarrow 2 {}^4\text{He}$ )	+2.03 +15.9
${}^7\text{Li}(n,\text{D}){}^6\text{He}$	-7.76

TABLE A-V

PERCENT OF ALL LITHIUM NONELASTIC REACTIONS, IN NATURAL-LITHIUM BLANKET

Reaction	Distance into the Blanket, cm					
	1	7	20	40	160	300
${}^6\text{Li}(n,n'\gamma){}^6\text{Li}$	0.2	0.1	0.1	0.1	~ 0	~ 0
${}^6\text{Li}(n,n'\alpha)\text{D}$	5.3	5.2	4.8	3.9	0.6	~ 0
${}^6\text{Li}(n,2n\alpha)\text{p}$	0.4	0.4	0.3	0.2	~ 0	~ 0
${}^6\text{Li}(n,\gamma){}^7\text{Li}$	~ 0	~ 0	~ 0	~ 0	~ 0	~ 0
${}^6\text{Li}(n,\text{p}){}^6\text{He}$	0.1	0.1	0.1	0.1	~ 0	~ 0
${}^6\text{Li}(n,\alpha)\text{T}$	30.8	33.2	38.6	50.9	92.3	97.3
${}^7\text{Li}(n,n'\gamma){}^7\text{Li}$	24.3	25.1	25.0	21.9	4.6	2.3
${}^7\text{Li}(n,2n){}^6\text{Li}$	1.5	1.3	1.1	0.7	0.1	~ 0
${}^7\text{Li}(n,n'\alpha)\text{T}$	35.1	32.7	28.5	21.2	2.3	0.1
${}^7\text{Li}(n,2n\alpha)\text{D}$	1.7	1.4	1.1	0.7	~ 0	~ 0
${}^7\text{Li}(n,\gamma){}^8\text{Li}$	~ 0	~ 0	~ 0	~ 0	~ 0	~ 0
${}^7\text{Li}(n,\text{D}){}^6\text{He}$	0.6	0.5	0.4	0.3	~ 0	~ 0

INELASTIC SCATTERING SOURCES FOR LITHIUM

The Monte Carlo code used for ICTR heating estimates in this study includes as one of its options a cell-wise tally of  $\Delta E_{n,1}^n$  = neutron energy lost in  $(n,n'\gamma)$  reactions in lithium. To estimate the resulting energy deposition it is necessary to estimate what fraction of  $\Delta E_{n,1}^n$  is deposited as energy of the lithium recoil nuclei, and what fraction reappears as inelastic-scattering  $\gamma$ -rays. The energy spectrum of these  $\gamma$ -rays must also be determined. This latter problem is particularly difficult if the inelastic scattering occurs via several nuclear levels, plus continuum-region scattering; the neutron spectrum varies greatly from inside to outside in a typical CTR blanket and, in general, this implies a position-dependent inelastic- $\gamma$  spectrum. Corresponding recoil energies for the lithium nuclei must also be estimated, since this fraction of  $\Delta E_{n,1}^n$  is deposited locally, in contrast to the inelastic  $\gamma$ 's.

Such problems have been examined by Ritts, Solomito, and Steiner.<sup>(38)</sup> In that study, inelastic scattering was assumed to be via the 0.478-MeV level in  ${}^7\text{Li}$  and the 3.56-MeV level in  ${}^6\text{Li}$ , plus a continuum region in which an evaporation scattering model was used for incident neutron energies above 9 MeV. Resulting group-wise secondary  $\gamma$ -ray spectra are tabulated in this reference for 100 neutron-energy groups between 0.414 eV and 14.92 MeV.

For the present work, the ORNL inelastic-scattering  $\gamma$ -ray production spectra will be normalized to the MCN-calculated neutron-energy losses to obtain inelastic- $\gamma$  sources for  $\gamma$ -heating estimates. Corresponding recoil energies will also be estimated that are consistent with the ORNL spectra.

To do this, consider only  $(n,n'\gamma)$  events in lithium and assume isotropic emission of the  $n'$  neutrons in the center-of-mass system (energies are in the laboratory system). The following definitions will be used:

- i = incident neutron energy (or group) index,
- j = excitation energy (or group) index, for an  $(n,n')$  event in lithium,
- k = position (or region) index,

- $E_i$  = incident neutron energy,
- $E_{ij}^n$  = excitation energy of the residual nucleus after  $(n,n')$  scattering of a neutron with incident energy  $E_i$ ,
- $E_{ij}^n$  = energy of the outgoing neutron in an  $(n,n')$  event which leaves the residual nucleus with excitation energy  $E_{ij}^n$  (incident neutron energy =  $E_i$ ),
- $E_{ij}^r$  = energy of recoil nucleus for  $(n,n')$  event as above,
- $f_{ij}$  = fraction of  $(n,n')$  events which produce residual nuclei with excitation energy  $E_{ij}^n$ ,
- $\phi_{ik}$  = flux at position k of neutrons with energy  $E_i$ ,
- $\sigma_{ik}$  =  $(n,n'\gamma)$  cross section at position k for neutrons of energy  $E_i$ ,
- $\Delta E_k^n$  = calculated total neutron energy change at position k via  $(n,n')$  reactions, per source neutron.

Thus, by the above definitions,

$$\Delta E_k^n = A_k \sum_i \sum_j f_{ij} \sigma_{ik} \phi_{ik} (E_i - E_{ij}^n) \quad (\text{A-1})$$

where the  $A_k$  are products of the proper normalization factors, as required. Also, via an energy balance for a given  $(n,n')$  event,

$$E_i = E_{ij}^n + E_{ij}^r + E_{ij}^r. \quad (\text{A-2})$$

The mechanics of the  $(n,n')$  scattering event are described by the following (see Ref. 38):

$$E_{ij}^r(\theta) = \frac{2 A E_i}{(1+A)^2} \left[ 1 - \frac{(1+A)E_{ij}^n}{2 A E_i} - \sqrt{1 - \frac{(1+A)E_{ij}^n}{A E_i} \cos \theta} \right],$$

where A is the ratio of the nuclear mass to the neutron mass, and  $\theta$  is the center-of-mass (c.m.) scattering angle. If isotropic c.m. scattering is assumed,\*

$$E_{ij}^r = \left[ E_{ij}^r(\theta) \right]_{\text{av}} = \frac{2 A E_i}{(1+A)^2} \left[ 1 - \frac{(1+A)E_{ij}^n}{2 A E_i} \right]. \quad (\text{A-3})$$

\*There are data which indicate that this may not be a good assumption for 14-MeV neutrons in lithium, and a significant error can be implied. However, available data are not sufficient to allow a better analysis at this time; further, the Monte Carlo calculations use isotropic inelastic scattering models. Any other assumption would, therefore, be inconsistent with the MCN results.

Finally, the total recoil energy at k is

$$\Delta E_k^r = A_k \sum_i \sum_j f_{ij} \phi_{ik} \sigma_{ik} E_{ij}^r$$

Thus, the fraction of  $\Delta E_k^n$  that reappears as recoil energy of the lithium nuclei is

$$\beta_k = \frac{\Delta E_k^r}{\Delta E_k^n} = \frac{\sum_i \sum_j f_{ij} \phi_{ik} \sigma_{ik} E_{ij}^r}{\sum_i \sum_j f_{ij} \phi_{ik} \sigma_{ik} (E_i - E_{ij}^n)} \quad (A-4)$$

The excitation energy,  $E_{ij}^Y = E_{ij} - E_{ij}^r$ , is assumed to reappear as a single photon of energy  $E_{ij}$ .

To estimate  $\beta_k$  and the resultant inelastic- $\gamma$  spectrum, the following energy groups are assumed (corresponding to intervals in the tables of Ref. 38.)

γ-Ray Groups		
j	$\Delta E_{ij}$ (MeV)	Assumed $E_{ij}$ (MeV)
1	12 to 14.1	12.3
2	10 to 12	11.0
3	8 to 10	9.0
4	3.5 to 4	3.56
5	0.4 to 1.0	0.478

Neutron Energy Groups		
i	$\Delta E_i$ (MeV)	Assumed $E_i$ (MeV)
1	13.5 to 14.92	14.1
2	12.21 to 13.5	12.9
3	11.05 to 12.21	11.6
4	10.0 to 11.05	10.5
5	9.048 to 10.0	9.52
6	8.187 to 9.048	8.62
7	6.703 to 8.187	7.45
8	5.488 to 6.703	6.10
9	4.066 to 5.488	4.78
10	3.012 to 4.066	3.54
11	2.019 to 3.012	2.52
12	1.353 to 2.019	1.69
13	0.9072 to 1.353	1.13
14	0.4979 to 0.9072	0.70

Data for  ${}^7\text{Li}$  and  ${}^6\text{Li}$ , from Tables 6 and 7 of Ref. 38, can be collapsed and combined to produce estimates of  $(f_{ij} \sigma_{ik})$  in natural lithium for these groups. Using Eq. (A-3),  $E_{ij}^r$  can be calculated as a function of  $E_i$  and  $E_{ij}$ ; with these results, Eq. (A-2), Eq. (A-4) and the Monte Carlo fluxes,  $\beta_k$  can be calculated as a function of position in the blanket of the ICTR system of Table A-I. These results are given in Table A-VI.

The spectrum of the resulting inelastic  $\gamma$ -rays can also be estimated as a function of position:

$$\alpha_{jk} = \frac{\text{fraction of the total inelastic-}\gamma \text{ energy at k that is emitted in } \gamma\text{-group j}}{\sum_j \sum_i f_{ij} \sigma_{ik} \phi_{ik} E_{ij}} = \frac{\sum_i f_{ij} \sigma_{ik} \phi_{ik} E_{ij}}{\sum_j \sum_i f_{ij} \sigma_{ik} \phi_{ik} E_{ij}}$$

Table A-VII gives the resulting  $\alpha_{jk}$ . (Note the large variation in these spectra as a function of position in the blanket.)

In summary, to get lithium inelastic- $\gamma$  sources for the geometry of Table A-I, the Monte Carlo-calculated  $\Delta E_k^n = \Delta E_{n,1}^k$  (from Table A-II) are multiplied by the appropriate  $(1-\beta_k)$  from Table A-VI, to get  $\gamma$ -source intensities. These are then assumed to have the spectra of Table A-VII. In addition, a fraction,  $\beta_k$ , of  $\Delta E_{n,1}^k$  is deposited locally as lithium recoil energy.

TABLE A-VI

$\beta_k$  vs POSITION IN ICTR OF TABLE A-I

k	r (cm)	$\beta_k$	$1 - \beta_k$
1	98.9	0.378	0.622
2	100.0	0.384	0.616
3	103.25	0.390	0.610
4	110.2	0.410	0.590
5	118.08	0.422	0.578
6	129.22	0.432	0.568
7	147.76	0.442	0.558
8	169.55	0.419	0.581
9	179.55	0.391	0.609
10	189.55	0.402	0.598
11	209.55	0.416	0.584

TABLE A-VII

$\alpha_{ij}$  = FRACTION OF TOTAL INELASTIC  $\gamma$ -RAY ENERGY CARRIED BY PHOTONS WITH ENERGY  $E_j$  (MeV), vs POSITION IN THE BLANKET OF ICTR SHOWN IN TABLE A-I

$r$ (cm)	$\alpha_{ij}$				
	$E_j = 12.3$ MeV	11.0	9.0	3.56	0.478
98.9	0.248	0.318	0.002	0.004	0.428
100.0	0.237	0.307	0.004	0.004	0.448
103.25	0.216	0.309	0.010	0.004	0.461
110.2	0.178	0.300	0.018	0.004	0.500
118.08	0.144	0.284	0.025	0.004	0.543
129.22	0.110	0.262	0.032	0.004	0.592
147.76	0.073	0.227	0.041	0.004	0.655
169.55	0.042	0.173	0.048	0.003	0.734
179.55	0.027	0.105	0.021	0.002	0.845
189.55	0.025	0.104	0.036	0.002	0.833
209.55	0.018	0.097	0.040	0.002	0.843

APPENDIX B

METHODS OF CALCULATION

by A. R. Larson and L. A. Booth

1. Pellet-Wetted-Wall Interaction and Wall-Strain Analysis

The finite-difference technique in solving Eqs. (1), (2), (3), (27), and (29) (see main body of report) is based on the following sequence. At the beginning of each time interval (computation cycle), new velocities for each zone boundary are determined from previous pressure gradients, Eq. (2). From the new velocities, the changes in zone boundaries are computed ( $\Delta R = U\Delta t$ ). Densities are computed next, Eq. (1), and time-centered by averaging with old values. New specific internal energies and pressures are then computed by iteration of temperatures to satisfy Eq. (3) or (27) and the equation of state (see Appendix C) by using the time-centered densities. Viscous pressures,  $Q$ , are calculated by the method of von Neumann and Richtmyer, (39) viz.

$$Q = \begin{cases} \ell^2 \rho \left( \frac{\partial u}{\partial r} \right)^2 & \text{for } \frac{\partial u}{\partial r} < 0 \\ \text{zero} & \text{for } \frac{\partial u}{\partial r} \geq 0 \end{cases} \quad (\text{B-1})$$

where  $\ell^2$  is the damping coefficient. The time interval for the next computation cycle is based on the Courant-Friedrichs-Lewy condition (40), and is determined by:

$$\frac{\Delta t}{\Delta R} \leq \frac{1}{2\ell s} \sqrt{\frac{2\eta}{\eta+1}} \left( \frac{1}{\eta-1} \right), \quad (\text{B-2})$$

where  $s$  is the time derivative of the shock's Lagrangian coordinate and  $\eta$  is the volume compression ratio of the shock. With this new time interval, pressure, and viscous pressure, the next computation cycle is started as before.

2. Radiation Transport across the Void for Pellet/Wetted-Wall Analysis

The energy equation, Eq. (3) of the main body of the report, includes a diffusion equation to transfer electromagnetic radiation across zone boundaries, i.e.,

$$F = \frac{ac}{3} A \lambda \text{ grad } \theta^4 \quad (\text{B-3})$$

$F$  = energy flux (erg/sec)

$a = 4\sigma/c k^4$

$\sigma$  = Stefan-Boltzmann constant  
( $5.67 \times 10^{-5}$  erg sec $^{-1}$  cm $^{-2}$  K $^{-4}$ )

$c$  = speed of light in vacuum

$\lambda$  = mean free path for radiation (an average of the mean free paths on either side of the boundary)

$T$  = temperature

$k$  = Boltzmann constant ( $1.381 \times 10^{-16}$  erg/K)

$\theta = kT$

$A$  = area

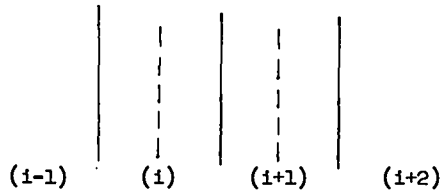
In finite-difference form Eq. (B-3) becomes

$$F = \left( \frac{ac}{3} \frac{\lambda}{\Delta r} \right) 4 A \bar{\theta}^3 \Delta \theta \quad (\text{B-4})$$

where  $\Delta r$  is a distance across a zone. Values of  $\bar{\theta}$  and  $\Delta r/\lambda$ , the numbers of mean free paths, are determined by averaging the values for the zones on each side of the interface for which  $F$  is applicable.

Equations (B-3) and (B-4) are appropriate if matter is present. In this calculation, however, a large void is assumed at the start of the calculation, and these equations therefore are inappropriate. To treat the radiation transport across this void, an improved formulation was devised without a major modification to the code.

The void region is divided into several zones, two of which (i and i+1) are considered here.



An imaginary radiating surface (indicated by dotted lines) is placed at the center of each zone. According to Huygen's principle, the wave front at the center of Zone (i+1) can be generated from a wave front at the center of Zone i. Energy densities for each zone,  $\epsilon_i$ , are calculated in the code by integrating the fluxes across the boundaries over time. Zone temperatures are then calculated from  $\epsilon_i = a \theta_i^4$ . Assuming that this is a reasonable approximation for  $\theta_i$  and that Huygen's principle can be used, the energy flux between the two imaginary surfaces is

$$F = \frac{ac}{4} (A_{i+1} \theta_{i+1}^4 - A_i \theta_i^4). \quad (B-5)$$

If the zone thicknesses are small,  $A_{i+1} \approx A_i = A$  (A is the area of the surface between the zones.) Then

$$F = \frac{ac}{4} A (\theta_{i+1}^4 - \theta_i^4) \\ = \frac{ac}{4} A \langle \theta^2 \rangle \langle \theta \rangle (\theta_{i+1} - \theta_i), \quad (B-6)$$

or

$$F = ac A \bar{\theta}^3 \Delta \theta, \quad (B-7)$$

where  $\langle \theta \rangle$  is the average value of  $\theta$ .

In Eq. (B-4),  $\theta$  has the same value as  $\bar{\theta}$  in Eq. (B-7) when  $\theta_i$  or  $\theta_{i+1}$  approaches zero. Upon comparing Eq. (B-4) and (B-7), approximate radiation transport can be calculated across a void if  $\frac{4}{3} \frac{\lambda}{\Delta t}$  is replaced by unity in Eq. (B-4).

### 3. Lithium Vaporization for Pellet-Wetted-Wall Analysis

The computer code used in this calculation includes an explicit scheme for solving the hydrodynamic equation in the Lagrangian-space coordinate

system and is not applicable for a liquid or solid phase. In the explicit scheme, zone boundary motion for a given time step is determined only by the pressures on each side of the boundary at the beginning of the time step. In using the liquid-lithium equation-of-state (see Appendix C), the liquid-zone pressures varied irrationally, resulting in an unrealistically low value for the time step.

The following modifications were made to alleviate this problem. The vaporization temperature of the lithium was arbitrarily assumed to be 5800 K--lithium zones below this temperature were liquid and those above were gaseous. All liquid zones had the same pressure as the gas zone adjacent to the liquid, resulting in no hydrodynamic motion for the liquid. The Courant time-step calculation was modified to allow the time step to increase without limit as adjacent gas-zone pressures become equal.

### 4. Analysis of Blowdown through Condenser

The finite-difference technique in solving Eqs. (10) through (14) is the backward-space difference method of Richtmyer for Eulerian equations. (41)

Equations (15) through (19) were differenced in a similar manner. The sequence of calculations during each time interval (computation cycle) was as follows. New velocities were calculated for both the liquid and the gas phase (Eq. 12) by using the combined density, pressures, and viscous pressures from the previous computation cycle (initial conditions for the first cycle). Changes in mass and energy (Eqs. 10, 11, 13, and 14) in each zone were then calculated by using the new velocities and time-centered densities. Gas pressures were calculated by Eq. (20), and compared with the vapor pressure (Eq. C-1, Appendix C). If the gas was superheated, the temperature was changed by the heat-transfer Eq. (15). After a zone became saturated, the changes in temperature (and energy), mass, density, and void fraction were calculated by Eqs. (16) through (19), and Eq. (C-1) was the equation-of-state. The viscous pressures and the new time interval were calculated from Eqs. (B-1) and (B-2), and the next computation cycle started as before.

APPENDIX C

PHYSICAL PROPERTIES OF LITHIUM

by J. C. Hedstrom and A. R. Larson

1. General

Transport and thermodynamic state properties of lithium have been obtained from the open literature, where possible. Liquid-lithium densities, viscosities, and thermal conductivities used for the various analyses in Section II of the report were obtained from three sources. (21,22,42)

2. High-Temperature Properties for Pellet Wetted-Wall Interaction Analyses

For the pellet wetted-wall analysis, the state (pressure and internal energy) and transport (radiation-absorption cross section, i.e., opacity, and thermal conductivity) properties were needed over a temperature range of 0.09 to 20.0 eV and a density range of  $2.7 \times 10^{-6}$  to  $0.534 \text{ g/cm}^3$ . The data used in the calculations were calculated at LASL<sup>(43)</sup> and were included in a tabular interpolation subroutine in the computation code. The opacity data included electron thermal conductivity.

The most uncertain of these properties is the opacity. Some calculated data are plotted in Fig. C.1, in which the wide variability of opacity is illustrated. Missing sections in the curves indicate ranges for which data could not be computed, and interpolated values were used. For the particular calculation in Section II.B.2 of the report the temperature-density points were such that the interpolated values were, for the most part, outside the region of interest. This is illustrated by a domain diagram in Fig. C.2. Values for  $T \leq 0.2 \text{ eV}$  (which are the most uncertain of those shown) are accurate within a factor of 2.

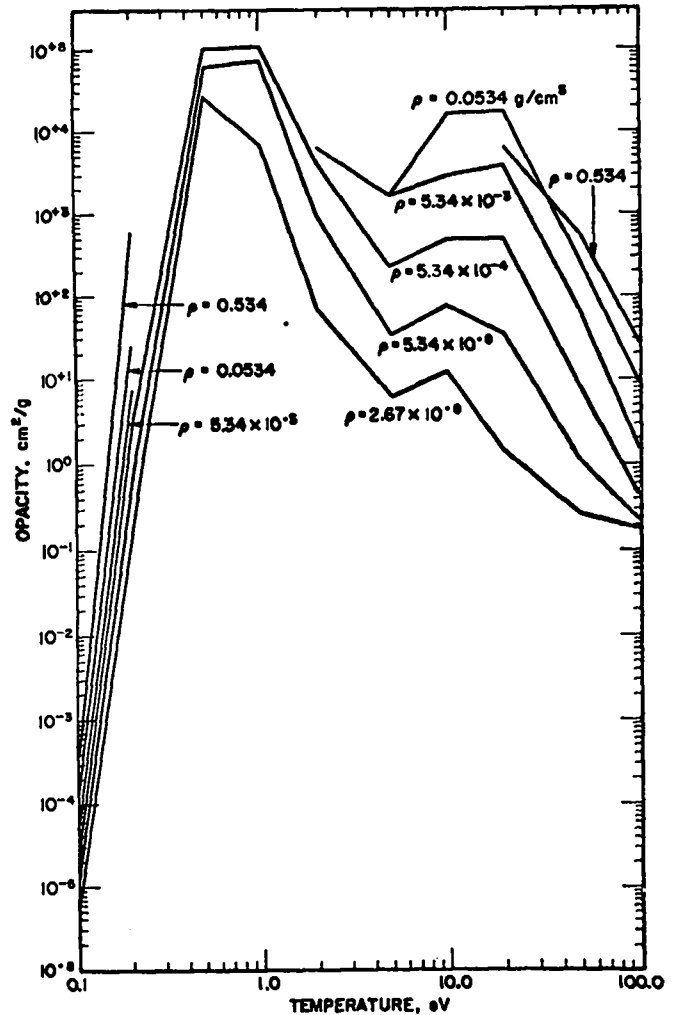


Fig. C.1. Calculated lithium opacity (including electron conduction) as a function of temperature.

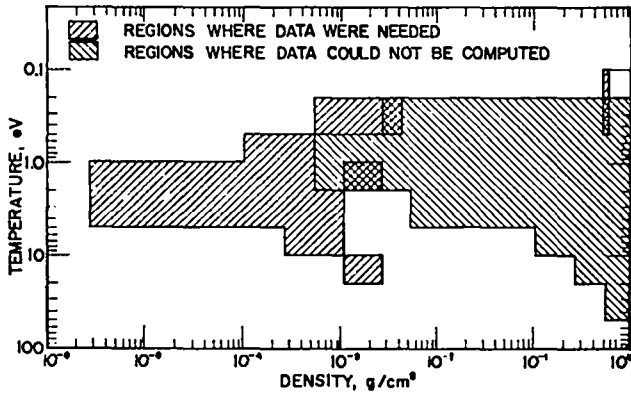


Fig. C.2. Temperature and density domains that were used in pellet wetted wall interaction calculations.

The tabular interpolation subroutine includes the calculated data in the following form:

The dependent variables are the logarithms of:

- $P_0$ , the pressure at zero temperature,
- $P-P_0$ , where  $P$  is the pressure,
- $E_0$ , specific internal energy at zero temperature,
- $E-E_0$ , where  $E$  is the specific internal energy, and
- $\kappa$ , the opacity (includes electron heat conductivity).

The independent variables are logarithms of:

$kT$ , where  $T$  is the temperature and  $k$  is Boltzmann's constant; and  $\rho/\rho_0$ , the compression, where  $\rho$  is the density and  $\rho_0$  is the density at zero temperature.

Lower and upper limits on  $kT$  and  $\rho/\rho_0$  may be chosen for each material. The interpolation points for  $P-P_0$ ,  $E-E_0$ , and  $\kappa$  are evenly spaced (on a logarithmic scale) between the lower and upper limits to minimize computer time. Values of the logarithm of  $kT$  and  $\rho/\rho_0$  for  $P_0$  and  $E_0$  are fixed.

### 3. Equation-of-State for Cavity Equilibration, Blowdown, and Condenser Analyses

For these analyses, the state properties for saturation and superheated vapor conditions must be obtained. However, because complete pressure-dependent properties are not available, an equation-of-state model was developed, based on data from the JANAF Thermochemical Tables<sup>(44)</sup>. This model, which assumes a perfect gas for the superheated vapor, includes the following from the JANAF data.

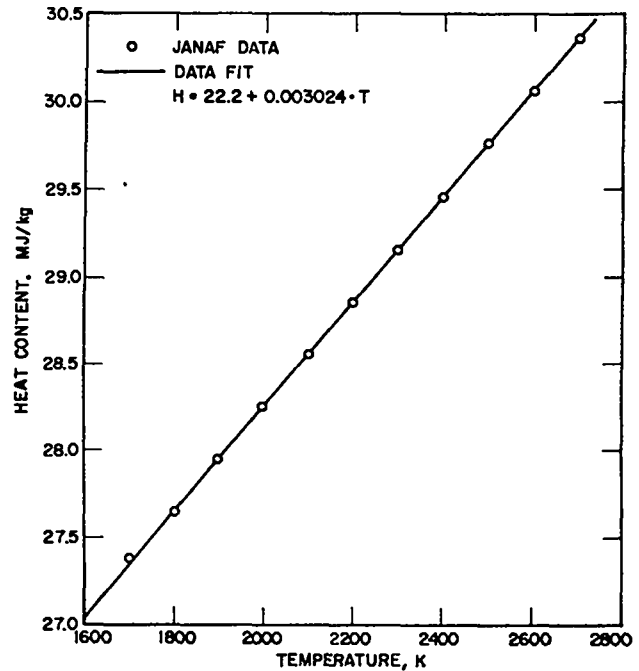


Fig. C-3. Heat content of saturated lithium vapor.

- Heat content of saturated vapor ( $H_v$ ) as a function of temperature, and
- Specific-heat ratio ( $\gamma$ ) as a function of temperature.

Heat content,  $H_v$ , as a function of vapor temperature is plotted in Fig. C.3 along with a linear fit to the data. Values of  $\gamma$  were calculated from the  $C_p$  data, assuming  $\gamma = C_p / (C_p - R)$ . Results are plotted in Fig. C.4 again with an analytic fit to the data. The dip due to the increase in dimer concentration was ignored because it is generally below the current range of interest.

The saturation conditions were determined by calculating vapor pressures from the equilibrium constant data. The relationship which fits these results is:

$$P_v = \exp [25.3794 - 17754.9/T_v - 0.39515 \ln T_v], \quad (C-1)$$

where  $P_v$  is the saturation pressure and  $T_v$  is the saturation temperature.

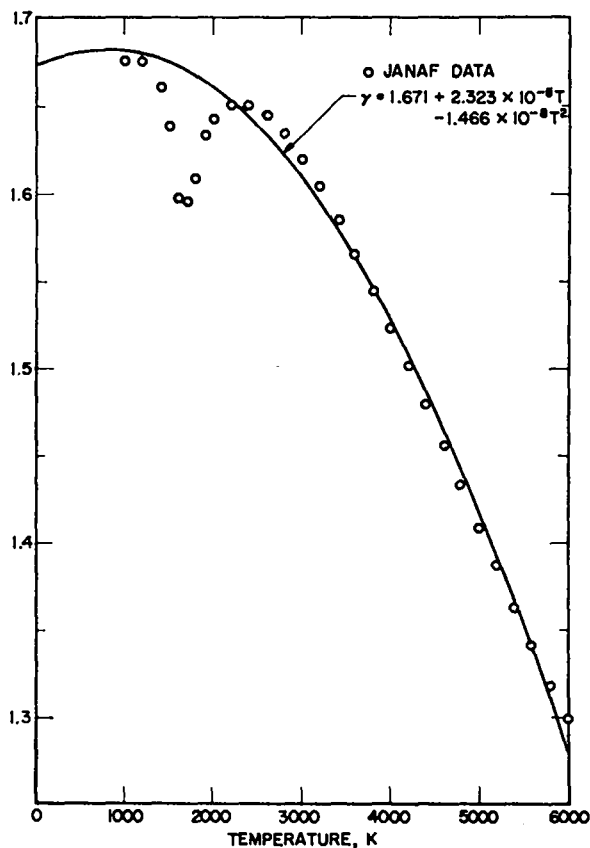


Fig. C.4. Ratio of specific heats ( $\gamma$ ) of lithium vapor assuming perfect gas.

The internal energy is then given by

$$E = H_V + R \int_{T_V}^T \frac{dT}{(\gamma-1)}, \quad (C-2)$$

and the pressure is given by

$$P = \rho RT = P_V \cdot T/T_V. \quad (C-3)$$

These three equations are the basis for the pressure-temperature diagram in Fig. 6 of the report.

The constant energy/volume line in Fig. 6 was derived by combining Eqs. (C-2) and (C-3) to obtain:

$$\frac{I}{V} = \frac{P_V}{T_V} \frac{H_V - E_0}{R} + \int_{T_V}^T \frac{dT}{\gamma-1} \quad (C-4)$$

where

$I$  = total energy in the cavity lithium after pellet initiation,

$E_0$  = initial specific internal energy of lithium vapor in the cavity prior to pellet initiation.

$P_V$  is evaluated by Eq. (C-1),  $H_V$  is evaluated by the data fit in Fig. C.3, and  $\gamma$  is evaluated by the data fit in Fig. C.4.

Given  $I$ ,  $V$ , and  $E_0$  and assuming a final  $T$ , this equation can be solved iteratively for  $T_V$  from which the other parameters can be calculated. The operating line on Fig. 6 is for  $I = 50$  MJ,  $V = 4.189$  m<sup>3</sup> (1.0 m radius), and  $E_0 = 2.09$  MJ/kg (saturated vapor assumed at 700 K). The conditions in Table I of the report are also calculated on this operating line from Eq. (C-4).

#### 4. Liquid Equation-of-State for Blanket Response Analysis

The equation-of-state for liquid lithium is developed from the definitions of the volumetric coefficient of thermal expansion and the compressibility coefficient. The compressibility coefficient is

$$\beta_c = - \frac{1}{V} \left( \frac{\partial V}{\partial P} \right)_T, \quad (C-5)$$

and the coefficient of thermal expansion is

$$\beta_T = \frac{1}{V} \left( \frac{\partial V}{\partial T} \right)_P. \quad (C-6)$$

Since  $v = f(T, P)$ , we have

$$dv = \left( \frac{\partial v}{\partial T} \right)_P dT + \left( \frac{\partial v}{\partial P} \right)_T dP. \quad (C-7)$$

Expressing the two coefficients, Eqs. (C-5) and (C-6), in terms of  $v$  and substituting in Eq. (C-7) gives

$$dP = - \rho \frac{dv}{\beta_c} + \frac{\beta_T}{\beta_c} dT$$

or

$$P = P_0 + \frac{\rho - \rho_0}{\rho_0 \beta_c} + \frac{\beta_T}{\beta_c} \frac{E}{C_p}, \quad (C-8)$$

where  $(T - T_0) = E/C_p$  and the subscript zero refers to a reference state.

For the calculations in Section II.C.3,  $\rho_0 = 507$  kg/m<sup>3</sup>,  $T_0 = 473$  K, and  $P_0 = 10^5$  N/m<sup>2</sup>. The compressibility coefficient ( $\beta_c$ ) was calculated from published data<sup>(45)</sup> to be  $1.42 \times 10^{-11}$  m<sup>2</sup>/N. Values of the other constants, taken from the literature,<sup>(21)</sup> were:  $C_p = 4183$  J/kg K;  $\beta_T = 1.38 \times 10^{-4}$  K<sup>-1</sup>.

#### REFERENCES

1. A. P. Fraas, "The BLASCON - An Exploding Pellet Fusion Reactor," USAEC Report ORNL-TM-3231, Oak Ridge National Laboratory (July, 1971).
2. "Design Study Report for TARGET, a 1000-MW(e) High Temperature Gas-Cooled Reactor," USAEC Report GA-4706, General Atomic Div. (1964).
3. D. J. Roehling, D. B. Fradkin, T. F. Stratton, "Experimental Performance of Supersonic Nozzles using Lithium Vapor as a Propellant," to be presented at AIAA 9th Electric Propulsion Conference, Bethesda, Md. (April, 1972).
4. J. E. Kemme, "Ultimate Heat-Pipe Performance," IEEE Trans. on Electron Devices, ED-16, No. 8, p. 717-723 (August, 1969).
5. E. E. Hoffman, "Corrosion of Materials by Lithium at Elevated Temperatures," USAEC Report ORNL-2674, Oak Ridge National Laboratory (1959).
6. T. E. Tietz, J. W. Wilson, "Behavior and Properties of Refractory Metals," Stanford University Press (1965).
7. G. L. Miller, "Metallurgy of the Rarer Metals - 6 Tantalum and Niobium," Academic Press (1959).
8. "Metals Handbook," Eighth Ed., American Society of Metals (1961).
9. "Aerospace Structural Metals Handbook," Syracuse University Press (1963).
10. H. Dreicer, D. B. Henderson, "Facility for Duplicating 14-MeV Neutron Effects in Fusion Power Reactors," USAEC Report LA-4709-MS, Los Alamos Scientific Laboratory (1971).
11. "Neutron Cross Sections," USAEC ENL-325, Second Ed., Brookhaven National Laboratory (1964 to 1966).
12. D. G. Martin, "Radiation Damage Effects in the Containment Vessel of a Thermonuclear Reactor," UKAEA Report CLM-R-103, Culham Laboratory (1970).
13. Cited in Ref. 12.
14. W. N. McElroy, N. Farrar IV, "Helium Production in Stainless Steel and its Constituents as Related to INFER Development Programs," USAEC Report HEDL-SA-193, Hanford Development Laboratories (1971).
15. W. V. Green, private communication, Los Alamos Scientific Laboratory (1971).
16. J. D. Lee, "Some Neutronic Aspects of a DT Fusion Reactor," USAEC Report UCRL-72493, Lawrence Radiation Laboratory (May, 1970).
17. A. P. Fraas, "Preliminary Appraisal of the Hazards Problems of a D-T Fusion Reactor Power Plant," USAEC Report ORNL-TM-2822, Oak Ridge National Laboratory (April, 1970).
18. D. Steiner, "The Neutron-Induced Activity and Decay Power of the Niobium Structure of a D-T Fusion Reactor Blanket," USAEC Report ORNL-TM-3094, Oak Ridge National Laboratory (August, 1970).
19. D. J. Dudziak, "A Technical Note on D-T Fusion Reactor Afterheat," Nuclear Technology, 10, p. 391 (March, 1971).
20. C. M. Lederer, J. M. Hollander, I. Perlman, "Table of Isotopes," Sixth Ed., John Wiley & Sons, Inc. (1967).
21. "Mellor's Comprehensive Treatise on Inorganic and Theoretical Chemistry - Volume I - Supplement II, The Alkali Metals, Part 1," Wiley and Sons (1961).
22. "Liquid Metals Handbook," USAEC, Dept. of Navy (1955).

23. E. F. Johnson, "Recovery of Tritium from Dilute Solutions of Lithium Tritide in Lithium," USAEC Report No. NYO-6370, Princeton University (1956).
24. A. P. Fraas, "A Diffusion Process for Removing Tritium from the Blanket of a Thermonuclear Reactor," USAEC Report ORNL-TM-2358, Oak Ridge National Laboratory (December, 1968).
25. R. W. Webb, "Permeation of Hydrogen through Metals," USAEC Report NAA-SR-10462, Atomic International (July, 1965).
26. A. P. Fraas, "Comparison of Two Tritium Removal Systems Designed to Minimize Contamination of Steam Systems in Full-Scale Thermonuclear Power Plants," USAEC Report ORNL-TM-2932, Oak Ridge National Laboratory (May, 1970).
27. "Standards for Radiation Protection," USAEC Manual Chapter 0524 (February, 1969).
28. J. D. Lane, M. L. Myers, R. C. Olson, "Power Plant Capital Cost Normalization," USAEC Report ORNL-TM-2385, Oak Ridge National Laboratory (June, 1969).
29. A. P. Fraas, "Conceptual Design of a Fusion Power Plant to Meet the Total Energy Requirements of an Urban Complex," Invited paper, Proceedings of the British Nuclear Energy Society Conference on Nuclear Fusion Reactors, Culham Laboratory (September, 1969).
30. C. Keller, "The Use of the Closed-Cycle Helium Gas Turbine in Atomic Power Plants," Escher Wyss News, 39, No. 1, 40 (1966).
31. J. A. Signorelli, "Perspective on Steam Cycles for Nuclear Power Costs," Nucleonics, 23, No. 4, p. 45 (April, 1965).
32. M. S. Lubell, et al, "Engineering Design Studies on the Superconducting Magnet System of a Tokamak Fusion Reactor," Proc. of Conf. on Plasma Physics and Controlled Nuclear Fusion, IAEA Paper CN-28/K-10, Madison, Wisc. (June, 1971).
33. F. L. Ribe, "Economic Considerations and Magnetic Energy Storage for High- $\beta$ , Pulsed Reactors," USAEC Report IA-DC-11330, Los Alamos Scientific Laboratory (1970).
34. "Civilian Nuclear Power: A Report to the President," with Supplement, USAEC, (1967), and as listed in "New York Times 1970 World Almanac," cited from Federal Power Commission Statistics (1971).
35. J. L. Tuck, "On Nuclear Fusion Objectives," Paper No. 1.1, Proceedings of the British Nuclear Energy Society Conference on Nuclear Fusion Reactors, Culham Laboratory (September, 1969).
36. E. E. Teller, Keynote address to 5th Intersociety Energy Conversion Engineering Conference, Las Vegas, Nevada (September, 1970).
37. E. D. Cashwell, J. R. Neergaard, W. M. Taylor, G. D. Turner, "MCN, A Monte Carlo Code," USAEC Report IA-4751, Los Alamos Scientific Laboratory (December, 1971).
38. J. J. Ritts, M. Solomito, D. Steiner, "KERMA Factors and Secondary Gamma-Ray Sources for Some Elements of Interest in Thermonuclear Blanket Assemblies," USAEC Report ORNL-TM-2564, Oak Ridge National Laboratory (June, 1970).
39. J. von Neumann and R. D. Richtmyer, "A Method for the Numerical Calculations of Hydrodynamical Shocks," J. Appl. Phys., 21, p. 232 (1950).
40. R. Courant, K. O. Friedrichs, H. Lewy, "Über die partiellen Differenzgleichungen der Mathematischen Physik," Math. Ann., 100, p. 32 (1928).
41. R. D. Richtmyer, "Difference Methods for Initial-Value Problems," Interscience Publishers, Inc., New York (1957).
42. C. L. Mantell, Ed., "Engineering Materials Handbook," McGraw-Hill (1958).
43. W. F. Huebner, A. L. Merts, unpublished work, Los Alamos Scientific Laboratory (1971).
44. D. R. Stull, et al, "JANAF Thermochemical Tables," PB 168 370, Clearinghouse for Federal Scientific and Technical Information (August, 1965).
45. A. D. Pasternak, "Isothermal Compressibility of the Liquid Alkali Metals," Mat. Sci. Eng., 3, No. 2, p. 65 (1968).